# Single Photon Sources in Infrared

**Xu Wang**


Clarendon Laboratory

Department of Physics

University of Oxford

Thesis submitted for the degree of

Doctor of Philosophy

Lincoln College

Trinity Term 2011

**Single Photon Sources in Infrared**

Xu Wang

Clarendon Laboratory, Department of Physics, University of Oxford

Thesis submitted for the degree of Doctor of Philosophy

Trinity Term 2011

---

## Abstract

This thesis reports the study of single photon sources that emit one infrared wavelength photon at a time, creating cavity quantum electrodynamical effects for applications such as quantum information processing. This work considers in two major single photon sources: a) InAs single quantum dots and b) single carbon nanotubes, which both emit in the infrared range.

Photonic crystal slabs and photonic crystal waveguides are served as distinctive passive devices with manipulated photonic band-gaps to control the propagating light. A Simulation of leaky modes of two-dimensional photonic crystal slabs is introduced to constrain model parameters in the device design. Fullerenes are used as fluorescent material to achieve resonance of a leaky mode with excitation 1492 nm and emission at 1519 nm and to see enhancement of the PL. We include novel characterization techniques and PL measurements to show sharp emission peaks from single quantum dots and successfully couple them to micro-cavities. The strong coupling effect is observed and is amongst the best examples of cavity-dot structures achieved to date.

Single-walled carbon nanotubes have shown anti-bunched light emission, thus we systematically study them as another possible candidate of single photon sources. PLE spectra show clear evidence of the existence of excited states, and time evolution measurements reveal the disorder induced diffusion, which separate the tubes into a series of quantum dots. These strongly confined states are concluded as the origin of the possibility that single-walled carbon nanotubes are single photon sources.

# Publications

- *Design of leaky modes of two-dimensional photonic crystal slabs to enhance the luminescence from $Er_3N@C_{80}$ fullerenes*

  Yiling Qi, Anas F. Jarjour, Xu Wang, Robert A. Taylor, Guoquan Zhang, Optics Communications **282**, 3637 (2009).

- *Strongly coupled single quantum dot in a photonic crystal waveguide cavity*

  F. S. F. Brossard, X. L. Xu, D. A. Williams, M. Hadjipanayi, M. Hugues, M. Hopkinson, X. Wang, and R. A. Taylor, Applied Physics Letters **97**, 111101 (2010).

- *Optical studies on a single GaN nanocolumn containing a single $In_xGa_{1-x}N$ quantum disk*

  Mark J. Holmes, Young S. Park, Xu Wang, Christopher C. S. Chan, Benjamin P. L. Reid, HeeDae Kim, Robert A. Taylor, Jamie H. Warner, and Jun Luo, Applied Physics Letters **98**, 251908 (2011).

- *Carrier dynamics of $In_xGa_{1-x}N$ quantum disks embedded in GaN nanocolumns*

  Mark J. Holmes, Young S. Park, Xu Wang, Christopher C. S. Chan, Anas F. Jarjour, Robert A. Taylor, Jamie H. Warner, Jun Luo, H. A. R. El-Ella, and R. A. Oliver, Journal of Applied Physics **109**, 063515 (2011).

- *Optical studies of GaN Nanocolumns containing InGaN quantum disks and the effect of strain relaxation on the carrier distribution*

Mark J. Holmes, Young S. Park, Xu Wang, Christopher C. S. Chan, Jun Luo, Jamie H. Warner, and Robert A. Taylor, accepted for publication in Phys. Stat. Sol. (c) (2011).

- *Wedgebox analysis of four-lepton events from neutralino pair production at the LHC* G. Bian, M. Bisset, N.Kersting, Y.Liu, and X.Wang, The European Physical Journal C **53**, 429 (2008).

# Contents

**Publications** **1**

**1 Introduction** **7**

1.1 Single photon sources . . . . . 7

1.1.1 Introduction to single photon sources . . . . . 7

1.1.2 Potential single photon sources . . . . . 8

1.1.3 Why infrared? . . . . . 10

1.2 Physics behind single photon generation . . . . . 11

1.3 Applications of single photon sources . . . . . 12

1.3.1 Double-slit experiment and quantum eraser . . . . . 13

1.3.2 Quantum information processing . . . . . 13

1.3.3 Entanglement and other applications . . . . . 14

1.4 Photonic crystals . . . . . 15

1.4.1 Photonic band gap . . . . . 15

1.4.2 L3 photonic crystals . . . . . 16

1.5 Thesis layout . . . . . 16

**2 Design of leaky modes of two-dimensional photonic crystal slabs** **18**

2.1 FDTD theory . . . . . 18

2.1.1 Photonic band gap calculation . . . . . 18

2.1.2 Absorption boundary condition . . . . . 22
2.1.3 MEEP calculation software . . . . . 22
2.2 FDTD study background . . . . . 24
2.3 Modeling PhCs . . . . . 26
2.4 PhC design and fullerene PL enhancement . . . . . 28

**3 Towards CQED with InAs/GaAs quantum dots 35**
3.1 Quantum dots . . . . . 35
3.1.1 Quantum dots growth . . . . . 35
3.1.2 InAs quantum dots . . . . . 37
3.1.3 Excitation and emission . . . . . 38
3.2 Characterization of single quantum dots . . . . . 40
3.2.1 Laser sources . . . . . 40
3.2.2 Spectrometer . . . . . 42
3.2.3 InGaAs diode array . . . . . 43
3.2.4 Superconducting nanowire single photon detectors . . . . . 43
3.2.5 Actuators . . . . . 44
3.2.6 Quantum dots PL spectroscopy . . . . . 45
3.2.7 Single quantum dots . . . . . 45
3.2.8 Spectral line shape . . . . . 47
3.3 SU-8 single quantum dots positioning . . . . . 49
3.3.1 SU-8 lithography and quantum dot registration . . . . . 49
3.3.2 Discussion on SU-8 adhesion and problems . . . . . 51
3.4 Scan quantum dot positioning using a new scanning techknoledge . . . . 52
3.4.1 Locating quantum dots . . . . . 53
3.4.2 Results and discussion . . . . . 54

**4 Light-matter interaction 56**

4.1 Cavity quantum electrodynamics . . . . . 56

4.1.1 SS-CQED: a short history . . . . . 57

4.1.2 Coupling regimes . . . . . 58

4.2 Photonic crystals . . . . . 62

4.2.1 Photonic waveguide . . . . . 62

4.2.2 Device design . . . . . 63

4.2.3 PhCWGs characterisation . . . . . 65

4.3 Strong coupling . . . . . 67

4.3.1 Looking for the boundary of strong coupling . . . . . 68

4.3.2 Identifing promising samples . . . . . 70

4.3.3 Strong coupled quantum dots in a photonic waveguide . . . . . 72

**5 Single-walled carbon nanotubes 78**

5.1 Carbon materials, an introduction . . . . . 78

5.2 The synthesis of CNTs . . . . . 79

5.2.1 CNT growth . . . . . 80

5.2.2 Conjugated polymers . . . . . 81

5.2.3 Dispersion of CNTs in conjugated polymers . . . . . 82

5.3 Characterization, a study case of single photon material . . . . . 84

5.3.1 Carbon nanotubes bundles . . . . . 85

5.3.2 How to find single CNTs . . . . . 88

5.3.3 Single CNTs . . . . . 91

5.4 Quantum dots confined in single-walled carbon nanotubes . . . . . 94

5.4.1 State filling spectroscopy of CNTs . . . . . 95

5.4.2 Spectral difusion and charge transfer in CNTs . . . . . 97

5.5 CNTs as single photon sources and future work . . . . . 106

**6 General conclusion and outlook** **108**

**A 2-D photonic crystal slab MEEP code** **111**

**B Modeling of electron phonon coupling in CNTs** **118**

**Bibliography** **122**

# Chapter 1

# Introduction

## 1.1 Single photon sources

### 1.1.1 Introduction to single photon sources

A single photon source (SPS) is a device that will either emit a single photon on demand or emits single photons at a given rate [1]. Realistically, a perfect single photon source can never be achieved because the sub-Poisson distribution can emit zero or multiple photons at random. This is quite different to an attenuated laser or thermal light source for which the number of photons emitted in a given rate will follow a Poisson distribution. The second-order coherence function $g_0^{(2)}$ sets the limit on the photon probability per pulse, and a single photon source has $0 \leq g_0^{(2)} < 1$. There are three major characteristic standards to measure the actual SPS: 1) the external quantum efficiency $\eta_{total}$, which defines the output efficiency, 2) the maximum repetition frequency $f_{max}$ that can be enhanced by the coupling to cavity modes and 3) the indistinguishability $F(0)$ which demands the identical output photon [2].

The type of single photon source studied here originates from the optical transition from confined discrete energy states with atom-like structure. It should be pointed out

that since both the quantum dots and carbon nanotubes have been shown to exhibit antibunched light emission [3,4], this thesis will not cover the Hanbury-Brown and Twiss experiment. Instead, the coupling to cavities and the physics behind spontaneous emission will mainly be the focus of this work.

### 1.1.2 Potential single photon sources

Single quantum dots (QDs) are without doubt the most promising candidates for SPSs. A quantum dot is an "atom like" three-dimensional confinement nano area in a semiconductor. This is very different from the 2D quantum wells and 1D quantum wires due to its discrete density of states. Sub-Poissonian light emission has been observed via fluorescence experiments [5–7]. Quantum confinement of single particles in the quantized levels and Coulomb interaction both determine the confined energy. QDs have several advantages as sources for single photons. Taking an InAs QDs coupled to a microcavity device as an example, light from the dot will be diverted mostly into a single spatial mode, which can achieve a very high $\eta_{\text{total}}$ (more than 80%) in theory), while high $f_{\max}$ is obtained by the enhanced spontaneous emission. The dots do not suffer from photobleaching or spectral diffusion, and show generally very stable photoluminescence. Two consecutively emitted photons have been proven to exhibit a fairly high indistinguishability of 80% overlap [8]. More recently, an experiment demonstrated indistinguishable photons from two different quantum dots [9].

Another solution to the SPS problem has been to use nitrogen-vacancy (NV) centers in synthetic diamond crystals as photon emitters. A nitrogen impurity with an adjacent carbon vacancy lies along the diamond lattice and can be synthesized by electron irradiation followed by annealing in a nitrogen environment. This well controlled process can produce uniform low density NV centers which emit antibunched photons with high quantum efficiency [10, 11]. One major advantage of NV center SPSs is room tempera-

ture operation. However, they intermittently stop emitting due to shelving in metastable levels. The NV center in diamond is regarded as promising solid state spin qubit thanks to the milisecond electron spin coherence lifetimes.

Single-walled carbon nanotubes(CNTs) have recently been reported to show anti-bunching emission [4]. These 1D materials, rolled up from graphene sheets, strongly confine QDs inside the tube in the presence of backscattering and impurity centers. Strong electron-phonon interaction with the help of exciton-exciton annihilation creates the possibility of emitting just one photon at a time [12]. Spectral diffusion is also an issue for CNTs with non-Markovian decoherence [13] but mass production (scalability) and exceptional electron conductivity are an advantage. In addition, chirality selection brings a massive broadband emission range, suitable for many practical applications. CNT-cavity devices have been made and have shown promising emission enhancement [14].

**Table 1.1:** Comparison of parameters for single-photon sources candidates presented in the text

| Parameter | InAs Quantum dots | Diamond NV-centers | Single-Walled Carbon Nanotubes | $D^0$X in ZnSe or GaAs |
|---|---|---|---|---|
| ZPL wavelength | 275-1550 nm | 637 nm | 483-1600 nm | 444/819 nm |
| Spontaneous emission rate $\gamma$ | $(0.5-1\text{ns})^{-1}$ | $(12\text{ns})^{-1}$ | $(0.001-0.5\text{ns})^{-1}$ | $(>1\text{ns})^{-1}$ |
| Optical linewidth | | | | |
| Single | (1-1000)$\gamma$ | (1-1000)$\gamma$ | (1-100)$\gamma$ | 1 GHz |
| Ensemble | $10^4$ GHz | 10 GHz | 10 GHz | 1-5 GHz |
| Cavity coupling | easy | difficult | easy | not exploied |

There are many other candidates for SPSs. These include semiconductor donors and acceptors in GaAs and ZnSe at zero magnetic field. The donor-acceptor bond exciton naturally provides an atom-like system and single-photon generation was proven with

DBR microcavities [15]. All of the SPSs described above emit continuous streams of sub-Poissonian photons. A comparison of different sources is summarized in Table 1.1. This thesis will mainly cover QDs and CNTS in the infrared range.

### 1.1.3 Why infrared?

Our main motivation in extending SPS device operation to the infrared (IR) region is to get better coupling between single emitters and microcavities. Take a QD coupled in a microcavity as an example. The quality factor Q ($\equiv \lambda/\Delta\lambda$) is a measure of the coupling quality. Where $\Delta\lambda$ is the band width, thus higher wavelength obviously means a higher Q. Also the hole sizes used in photonic crystals are bigger and thus easier to fabricate accurately. A low QD density is an a priori requirement since it guarantees that we are dealing with one quantum emitter within a cavity, which is essential for single photon studies. In addition, the shape of a dot severely affects its optical transitions. The distance between the lowest quantized levels varies as $1/R^2$, where R is the radius of the QD. Indeed, photonic crystals are much easier to couple with bigger dots due to the QD size and increased oscillator strength obtained.

Initially we worked with InAs quantum dots emitting around 900 nm. By accurately controlling the growth recipe, we were able to obtain low-density quantum dots emitting beyond 1200 nm. In single-walled nanotubes, which will be considered in Chapter 4 in this work, emission around 1300 nm can be obtained through carefully selecting the chirality of carbon nanotubes.

Last but not least, manipulating quantum states is rather important, particularly in the case of secure transfer of information via photons, i.e. quantum cryptography. Optical losses in fibers are small in the telecommunication wavelength bands around 1300 nm and 1550 nm. Due to the high wavelength dependence, this so-called Quantum Key Distribution (QKD) demands fiber based single photon transmission at telecommunication

wavelengths [16].

## 1.2 Physics behind single photon generation

The atom-like system we study in this work will depend on optical excitation. The photon number in the incoming laser pulse follows a Poissonian distribution,

$$P_{(n/\mu)} = \frac{\mu^n}{n!} e^{-\mu}, n = 0, 1, 2... \tag{1.1}$$

where $p_{n/\mu}$ is the probability of $n$ photons being contained in the laser pulse and $\mu$ is the mean photon number. If our device can somehow transfer the output field to $p_1 = 1$, and $p_{n\neq 1} = 0$ then we have an ideal SPS, and the light emission follows a sub-Possonian distribution.

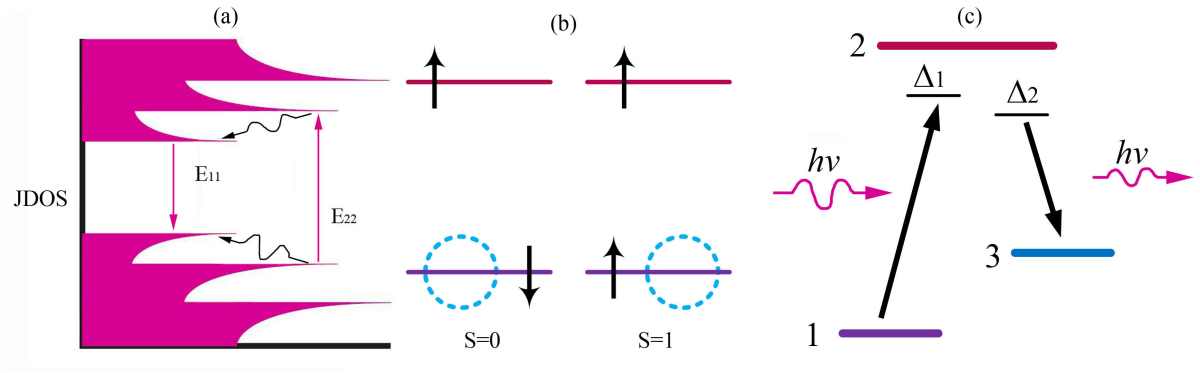


**Figure 1.1:** Schematic illustration of a single photon system in a quantum confined device. (a) The VHS energy states with $E_{11}$ and $E_{22}$ transitions. (b) electron spin excitation with black arrows indicating spin and the blue circles representing holes. (c) a 3 level system depicting a coherent excitation scheme.

We now use CNTs to explain the energy-level structure with discrete states which could represent a solid state SPS device. Figure 1.1 (a) shows a CNT single particle

joint density of states connecting the valence and conduction energy bands. The high symmetry points in the Brillouin zone forms the "kink" shaped van Hove singularities (VHSs). In a semiconducting material, with larger than band gap excitation energy, an electron in the $i^{\text{th}}$ valence band can be excited to the $j^{\text{th}}$ conduction band. After phonon assisted relaxation, the system then emits a single photon spontaneously. In an excitonic picture, when an electron with spin $\uparrow$ is excited to the excited states by absorbing a photon (Figure 1.1 (b)), a hole with spin $\downarrow$ is left behind in the ground state. Thus we obtain a spin singlet bright exciton in which the electron and hole can recombine by emitting a photon. This S = 0 exciton also has larger exciton binding energy due to the Coulomb interaction. By contrast, if there is a spin $\uparrow$ in each energy state then we have S = 1, which is called a trion exciton (S = 1) (triplet) and cannot recombine because of the Pauli exclusion principle. Thus it is called a dark exciton. With a cavity, this single photon picture could be more interesting. Figure 1.1 (c) shows a single emitter resonantly coupled to an optical microcavity. $|1\rangle$ and $|3\rangle$ are two non-degenerate ground states and $|2\rangle$ is the excited state. Suppose the system starts in state $|1\rangle$. The dipole transition $|1\rangle$ to $|2\rangle$ couples to a control pulse. State $|2\rangle$ to $|3\rangle$ is coupled to a cavity mode. When slowly varying the control pulse with detuning $\Delta$, a coherent transition can be realized from $|1\rangle$ to $|3\rangle$, thus placing a single photon unperturbed in the cavity.

## 1.3 Applications of single photon sources

There are many possible SPS applications, mainly on quantum information technologies ranging from long distance quantum key distribution to coherent manipulation of a single node. We provide a general introduction here and point out further reading recommendations.

### 1.3.1 Double-slit experiment and quantum eraser

The famous double-slit experiment [17] can be conducted with an interferometer. A mode-locked laser operating well above threshold can generate reasonable short pulses close to a coherent state [18]. We think of an experiment with a double slit after the laser pulse and try to detect the separated photons by placing two single photon detectors behind a beamsplitter. A surprising feature emerges: no matter how large the optical losses are in the two passes, we can always observe a perfect interference pattern as long as the losses are the same. This phenomenon is a perfect demonstration of quantum mechanics, especially when the light source is a single photon source, as the final measurement will be secure only to the observer, which brings us to the next section.

### 1.3.2 Quantum information processing

Quantum information processing (QIP) is the art of transferring and storing a quantum state between different registers. A "*qubit*" as in the case of two-dimensional Hilbert spaces, is the basic unit of quantum state transfer. Generally speaking, QIP includes many subjects such as quantum cryptograph, quantum error correction and quantum computing etc. Among them, QKD is a well known example.

As information technology develops, methods of encoding and breaking ciphers are also progressing. The maturing of new computing algorithms places high demands of new ways of protecting information. For example, the factoring problem proposed from Shor's algorithm of a polynomial solution challenges all current key distribution [19]. A replacement is needed, even though we are still far from a real quantum computers. Quantum cryptography aims to develop a fundamentally unbreakable cipher. Traditionally, the initial quantum state A is named Alice and the objective state B is called Bob. If the key can be encoded on the quantum states of single particles, and then sent to Bob from Alice, any measurement performed by an eavesdropper (Eve) can be detected

by Bob since it will cause the collapse of the prepared pure quantum states [20].

Several schemes have been proposed to utilize these advantages of quantum communication. John Bell introduced the experimental question of Bell inequalities [21] and Bennett and Brassard created the `BB84` protocol. Each photon is encoded by a logical zero or one as two orthogonal polarizations. When the polarization basis randomly changes from linear to circular, information is encoded into four polarization states of a quantum system: horizontal, vertical, right circular or left circular. Bob's choice of basis is arbitrary. Once Alice and Bob have compared the associated basis and eliminated all the wrong bases through a public channel, a shared, random sequence of key can be obtained. In the presence of Eve, the measurement and transmission basis will be the same so the security of the `BB84` relies on the assumption that states are encoded in single photons. If the source emits more than one photon, Eve could then attack one of the photons while allowing the unperturbed photon to reach Bob.

In the standard paradigm of QIP, a quantum network connects quantum computers to perform controlled operations and to manipulate the information stored in the nodes of the network. Preparation and measurement of a node can cause the "collapse" of the pure quantum state. The operation on a node is called a *single-qubit gate* and the computation can be realized by transporting a single photon in the network [22].

### 1.3.3 Entanglement and other applications

Single photon sources have proven to be able to generate entangled photon pairs. One such example is by Fattal et. al. [23] by checking the joint polarizations of two photons with orthogonal polarization after a beamsplitter. If they are detected from a different output after the beamsplitter then one can reconstruct the complete polarization states of the two photons. SPS are useful in many other fields such as quantum repeaters [24] and nonlinear optics [25]. SPS research is progressing quickly and many new ideas are

being brought into the field.

## 1.4 Photonic crystals

As stated before, an optical micro cavity is an essential component to achieve a high efficiency single photon source. There are 3 important parameters used to judge the quality of a cavity: the quality factor $Q$ introduced in Section 1.1.3, the mode volume V, which introduces the maximum electric field strength, and the ratio $\kappa_C/\kappa$ which is the cavity field coupling efficiency. To date, there are several successful micro cavities in use, including planar Bragg reflector mirrors [26], micropillars [22], microdisks [27] and photonic crystals [28]. We introduce photonic crystals (PhC) microcavities since they are related to the work in this thesis.

### 1.4.1 Photonic band gap

In semiconductor materials, the periodic of molecules and atoms can manipulate the electron energy distribution. Electrons' states are forbidden in the complete band gap between the conduction and valence bands, the so-called the forbidden band. Bandgap engineering is intensively used in the rapidly developing electronic photonic materials market. In a similar fashion, periodic photonic structures (with a periodic refractive index change) also exhibit forbidden bands. In this case, however, it is propagation of electromagnetic waves in certain directions that is inhibited, leading to the formation of a photonic band gap (PBG). It is therefore possible to manipulate the propagation of light by varying the periodic photonic structures [29].

### 1.4.2 L3 photonic crystals

It is possible to create one, two and three-dimensional photonic crystal structures. Light scattering off planes introduces photonic band gaps. No electromagnetic waves can propagate in the band gap. Technically, a complete band gap only exists in 3D PhCs. However, a $Q$ of over 100000 can be produced in 2D crystals [30]. In particular, when the symmetry of a photonic crystal is broken, e.g. by the introduction of defects, localized modes with certain frequencies can exist within the gap. Figure 1.2 shows a scanning electron microscope image of a so-called "L3" 2D planar photonic crystal cavity. The central 3 holes have been removed and the two holes next to them were also shifted to avoid an abrupt change in the electromagnetic field. Single photon devices can be made by these 2D PhCs thanks to their extremely small mode volume and high Qs.

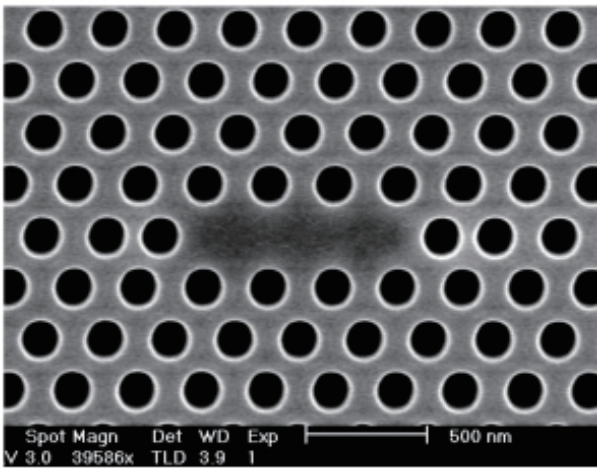


**Figure 1.2:** SEM image of a L3 PhC.

## 1.5 Thesis layout

In **Chapter 2** we give an overview of the theoretical models of PhCs fabrication. In particular, we use MEEP software package to predict the leaky mode of a device with

fullerenes coupled to a PhC. With the introduction of photonic band gap, we show a perfect match of the absorption and emission energy from fullerene PL to that of PhC. We also simulate the electromagnetic field at the defect of a PhC. This MDTD method is used as a basic model in the following chapters. An introduction to single QD spectroscopy is given in **Chapter 3** where we also review the previous work on InAs QDs. This starts with QDs growth techniques and optical transitions and moving onto a brief introduction of our general experimental equipments. Fabrication methodologies of the SU-8 samples are presented. They allow for accurate spectral and spatial registration of a single quantum dot. However, contamination is an issue for the SU-8 method and so a new registration method is introduced. By scanning the position of pattern's edges regarding to the positions of QDs, one can locate the QDs with an all-optical method, which effectively reduces the processes of registering a quantum dot. **Chapter 4** examines the light matter interaction of QDs with cavities. After reviewing cavity quantum electrodynamics we describe the fabrication of a photonic wave guide coupled to high QDs density sample. This leads to a strong coupling phenomenon which is essential for QDs as a single photon source. In **Chapter 5**, a review on carbon materials and conjugated polymer is given. By comparing the single and bundle PL from CNTs we conclude with some intrinsic properties of single quantum dots such as spectral diffusion. A brand new CNT-polymer fabrication method is discussed and this leads to the excellent optical performance of the single CNTs we used in our experiments. A theoretical model is developed which predicts the phonon assisted exciton decay channel. With help of newly discovered methods of finding single CNTs, we prove the QD-like states confined in CNTs and this provides a strong support for CNTs as single photon sources. The general conclusions of the work in this thesis are presented in **Chapter 6** where we focus particularly on providing insight into how a better understanding of the observed results can be obtained.

# Chapter 2

# Design of leaky modes of two-dimensional photonic crystal slabs

## 2.1 FDTD theory

The design of electronic devices involves the processes of modeling, analyzing and experimental verification. The modeling needs to be repeated many times to achieve a better design, hence numerical modeling has become a very important method of designing electronic devices and integrated circuits.

### 2.1.1 Photonic band gap calculation

The aim of research into micro- and nano-photonic structures is to utilize the results in modern photonic information processing. The idea is to speed up the design process and decrease the development investment. The complex geometry and structure of periodic photonic micro-structures prevents researchers from using normal methods

to analyze the electromagnetic wave packet. Photonic modeling software appeared following the rapid development of optical fiber technology at the end of the last century. According to microwave simulation theory, there are several commercial software suites now in the tens of years of development. For example OptiBPM and OptiFDTD from Optiwave Systems [31, 32], coupling analysis software from Comsol Multiphysics, etc. These software packages mainly deal with plain-wave photonic waveguides and the composite photonic structures. Here we mainly focus on the Finite-difference time-domain method (FDTD) [33]. The powerful FDTD is used to solve the dynamic response of open structures.

The FDTD algorithm was first introduced by Kane Yee in 1966 [34]. This electromagnetic field modeling and simulation method is currently very popular and is briefly described in this section.

Consider a space with no electric or magnetic current sources, but with materials that may absorb electric or magnetic field energy. The general spatial- and time-dependence of these materials follow Maxwell's equations:

$$\frac{\partial \vec{H}}{\partial t} = -\frac{1}{\mu}\vec{\nabla} \times \vec{E}, \tag{2.1}$$

$$\frac{\partial \vec{E}}{\partial t} = \frac{1}{\epsilon}\vec{\nabla} \times \vec{H} - \frac{\sigma}{\epsilon}\vec{E}. \tag{2.2}$$

where $\vec{H}$ is defined by $\vec{\mathrm{B}}/\mu - \vec{\mathrm{M}}$, $\vec{\mathrm{M}}$ is the regional magnetizing density, $\mu$ is the magnetic permeability, $\epsilon$ is the electric permittivity and $\sigma$ is the electric conductivity.

In a 3D Cartesian rectangular coordinate system $(x, y, z)$, the Maxwell equations are decomposed and can be expressed as:

$$\frac{\partial H_x}{\partial t} = -\frac{1}{\mu}\left(\frac{\partial E_z}{\partial y} - \frac{\partial E_y}{\partial z}\right) \tag{2.3}$$

$$\frac{\partial H_y}{\partial t} = -\frac{1}{\mu}\left(\frac{\partial E_x}{\partial z} - \frac{\partial E_z}{\partial x}\right) \tag{2.4}$$

$$\frac{\partial H_z}{\partial t} = -\frac{1}{\mu}\left(\frac{\partial E_y}{\partial x} - \frac{\partial E_x}{\partial y}\right) \tag{2.5}$$

$$\frac{\partial E_x}{\partial t} = \frac{1}{\epsilon}\left(\frac{\partial H_z}{\partial y} - \frac{\partial H_y}{\partial z} - \sigma E_x\right) \tag{2.6}$$

$$\frac{\partial E_y}{\partial t} = \frac{1}{\epsilon}\left(\frac{\partial H_x}{\partial z} - \frac{\partial H_z}{\partial x} - \sigma E_y\right) \tag{2.7}$$

$$\frac{\partial E_z}{\partial t} = \frac{1}{\epsilon}\left(\frac{\partial H_y}{\partial x} - \frac{\partial H_x}{\partial y} - \sigma E_z\right) \tag{2.8}$$

The basic idea of the FDTD algorithm is that E and H are interleaved. In the 3D case, each E/H component is surrounded by four H/ E components, as shown in Figure 2.1. By solving these equations with certain initial and boundary conditions we get leapfrog time-stepping, the so-called "Yee Cube": All the E components for a particular time in the 3D spaces are calculated and stored in memory using the H data previously calculated in memory. Then all the following H data are calculated and stored in memory using the E data just stored. All derivatives in the equations above are replaced by central finite differences and can be shown with fake color in a computer, therefore clear simulation is visible with second order accuracy.

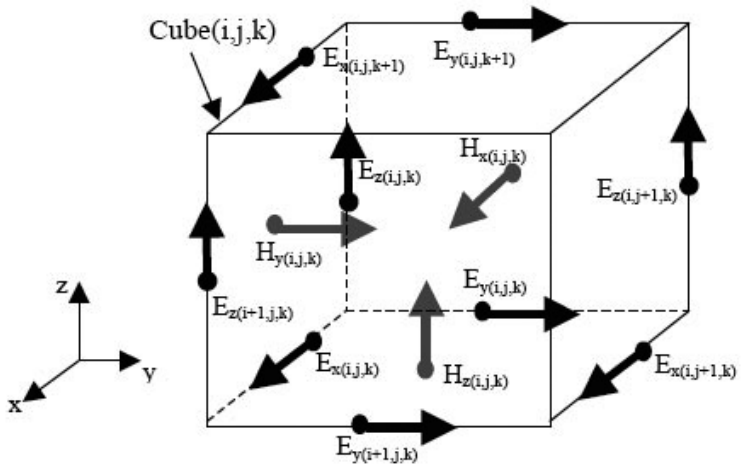


**Figure 2.1:** Position of the E and H about a cubic unit cell of the Yee space lattice.

In the FDTD simulation, leapfrog time-stepping is set as $u$ to represent $E_x$, $E_y$, $E_z$,

$H_x$, $H_y$ and $H_z$. The simulation uses the notation $u(i\Delta x, j\Delta y, k\Delta z, n\Delta t)$=$u^n_{ijk}$:

$$\frac{\partial u}{\partial x}(i\Delta x, j\Delta y, k\Delta z, n\Delta t) = \frac{\partial u^n_{ijk}}{\partial x} = \frac{u^n_{i+1,j,k} - u^n_{i,j,k}}{\Delta x} \tag{2.9}$$

$$\frac{\partial u}{\partial t}(i\Delta x, j\Delta y, k\Delta z, n\Delta t) = \frac{\partial u^n_{ijk}}{\partial t} = \frac{u^{n+1}_{i,j,k} - u^n_{i,j,k}}{\Delta t} \tag{2.10}$$

then for every time step we have:

$$H^{n+\frac{1}{2}}_{x(i,j,k)} = H^{n-\frac{1}{2}}_{x(i,j,k)} - \frac{\Delta t}{\mu}\left(\frac{E^n_{z(i,j+1,k)} - E^n_{z(i,j,k)}}{\Delta y} - \frac{E^n_{y(i,j,k+1)} - E^n_{y(i,j,k)}}{\Delta z}\right) \tag{2.11}$$

$$H^{n+\frac{1}{2}}_{y(i,j,k)} = H^{n-\frac{1}{2}}_{y(i,j,k)} - \frac{\Delta t}{\mu}\left(\frac{E^n_{x(i,j,k+1)} - E^n_{x(i,j,k)}}{\Delta z} - \frac{E^n_{z(i+1,j,k)} - E^n_{z(i,j,k)}}{\Delta x}\right) \tag{2.12}$$

$$H^{n+\frac{1}{2}}_{z(i,j,k)} = H^{n-\frac{1}{2}}_{z(i,j,k)} - \frac{\Delta t}{\mu}\left(\frac{E^n_{y(i+1,j,k)} - E^n_{y(i,j,k)}}{\Delta x} - \frac{E^n_{x(i,j+1,k)} - E^n_{x(i,j,k)}}{\Delta y}\right) \tag{2.13}$$

$$E^{n+1}_{x(i,j,k)} = \left(\frac{1-\frac{\sigma\Delta t}{2\epsilon}}{1+\frac{\sigma\Delta t}{2\epsilon}}\right)E^n_{x(i,j,k)} + \frac{\frac{\Delta t}{\epsilon}}{1+\frac{\sigma\Delta t}{2\epsilon}}\left(\frac{H^{n+\frac{1}{2}}_{z(i,j,k)} - H^{n+\frac{1}{2}}_{z(i,j-1,k)}}{\Delta y} - \frac{H^{n+\frac{1}{2}}_{y(i,j,k)} - H^{n+\frac{1}{2}}_{y(i,j,k-1)}}{\Delta z}\right) \tag{2.14}$$

$$E^{n+1}_{y(i,j,k)} = \left(\frac{1-\frac{\sigma\Delta t}{2\epsilon}}{1+\frac{\sigma\Delta t}{2\epsilon}}\right)E^n_{y(i,j,k)} + \frac{\frac{\Delta t}{\epsilon}}{1+\frac{\sigma\Delta t}{2\epsilon}}\left(\frac{H^{n+\frac{1}{2}}_{x(i,j,k)} - H^{n+\frac{1}{2}}_{x(i,j,k-1)}}{\Delta z} - \frac{H^{n+\frac{1}{2}}_{z(i,j,k)} - H^{n+\frac{1}{2}}_{z(i-1,j,k)}}{\Delta x}\right) \tag{2.15}$$

$$E^{n+1}_{z(i,j,k)} = \left(\frac{1-\frac{\sigma\Delta t}{2\epsilon}}{1+\frac{\sigma\Delta t}{2\epsilon}}\right)E^n_{z(i,j,k)} + \frac{\frac{\Delta t}{\epsilon}}{1+\frac{\sigma\Delta t}{2\epsilon}}\left(\frac{H^{n+\frac{1}{2}}_{y(i,j,k)} - H^{n+\frac{1}{2}}_{y(i-1,j,k)}}{\Delta x} - \frac{H^{n+\frac{1}{2}}_{x(i,j,k)} - H^{n+\frac{1}{2}}_{x(i,j-1,k)}}{\Delta y}\right) \tag{2.16}$$

One can hence solve the electromagnetic field distribution using the above equations and the FDTD method is based on the solution of these differential equations instead of the original solution of electromagnetic field partial differential equations. This simulation will result in the calculated quantities having discrete values. For instance, the calculated wave mode phase velocity using FDTD numerical method is different from light speed in vacuum [35]. To guarantee the stability of the leap-frog algorithm, the FDTD lattice step should be at least 10 times smaller than the propagation electromagnetic wavelength. It is obvious that the smaller the degree of dispersion grid the less

discreet the simulation. However this leads to the increasing requirements for computer hardware and computing speed. Thus we have:

$$\Delta x, \Delta y, \Delta z \leq \frac{\lambda_0}{10} \tag{2.17}$$

where $\lambda_0$ is the propagating electromagnetic wavelength. For the 2nd-order FDTD scheme, the time step should follow the Courant condition for the solution to be stable:

$$\Delta t \leq \frac{1}{c\sqrt{\frac{1}{\Delta x^2} + \frac{1}{\Delta y^2} + \frac{1}{\Delta z^2}}} \tag{2.18}$$

### 2.1.2 Absorption boundary condition

The Absorption Boundary Condition (ABC) is used to simulate the "no physical boundary" electromagnetic region, since it cannot be deduced from Maxwell's equations. This function terminates the region of study by absorbing all outgoing electromagnetic waves, regardless of the polarization, frequency, direction or intensity. The reflection coefficient of the boundary is very close to zero in any case and there is no interruption to the inside field. Therefore, all the outgoing waves from inside never return, which simulates the object in an open space. At the moment people are generally using a perfectly matched layer (PML) [36] as the ABC. By careful design of the PML, absorption can be controlled to be very low. For periodic structures, the Bloch periodic boundary condition becomes applicable [33].

### 2.1.3 MEEP calculation software

The MIT electromagnetic equation propagation (MEEP) is a free calculation software package developed by the Joannopoulos Ab Initio physics group at MIT aiming to sim-

ulate electromagnetic wave transmission using the FDTD method [37]. A list of main features of this package is provided:

1. Calculation objectives can be one dimensional, two dimensional or three dimensional, either using a Cartesian coordinate system or a cylindrical coordinate system;

2. Definable arbitrary materials or arbitrary initial field distribution;

3. Definable arbitrary anisotropic dielectric permittivity $\epsilon$ and permeability $\mu$. The system also takes into account the medium dispersion $\epsilon(\omega)$, $\mu(\omega)$ and the nonlinear effect of the medium (Kerr nonlinearity and the Pockels nonlinearity) with consideration of the conductivity $\sigma$;

4. Boundary conditions include: absorbing boundary conditions (PML), the perfect conductor boundary conditions and Bloch periodic boundary conditions;

5. The development of symmetry includes odd/even mirror symmetry and $90^o/180^o$ rotational symmetry. When the study objective fulfills the symmetry operations, one can reduce the computational domain to improve the computing speed;

6. For the Unix operating system, the user control interface based on GNU Guile compiler environment is simple to use and one can use C++ language software to control the operation;

7. The output format is HDF, which is applicable for a variety of image processing and visualization software;

8. In addition to the serial computation, the expansion MPI package also supports parallel computing.

In the following sections we perform a FDTD simulation on fullerenes dispersed on photonic crystal structures with the MEEP software package to demonstrate the application of MEEP. This simulation was applied throughout our entire study and we were able to determine electromagnetic field distributions in various system. These proved to be extremely useful.

## 2.2 FDTD study background

Fullerenes were discovered in 1985 as the third crystaline carbon form following diamond and graphite [38]. They are composed of a series of pure carbon clusters. Among these, the cylindrical or tubular elements are known as carbon nanotubes. So far, natural fullernes have been found to exist in nature [39] and in space [40]. In the laboratory, stable fullerenes can now be isolated in forms such as $C_{60}$, $C_{70}$ and $C_{82}$. Doped fullerene can be produced by embedding one or more ions or small molecules in the fullerene cage (Endohedral fullerenes) [38, 41–43]. In the field of quantum information processing, fullerene as a qubit−readout unit of a quantum computer has been proposed [44]. Their properties meet the basic conditions for qubits: long-lived spin 1/2 two-level systems; Fluorescence can be achieved from the optical transition from excited state to the ground state (information capacity); the dual-energy level system has a long decoherence time (information storage stability); efficient fluorescent light (information read-out feasible). Erbium-doped trinitride-template (TNT) fullerenes $Er_3N@C_{80}$ offer good optical control and measurement on their fluorescent properties due to the transparency of the fullerene cage at infrared wavelengths. The transition from a free $Er^{3+}$ ion in the first excited state ${}^4I_{\frac{13}{2}}$ to the ground state ${}^4I_{\frac{15}{2}}$ corresponds to an emission wavelength of 1.5 $\mu$m. For $Er^{3+}$ ions embedded in the fullerene structure, the photoluminescence spectrum of an $Er^{3+}$ ion is still at 1.5$\mu$m. This range is often used for fiber optic communications. More importantly, the emission is not in the absorption range of fullerene cage structure. Figure 2.2 (a) provides a schematic diagram of the $Er_3N@C_{80}$ molecular structure while Figure 2.2 (b) shows the $C_{80}$ molecular structure diagram .

Previous spectral studies of fullerenes were undertaken at low temperature, and the fluorescence emission intensity was weak. To realize its potential as a qubit for quantum information processing, researchers have to overcome the endohedral fullerene's limitations of low light emission efficiency. In ref. [46], Ganesh et. al. demonstrates

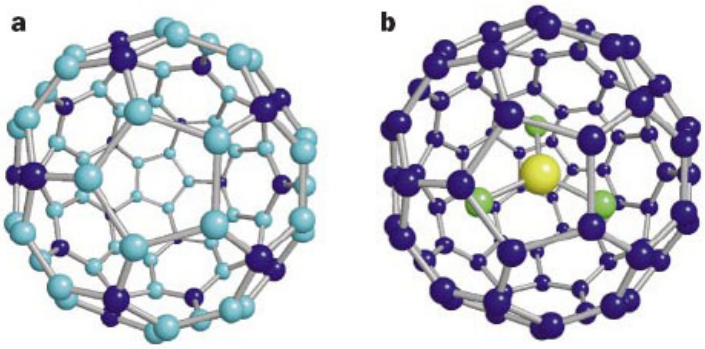


**Figure 2.2:** (a) Fullerene cage structure$C_{80}$ and (b) $Er_3N@C_{80}$ with $Er_3N$molecular structure [45].

**Table 2.1:** $Er_3N@C_{80}$spectral peaks

| Wavenumber ($cm^{-1}$) | Wavelength (nm) | Width ($cm^{-1}$) | Rel. Intensity |
|---|---|---|---|
| 6584.2 | 1518.79 | 5.8 | 1.000 |
| 6611.6 | 1512.49 | 18.0 | 0.072 |
| 6644.0 | 1505.12 | 3.6 | 0.096 |
| 6651.5 | 1503.42 | 11.1 | 0.625 |
| 6701.9 | 1492.11 | 4.0 | 0.245 |
| 6738.1 | 1484.1 | 10.4 | 0.157 |
| 6803.4 | 1469.85 | 8.8 | 0.079 |

enhancement of fluorescence emission from colloidal quantum dots on the surface of two-dimensional photonic crystal slabs. We follow this idea and developed an effective way of designing the PhC structure to manipulate its photonic modes to overlap with both the absorption and emission spectra of the $Er_3N@C_{80}$ for the purpose of enhancing the fluorescence emission and absorption of the $Er_3N@C_{80}$. Consider the deposition of fullerenes on a 2D photonic crystal slab. Erbium ions trapped in fullerene cages can be excited directly to the upper manifold levels with wavelengths longer than 1 $\mu$m. For icosahedral

Ih isomer TNT cages of 99% purity prepared by repeated purification using high pressure liquid phase chromatography, the strongest emission peak of $Er_3N@C_{80}$ is at 1519 nm while the peak at 1492 nm is one of the direct excitation wavelengths at which the observed photoluminescence peak has a narrow linewidth and exhibits relatively strong absorption. All the spectral peaks can be found in Table 2.1.

## 2.3 Modeling PhCs

As described in the previous section, our mission is to find the right material to make a two-dimensional photonic crystal plate in which the photonic mode resonance is located at 1519nm and 1492nm (near-infrared). Given the known properties of GaAs properties of GaAs [47], we choose a two-dimensional GaAs photonic crystal slab as the object of study.

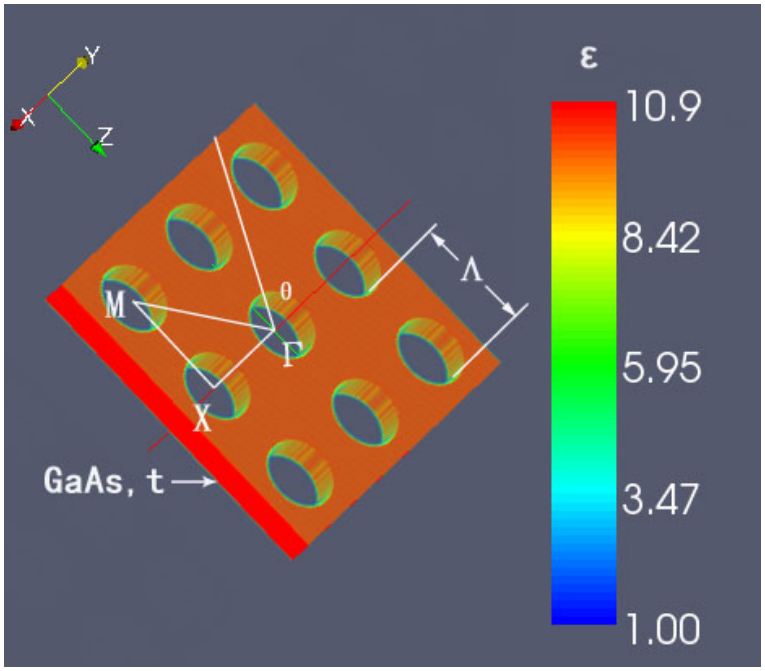


**Figure 2.3:** Two-dimensional GaAs photonic crystal slab structure, where $\epsilon$ represents the dielectric constant of GaAs.

Figure 2.3 shows the two-dimensional GaAs photonic crystal slab (PhC) structure. The periodic structure with air holes has lattice period $\Lambda$, air hole radius $r$, GaAs slab thickness $t$ and $\Gamma$, X, M are high symmetry points in the corresponding square lattice reciprocal lattice vector space. The mechanisms for light confinement in PhCs arise from in-plane light confinement through multiple Bragg reflections, which lead to resonant modes in the structures (termed guided-mode resonances). These modes possess finite lifetimes within such structures and are referred to as "leaky eigenmodes" (hereafter leaky modes). At specific wavelengths and angular orientations of the incident beam, the leaky modes interfere destructively with the transmitted beam, resulting in zero transmission [48]. Therefore, studying the transmission properties of the PhC is a convenient technique to determine the dispersion of the leaky modes. A numerical calculation using the finite difference time domain method based on the MEEP package was chosen and the basic MEEP calculating reference code can be found in Appendix.

In the numerical calculation of two-dimensional GaAs PhC optical transmission properties, the incident light is set to be S polarized light, incident along the direction of high symmetry ($\Gamma - \mathrm{M}$ direction). In Figure 2.3, $\theta$ is the angle between the incident plane wave and the plate normal direction. We ran the MEEP program corresponding to each incident angle to obtain the incident light wave transmission distribution through the photonic crystal wave slab. By repeatedly changing the incident angle, one can get a histogram of transmission rate distribution values. We then use Matlab for numerical processing, by subtracting the grid distribution of the discrete values of transmission rate within the incident light wavelength range to plot a continuous spectrum, as shown in Figure 2.4 below. The relevant two-dimensional thin photonic crystal parameters are: lattice period $\Lambda = 720$ nm, the air hole radius $r = 215$ nm, slab thickness $t = 230$ nm, GaAs refractive index is set to $n = 3.3$. The scale bar represents the normalized transmission efficiency. The white area shows the spectral position corresponding to an

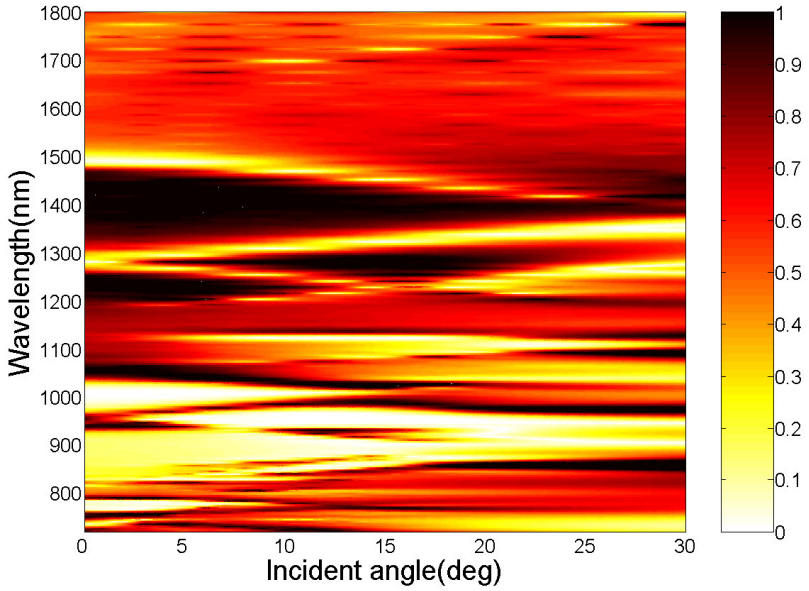


**Figure 2.4:** 2D GaAs PhC optical transmission distributionmeasured by transmission rates.

incident angle with transmission rate of 0. Taking the incident angle of 0° as an example, two distinct resonant leaky modes can be seen in Figure 2.4 between 1200 nm -1600 nm. Adjusting the emission and absorption peaks by matching leaky modes can enhance the emission from $Er_3N@C_{80}$, a technique which will be discussed in the next section.

## 2.4 PhC design and fullerene PL enhancement

We estimated parameters to calculate the transmission efficiency in the two-dimensional GaAs photonic crystal slab shown in Figure 2.4. When the structural parameters of the plate change, the leaky mode changes. Thus by adjusting the structural parameters (such as crystal plate period $\Lambda$, plate thickness $t$ and the air hole radius $r$ etc.), one can manipulate the spectral location of the leaky modes. To accurately match the leaky modes to the $Er^{3+}$ ion emission peak (1519nm) and the absorption peak (1492nm) in the

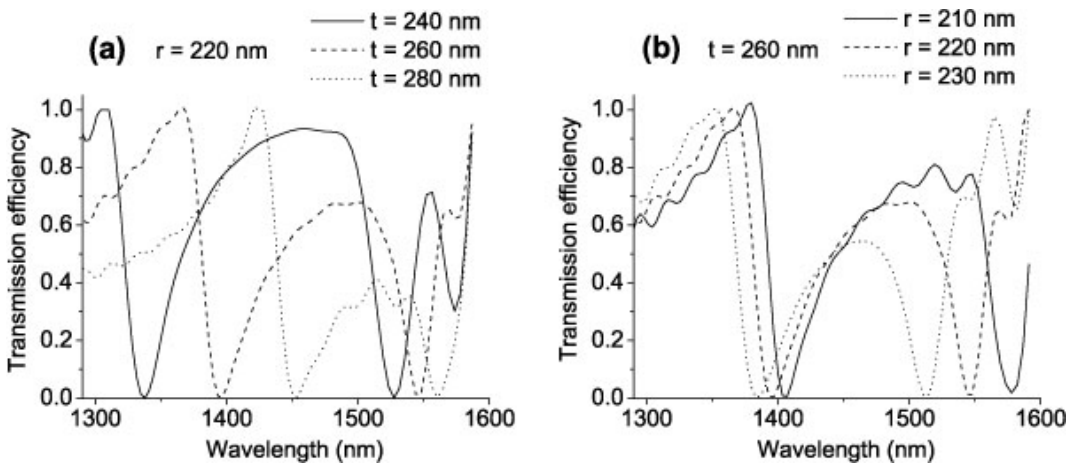


**Figure 2.5:** Transmission efficiency rate of incident light along the normal direction on a PhC: (a) corresponds to when r=220 nm, slab thickness t=240 nm, 260 nm and 280 nm, respectively. (b) corresponds to when t=260 nm, radius are r=210 nm 220 nm and 230 nm, respectively.

three metal nitride doped fullerene $Er_3N@C_{80}$ to enhance PL as described in [46], we will need to determine the structural parameters corresponding to the specific mathematical relationship.

Figure 2.5 shows the dependence of incident light along the normal direction to different structural parameters of the two-dimensional GaAs photonic crystal slab. Figure 2.5 (a) shows the transmission efficiency when the air hole radius $r$ is 220 nm, slab thickness $t$ is 240 nm, 260 nm and 280 nm, respectively; while Figure 2.5 (b) shows the transmission efficiency when the plate thickness is t=260 nm, the air hole radius $r$ is 210 nm, 220 nm and 230 nm, respectively. The other structural parameters remain unchanged with the period $\Lambda = 720$ nm, and the GaAs refractive index is set to $n = 3.3$. Two trends can be seen as the two distinct leaky modes between 1300 nm-1600 nm appear. One is located around 1400 nm, which can match the absorption peak at 1492 nm of $Er_3N@C_{80}$ and with the structural parameters is sensitive to slab thickness $t$; another mode position

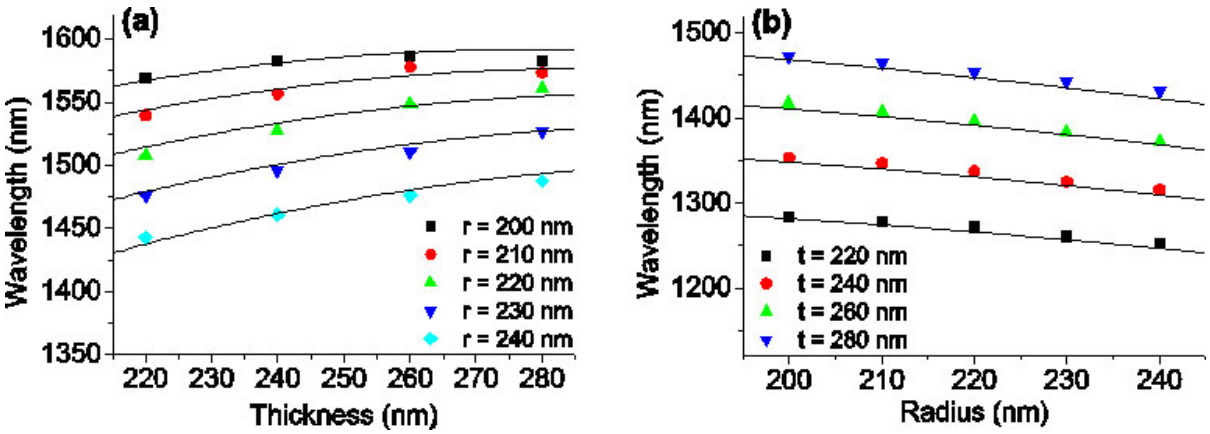


**Figure 2.6:** By varying $t$ and $r$ we can set the PhC to zero transmission, (a) depicts wavelength around 1500 nm to achieve 1519nm (b) corresponds to 1400 nm to matchwith PL emission at 1492 nm.

1550 nm could match with the $Er^{3+}$ ion PL emission peak at 1519nm of $Er_3N@C_{80}$ and is more sensitive to the hole radius $r$.

After we set different $t$ and $r$, we plot the scattering wavelength positions of leaky eigenmode values as shown in Figure 2.6, where Figure 2.6 (a) corresponds to leaky modes around 1519nm while Figure 2.6 (b) corresponds to leaky modes around 1492nm. Because of the non-linear distribution of the figure, we consider higher-order quadratic polynomial fits. Setting the leaky modes around 1519nm as $\lambda_{em}$ and leaky modes around 1492nm as $\lambda_{ex}$, then $\lambda_{em}$ and $\lambda_{ex}$ with respect to $t$ and $r$ satisfy a quadratic function of

**Table 2.2:** Parameters derived from quadratic equation (2.19) and equation (2.20)

| $A_{em}$ (nm) | $B_{em}$ | $C_{em}$ ($nm^{-1}$) | $D_{em}$ | $E_{em}$ ($nm^{-1}$) | $F_{em}$ ($nm^{-1}$) |
|---|---|---|---|---|---|
| 820.322 | 7.144 | -0.030 | 1.313 | -0.007 | 0.013 |
| $A_{ex}$ (nm) | $B_{ex}$ | $C_{ex}$ ($nm^{-1}$) | $D_{ex}$ | $E_{ex}$ ($nm^{-1}$) | $F_{ex}$ ($nm^{-1}$) |
| -19.653 | 2.319 | -0.005 | 6.869 | -0.006 | -0.005 |

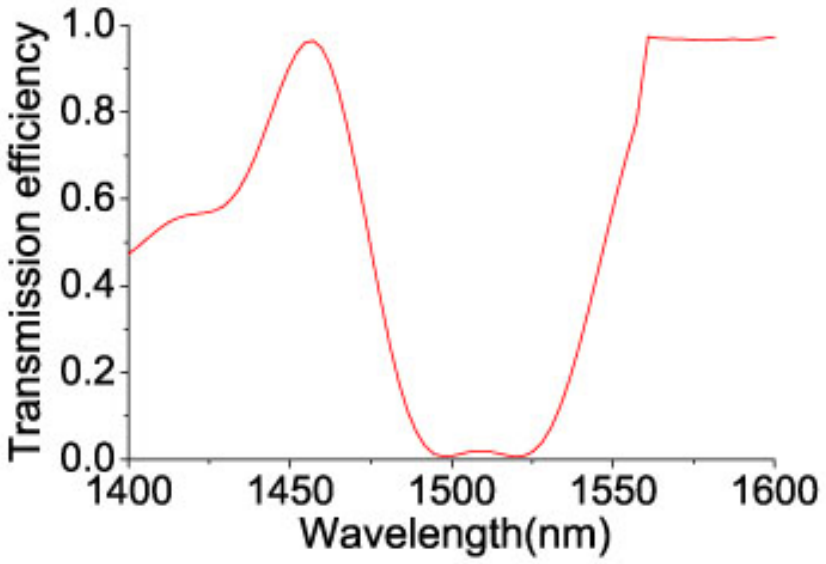


**Figure 2.7:** 2D GaAs PhC transmission efficiency with $r = 233.4$ nm and t=301.5 nm. The two leaky modes are at 1497 nm and 1519 nm, respectively.

the form:

$$\lambda_{em} = A_{em} + B_{em}r + C_{em}r^2 + D_{em}t + E_{em}t^2 + F_{em}r \cdot t, \tag{2.19}$$

$$\lambda_{ex} = A_{ex} + B_{ex}r + C_{ex}r^2 + D_{ex}t + E_{ex}t^2 + F_{ex}r \cdot t. \tag{2.20}$$

where the coefficients $A$, $B$, $C$, $D$, $E$, $F$ can be subtracted from the non-linear fitting of the plot. Table 2.2 lists the the best fit parameter values. According to the expressions for $\lambda_{em}$ and $\lambda_{ex}$ with $t$ and $r$, a continuous curve was also drawn in Figure 2.6. As one can see, the fitted curve and the scattered points calculated from MEEP program are in good agreement with the the predicted wavelength. Inserting the wavelength values $\lambda_{em}$ = 1519 nm, $\lambda_{ex}$=1492 nm into Equations (2.19) and (2.20), we get a slab thickness $t$=301.5nm and a hole radius $r$=233.4nm. These parameters were re-input into the MEEP program to calculate the transmission efficiency, with the result shown in Figure 2.7. Leaky modes of this GaAs photonic crystal structure are located at 1497 nm

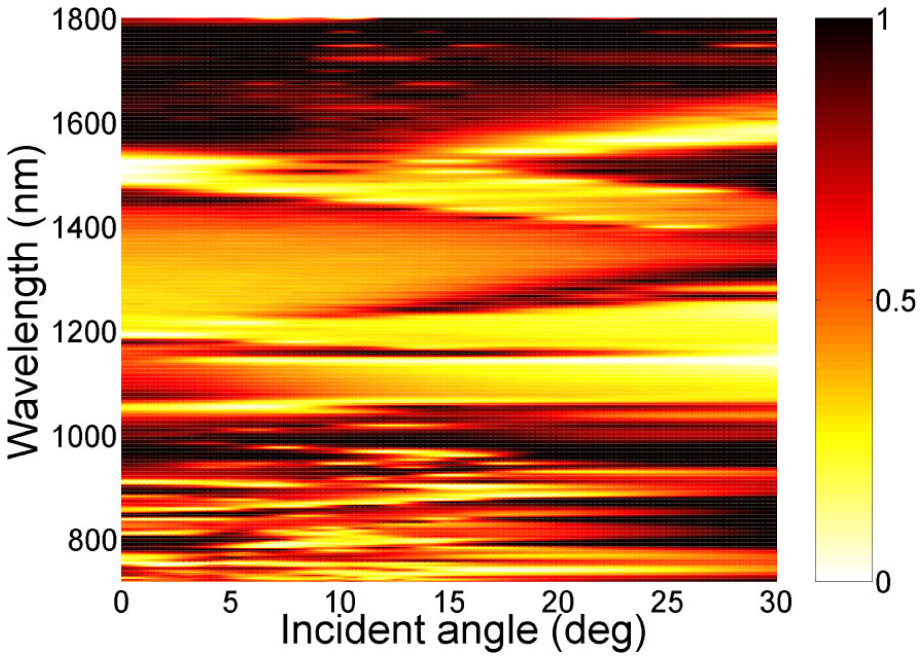


**Figure 2.8:** 2D GaAs PhC light transmission spectrum with $r = 233.4$ nm, $t = 301.5$ nm.

and 1519 nm, in good agreement with the target values, which confirms that our model for the design is accurate and effective.

Quadratic polynomial fitting was used to adjust the structural parameters. Increasing the order of simulation can further reduce the system error, and hence better the leaky mode simulation. In addition, precise spectral overlap can also be realized by adjusting the incident angle with respect to the S-polarized light transmission spectrum shown in Figure 2.8, in which incident angle $\theta$ along the $\Gamma - \mathrm{M}$ direction was changed. The thickness of this photonic crystal is $t = 301.5$ nm, the hole radius $r = 233.4$ nm, and the other parameters remain unchanged.

To see the influence of the resonance phenomenon in the near-field, we simulate the near-field electric-field intensity distribution at the two surfaces of the slab for the excitation of the leaky modes (resonance) at $\lambda_{em}$=1519 nm and $\lambda_{ex}$=1492 nm, respectively,

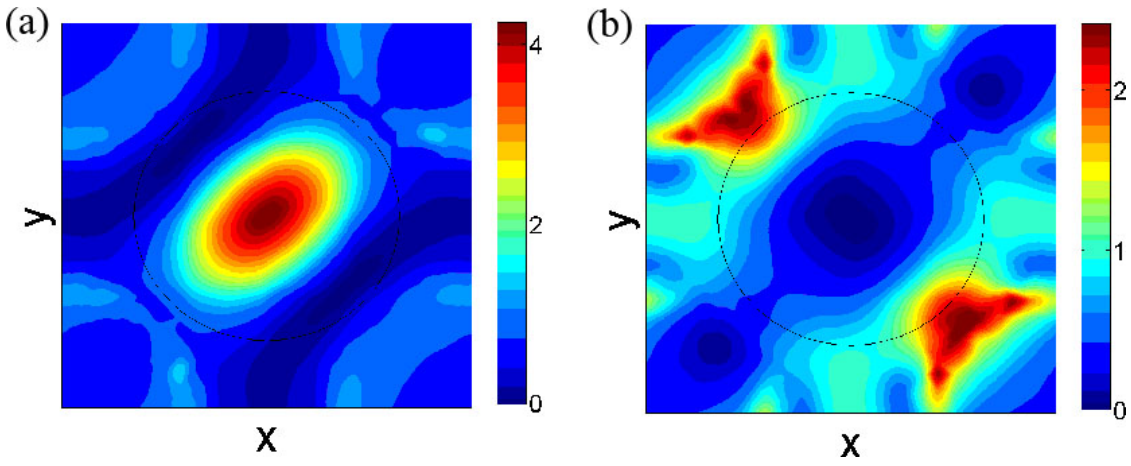


**Figure 2.9:** Calculated near electric-field intensity ($E^2$) for the lower (a) and upper (b) GaAs slab surfaces with the incident light at 1519 nm.

as shown in Figure 2.9 and Figure 2.10. In both cases, S-polarized light at normal incidence is used, and the intensity of the near-field is normalized to unit amplitude of the incident light field. Figure 2.9 (a) and Figure 2.10 (a) are for the lower surface where the resonant mode concentrates its energy within the cavity region while Figure 2.9 (b) and Figure 2.10 (b) are for the upper surface, at which the energy is distributed at the cavity periphery and beyond. It is clearly seen that the resonance results in the enhanced near-field electric-field intensity at the both wavelengths simultaneously. Therefore, the leaky modes of the PhC can be designed to couple with the excitation and emission peaks of $Er_3N@C_{80}$, offering the optimal conditions to enhance the fluorescence emission.

The method discussed above for designing such as photonic crystal cavity to achieve resonance of a leaky mode with the excitation and emission energy of fluorescent material to enhance the PL emission can be extended to other optical solid state materials, such as QD-cavity materials that we are going to introduce from next chapter. The MEEP package will be mentioned many times throughout this thesis. Single-walled carbon nanotubes have absorption at 575nm and emit through $E_{11}$ at 1000nm (6,5 nanotubes).

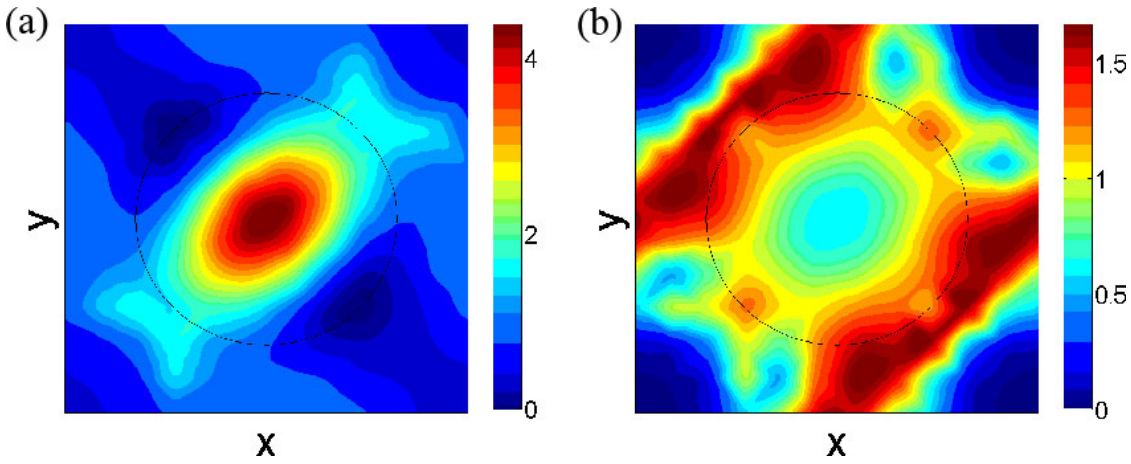


**Figure 2.10:** Calculated near electric-field intensity ($E^2$) for the lower (a) and upper (b) GaAs slab surfaces when the leaky mode at 1497 nm is excited using s-polarized light at normal incidence. The circular regions on the images show one period of the lattice.

The same operation can be undertaken to meet the leaky mode matching of nanotubes [49] .

# Chapter 3

# Towards CQED with InAs/GaAs quantum dots

The two-level system in Quantum dots (QDs) behaves as an "artificial atom" and QDs emit sharp PL lines which can be observed by micro-spectroscopy. A few thousands of atoms assemble to form QDs to make them normally around $\sim 6-20$ nm in height and several tens of nanometers in diameter. This 3-dimensional confinement guarantees their possible application for optical quantum information processing. Several different aspects of QD experiments are described in this Chapter.

## 3.1 Quantum dots

### 3.1.1 Quantum dots growth

Thanks to the invention of molecular beam epitaxy (MBE) in 1966 at Bell Telephone Laboratories [50], precision growth and deposition of atomic monolayers is now a critical part of many modern semiconductor devices.

The solid-sources used here are kept under ultra-high vacuum (UHV) and mounted

in furnaces called Knudsen cells, and gaseous components such as N are generated by a plasma cell. The heated sources slowly sublimate and are directed towards a heated substrate. The UHV environment is critical for MBE so that the associated mean free paths are sufficiently long, that the evaporated vacuum chamber gases do not interact with each other until they reach the wafer. The epilayer (morphology of the deposited film) is determined by the substrate material, crystallographic orientation and growth rate, which can be monitored and controlled with *in-situ* diffraction techniques such as reflection high-energy electron diffraction (RHEED) [51].

In III-V compounds such as GaAs, AlAs and InAs, the different lattice parameters of the constituent components result in a lattice mismatch and strain at the interface. This build-up strain becomes energetically favourable for the adatoms to form 3D-like structures beyond a certain critical thickness. InAs/GaAs QDs are obtained by strain-driven nucleation in the Stranski-Krastanov (S-K) growth mode. Our collaborator at Imperial college grew the samples in a similar fashion to that described in [52]; the MBE fabrication and subsequent atomic force microscopy (AFM) characterization was performed at Imperial College London. Characterization was undertaken as part of this thesis at Oxford.

The natural growth dynamics decide the morphology of individual QDs, whose diversions vary, changing their optical properties. However, reproducibility is commonly achieved with similar dot densities and statistical distributions of QD sizes and shapes. Take a standard growth process as an example. After oxide absorption, a 100 nm GaAs buffer layer was grown under As flux. Then 1.8 ML of InAs was sublimated to form QDs at 500°C with growth rate of 0.0015/MLs, followed by 60 seconds of annealing under an As flux at 500°C. The stored strain energy gets larger and the elastic energy is relaxed via the formation of self-assembed 3D islands, which become the desired QDs. A slow growth rate is very important as described in [52], due to the increased migration length

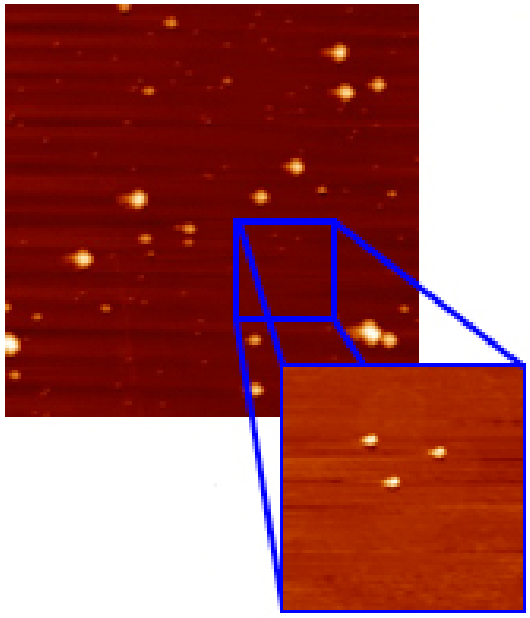

**Figure 3.1:** AFM image of self-assembled InAs QDs with image size of 5$\mu$m $\times$ 5$\mu$m. The dot density is $3 \times 10^8 \text{cm}^{-2}$. The zoomed image is 1 $\mu$m $\times$ 1 $\mu$m.

of In adatoms incorporating into existing dots rather than forming new dots, hence resulting in larger dot sizes. The formation of 3D islands on the GaAs layer arises from a release of strain energy according to the S-K growth mode. AFM was used to study the surface of the QDs layer as shown in Figure 3.1. Low density QDs were achieved and large InAs islands were seen.

### 3.1.2 InAs quantum dots

The emergence of quantum information processing (QIP) has demanded the development of reliable single photon sources. Most studies have focused on dots emitting below 1000 nm range, which can be attained with standard growth protocol. However, fiber-based

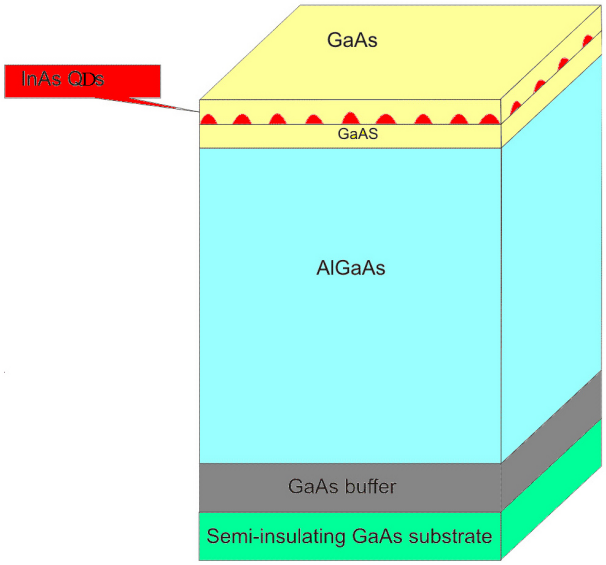


**Figure 3.2:** InAs/GaAs QDs fabrication illustration.

QIP requires 1300 or 1550 nm transmission window. Figure 3.2 shows a schematic view of the growth of the QDs we use. In these low energy interface structures, the strain energy increases with the thickness of the epilayers. Given the self-assembed nature of the S-K mode, the fabricated QDs are randomly located. The GaAs cap at the top of the structure is used to redshift the QDs' emission. Note the sacrificial AlGaAs layer fabricated above the GaAs buffer and below the dots is necessary for the production of an air bridge in photonic crystal structures, which will be addressed more detail in Chapter 4. The structure depicted above is only a typical sample we used. Various growth schemes were adopted with different epilayer thickness or cap-layers such as InGaAs caps, in order to optimize the optical performance of the QDs.

### 3.1.3 Excitation and emission

Here we consider a particular transition in a bulk semiconductor. In an absorption process, electrons are promoted to the conduction band and holes are left behind in the

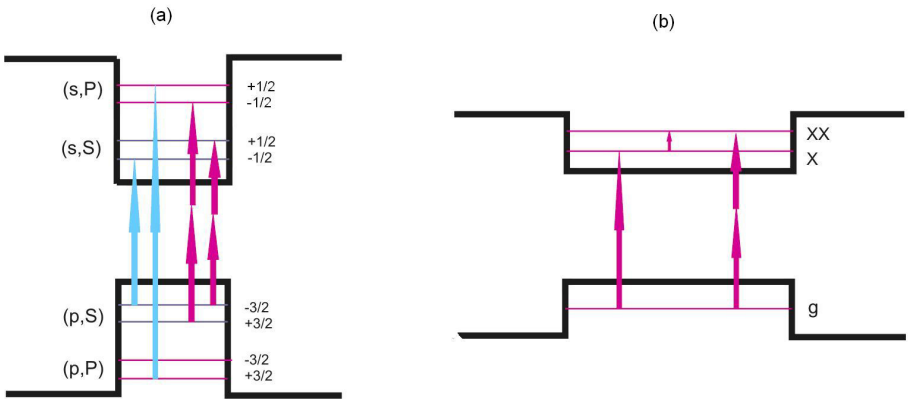


**Figure 3.3:** Simplified schemes of optical transitions from different single photon sources. (a) Electron and hole confined states in a QD. The left indices show the band and envelope orbital symmetries, respectively. The right indices indicate the spin states. (b) Electron and hole confined states in a bigger QD compared with (a). Excitons and biexcitons are indicated. It should be noted that only absorption is illustrated in (a) and (b).

valence band. Electron and hole pairs can bind to form complexes known as excitons and the electrons and holes recombine by emitting photons.

In the case of quantum dots, the atom-like discrete nature of the energy levels generates promising interband transitions. As in the simplest picture of the energy levels shown in Figure 3.3 (a), electrons and heavy holes populate the conduction band and valence band, respectively. Transitions are allowed when the overall symmetry of the two states are different, such as the transition (p,S) $\longleftrightarrow$ (s,S). Excitons are formed due to Coulomb interactions between the carriers. The so-called dark excitons in contrast with bright ones cannot recombine optically due to quantum selection rules. Schematically, the transition (p,S) $\longleftrightarrow$ (s,P) is not allowed. However, in processes such as two photon absorption (TPA), the dark transition can be observed. As more carriers are excited into the QD, a second exciton can be created which can interact with the first forming a state known as a biexciton (XX) as illustrated in figure 3.3 (b). The linear dependence

of the exciton on excitation power becomces quadratic for XX since every transition has to capture two electon-hole pairs. The repulsive Coulomb interaction between excitons and biexctons leads to the binding energy decreasing with increasing exciton transition energy [53].

In the arsenide-based dot systems we studied, the infrared band gaps means that excitation can take place using a tunable Ti:Sapphire laser system or a higher energy laser source such as a He-Ne laser. Non-resonant excitation creates many electron-hole pairs in the material matrix surrounding the QDs. Relaxation to the lowest energy confined states in the QDs follows. A pulsed Ti:Sapphire laser was used for time-resolved measurements and we normally set this laser to continuous wave laser mode for time-integrated PL excitation.

## 3.2 Characterization of single quantum dots

Photoluminescence (PL) measurements were carried out on a high InAs dot density sample with 100 dots/cm$^2$. The idea of $\mu$PL spectroscopy is simply to optically excite the sample and collect the PL. Micro ($\mu$) here means the laser spot is always around 1 $\mu$m, so we are exciting a small area of the sample and hence a single or a few nanostructures. We mainly use time-integrated PL measurement (TI-PL) to investigate samples in the spectral domain. We briefly introduce our experimental system as shown schematically in Figure 3.4 and then follow the experimental results.

### 3.2.1 Laser sources

The He-Ne laser used in our work is for optical alignment and PL excitation. In the laser reservoir, Neon is excited by high voltage and with the assistance of Helium, produces a continuous coherent monochromatic beam.

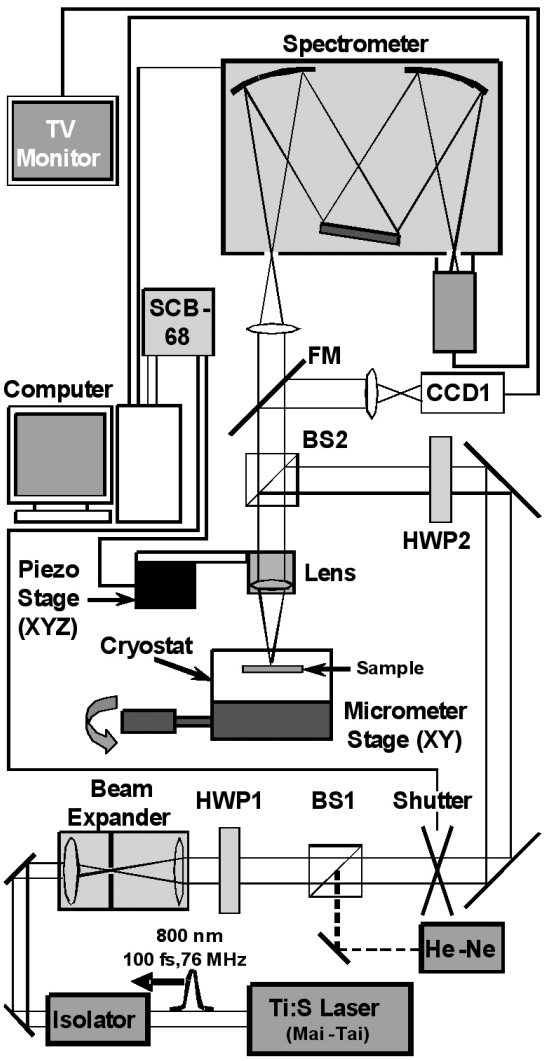


**Figure 3.4:** Schematic diagram of the system used to perform Two Photon Absorption laser photolithography and micro-photoluminescence spectroscopy.

A MAI TAI Titanium:Saphire (Ti:S) based ultrafast laser (100fs pulses) with about 1 W output power is also used. The Ti:S Oscillator is pumped by a neodymium:yttrium vanadate (Nd:YVO4) diode-pumped solid-state laser and mode-locked at a pulse width of 120 fs with 80 MHz frequency.

Different laser system are applied mainly because the various requirement of the

excitation of our sample bandgaps. For example, Other laser sources have also been used in our experiments including a green frequency-doubled YAG laser and a tunable dye laser.

### 3.2.2 Spectrometer

A spectrometer disperses light into its spectral components using a Czerny-Turner design, which measures the lifetime and intensity of incident light dispersed by gratings. The Spectrometer used in our work is an Andor Technology produced Shamrock SR-303i-B. The light is collimated through a spherical mirror onto the input slit. Each spectral component arrives on the focal plane as separated images with each image corresponding to a given spectral component. The Samrock is an imaging spectrometer, with each spectral component being an exact 1:1 image of the focused spot on the entrance slit. 3 gratings with different ruling disperse the light. Finally the beams were focused on our iDus InGaAs diode array or a Si CCD detector.

A particular experiment requires the consideration of spectral resolution and acquisition time. Higher spectral resolution demands a smaller input slit, hence less light passes through the instrument. This can be compensated by using a longer acquisition time. The reciprocal linear dispersion of a spectrometer is given by:

$$\frac{\mathrm{d}\lambda}{\mathrm{d}x} = \frac{\mathrm{d}}{\mathrm{L_F}}$$

where $\mathrm{L_F}$ is the focal length of the spectrometer, d is the grating spacing, $d\lambda$ is a small change in wavelength and dx is the corresponding position of the dispersed light. A 2.78 nm/mm reciprocal linear dispersion could be obtained with the 0.3 m spectrometer and a 1200 grooves/mm grating. The resolving power R, given by:

$$R = \frac{\lambda}{\delta\lambda}$$

can be as small as 0.2 nm at 400 nm.

Modern spectrometers are well designed electro-mechanical devices driven by computer through IEEE-488/GPIB or USB interfaces to control the entrance slit width and the grating turret, etc. We have 300 groove/mm, 600 groove/mm and 1200 groove/mm gratings fitted to the same turret. These features were fully adapted to fulfill the requirements of our experiment.

### 3.2.3 InGaAs diode array

A multichanel array is usually a semiconductor chip with two-dimensional photon sensors or pixels. The Andor iDus InGaAs 490-1.7 camera has 512 pixels with 26 $\mu m \times 500 \mu m$ (W×H) pixel size. When an incident photon reaches the surface of the chip, electron-hole pairs are produced and through a series of electrodes on the chip these are then amplified and shifted to the output to be read by a computer connected using USB. This array is especially designed for IR spectroscopy and has good efficiency from 0.8 to 1.7 $\mu$m.

Most of the noise in diode arrays can be classified as pixel noise and fixed pattern noise arising from readout repetition for a thermal dark signal. This dark signal is produced by thermal excitation of carriers over the bandgap and the dark current thus varies with the temperature of the detector. By cooling the equipment down we can reduce this dark signal. iDus arrays can be cooled by water or air using Peltier cooler to $-87^{o}$C.

### 3.2.4 Superconducting nanowire single photon detectors

Superconducting nanowire single-photon detectors (SNSPDs) have a sensitive range from visible to infrared with low dark counts, operating between 1.5-4 K with ultrathin niobium nitride nanowire. The superconducting wire with fast photoresponsive properties [54] is biased just below its critical current. When a photon is directed onto the detecting head, a resistive hot spot in the nanowire triggers a current pulse that can be measured. [55] [56]

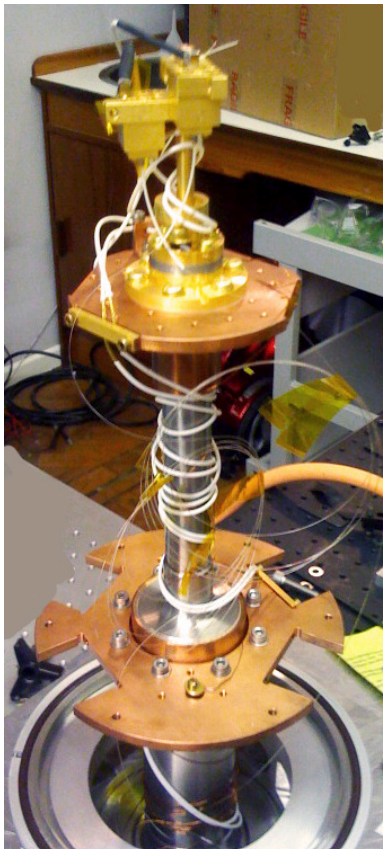

**Figure 3.5:** Inside the superconducting nanowire single photon detector.

A basic meander-type SNSPDs82 with a commercial Sumitomo Heavy Industries RDK-101D 4K cold head was fabricated for our experiment, and is shown in Figure 3.5. Fibre-coupled SNSPDs can be integrated into two-stage closed-cycle refrigerator systems. A continuous refrigeration achieves 40K - 60K at the first stage and a further closed-cycle cools the second stage to 3K [57]. The next-generation of high-efficiency SNSPDs with integrated cavity designs will improve the detector efficiencies above the 1% standard achieved in our device [56].

### 3.2.5 Actuators

Samples are placed in a Janis ST-500 microscale cryostat. Cooling the sample to around 4.2K achieves a better quantum efficiency of photon generation owing to reduced electron-

phonon interactions. Piezo materials convert electrical energy to mechanical energy and vice versa. The cryostat is fixed on a movable XY micrometer stage. A 100× IR optimized microscope objective with $N.A.$ 0.5 is used to collect the emission and this is controlled by a E$-$611.3$S$ piezo stage with an $E-664$ controller applying a $0-100$ V voltage to induce a 0-100 $\mu$m range at travel. The resolution is determined by the 16 bit A/D card which generates the voltage that is applied to the analogue controller. The absolute position of the stage is determined by in-built gauges given an accurate positional signal.

### 3.2.6 Quantum dots PL spectroscopy

Using our experimental setup, Figure 3.6 shows PL spectra from five IR QDs samples with slightly different growth recipes in an effort to achieve the lowest possible QD density with the highest emission wavelengths. Sample A was grown as described previously with an extra 4 nm InGaAs cap in order to extend the emission to ∼1300 nm at low temperature. It has a rather low QD density of ($\sim 5\times10^{8}/\mathrm{cm}^{-2}$). However, to achieve the patterning with a photonic crystal (PhC), a layer of AlGaAs is also needed, which we will discuss in Section 4.3. Sample B and C are high ($\sim2\times10^{9}/\mathrm{cm}^{-2}$) and low ($\sim5\times10^{8}/\mathrm{cm}^{-2}$) density samples including the AlGaAs sacrificial layer, respectively. Unfortunately these samples show lower emission wavelength of approximately 1200 nm due to imperfections in the growth rate calibrations. High and low density samples D and E are promising as our study objectives. In addition, it is rather easy to locate single quantum dots in sample E, which we will discuss in Section 3.3.

### 3.2.7 Single quantum dots

In order to achieve effective coupling between a QD exciton and a PhC defect optical mode, we need to be able to locate the position of the single QD. This is rather difficult to achieve not only due to the small size of the QD but also because our optical measurement

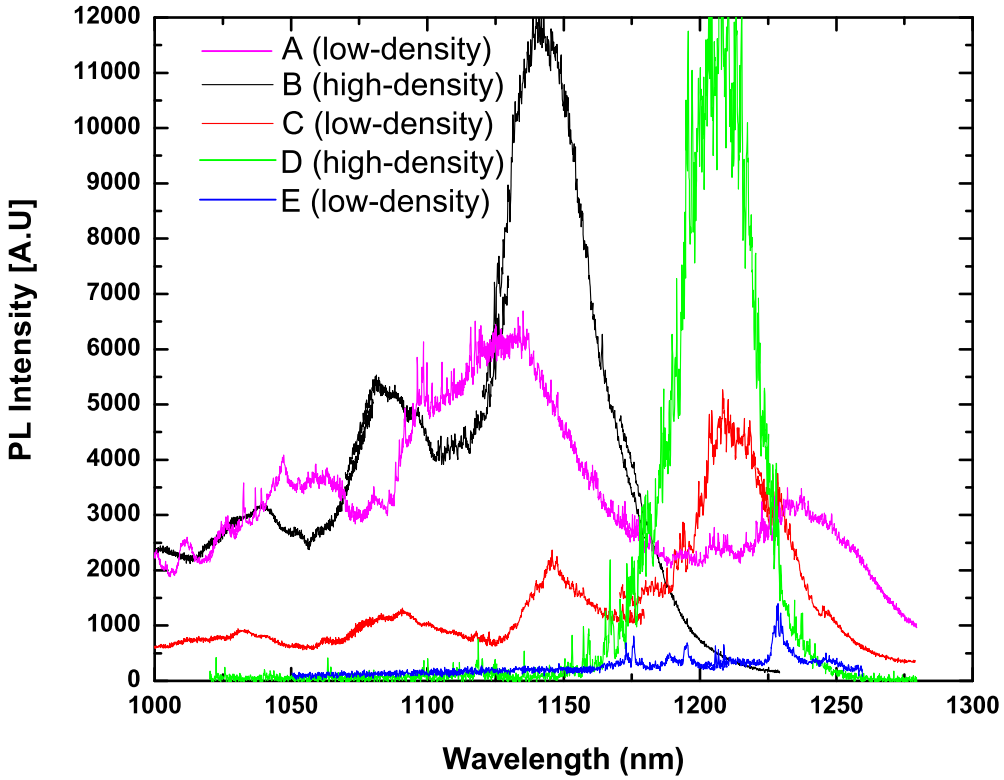


**Figure 3.6:** Photoluminescence from various QDs samples. For visualization, samples are plotted here under the same scale but with different power and acquisition time. The powers applied to samples A-E are 210$\mu$W 2s, 160$\mu$W 5s, 160$\mu W$ 5s, 50nW 40s and 60$\mu W$ 10s, respectively.

is greatly affected by thermal drifts. The latter requires constant spatial PL maps on the QD of interest [58]. Here we developed an Andor Basic program to spatially map the QDs. Power-dependent PL measurements are presented in Figure 3.7. The sharp, atom-like peak at 1237 nm is the signature of single QD emission. Many single dot peaks were measured in order to find a relative higher emission-background contrast. This particular single dot exciton emission is saturated at 50 $\mu$W.

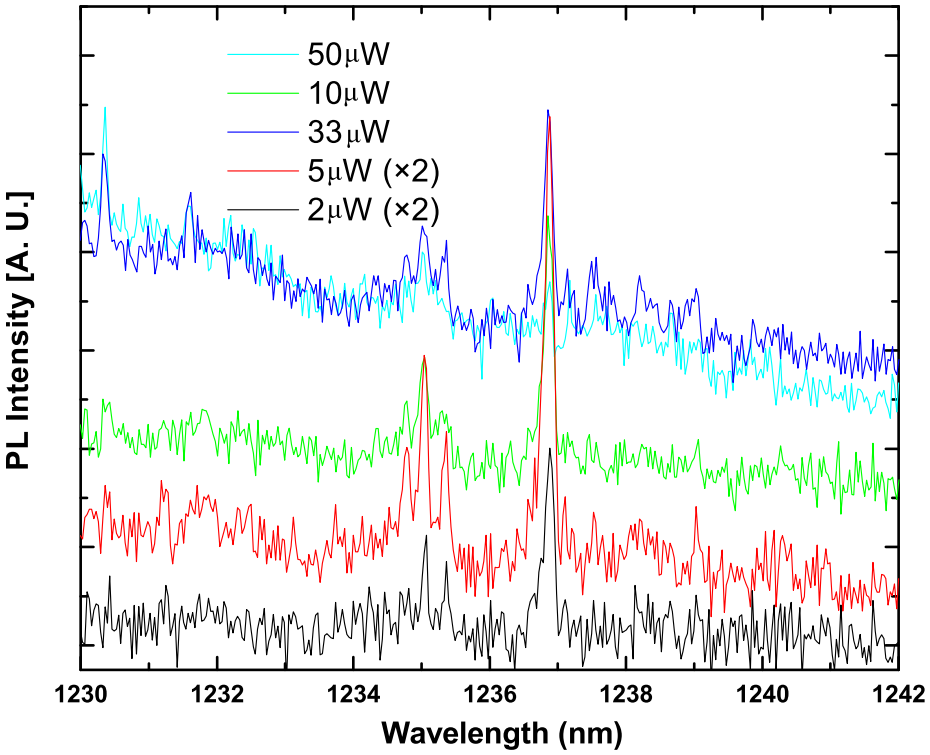


**Figure 3.7:** Power dependent PL measurements from a single QD exciton, clearly showing the higher excited states in the dots.

### 3.2.8 Spectral line shape

As shown in Figure 3.7, clear distinguishable peaks originate from the discrete, delta-like density of states of QDs. The increase of the height of QDs in monolayer greatly affects the upper and lower energies of the band edges. The minimum FWHM of an emission line is determined by the radiative decay rate, and hence the lifetime. Theoretically, the homogeneous broadening of each quantum dot, referred to as the natural spectrum linewidth, is dominated by the spontaneous emission rate and carrier scattering rate [59]. The shape of the QD emission has a strong dependence on the power used for

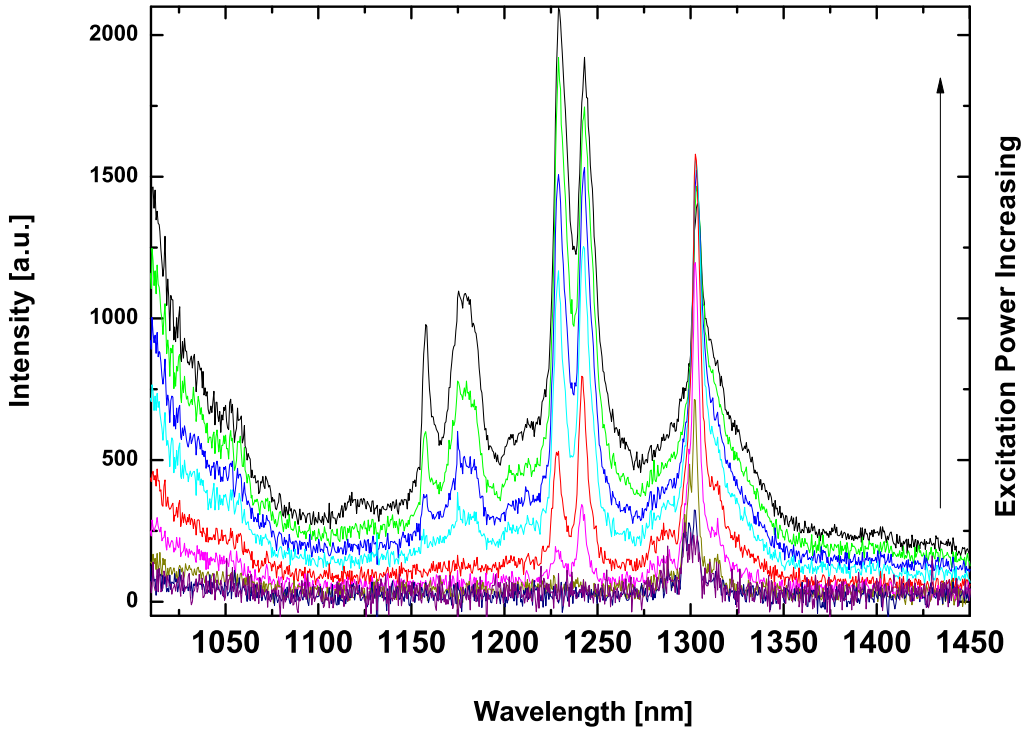


**Figure 3.8:** Power dependent PL measurements from a QDs sample.

excitation and takes the form of a Lorentzian bell curve. Under a high excitation regime, biexcitons can generally be distinguished from excitons by their quadratic dependence on the excitation density. This Coulomb interaction is particularly important for InAs QDs for which the confinement induces the local charge separation due to the inhomogeneous strain. Phonon assisted relaxation (the phonon bottleneck effect) and the so-called state filling effect arising from selection rules that populate the lower states with a few carriers also lead to the observation of the higher energy peaks [60]. These new peaks are observed in Figure 3.8 when higher excitation is applied.

## 3.3 SU-8 single quantum dots positioning

Quantum electrodynamics (QED) is a sophisticated branch of physics dealing with coherent interactions between an atom (i.e. an emitter) and electro-magnetic fields. The Jaynes-Cummins model describes this type of light-matter interaction [15]. Cavity QED (CQED), as the name states, describes the interaction of an atom inside a cavity with the cavity modes and can enhance the photoluminescence of atoms positioned at the anti-nodes of the cavity. A more detailed discussion can be found in Refs. [16, 17] and will be discussed more fully in the next chapter.

### 3.3.1 SU-8 lithography and quantum dot registration

We introduce a promising technique to spatially and spectrally register the position of QDs. This method involves two photon absorption (TPA) laser lithography using SU-8 photoresist patterned at cryogenic temperatures. SU-8 is widely used in the micro-electromechanical system community as a negative photoresist [61]. Figure 3.9 demonstrates this process. Firstly, a tungsten metallic layer was fabricated on the surface of an InAs QD sample. The mask consists of exposed 15×15 $\mu$m squares formed using optical lithography on a positive photoresist (Shipley S1813). A grid of apertures with a 100 $\mu$m spacing was created. This space was then developed with aqueous-based Shipley MF-319 and treated with chlorobenzene vapour so that a 60 nm thick sputter-deposited tungsten layer was obtained. Tungsten is chosen, as it is removable by reactive ion etching (RIE) and has good visibility under electron beam machine (e-beam) illumination due to its high atomic number. After spin-coating SU-8 on tungsten at 3000RPM for 60 seconds, we baked the sample at 95°C for 2 minutes to form a 1 $\mu$m thick resist layer. The sample has to avoid UV light due to the possibility of premature exposure of the resist [62].

A single QD was located by conducting a 2D scan on the different apertures of the tungsten mask ($\sim$10×10$\mu$m). We aligned the optical path with the intention of obtaining

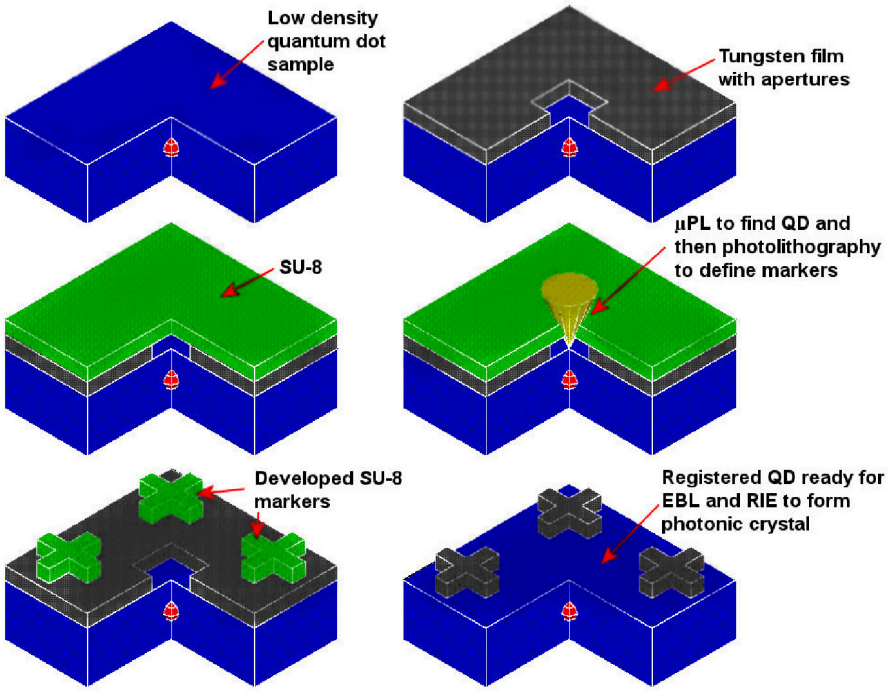


**Figure 3.9:** A schematic illustration of the TPA lithography process.

the highest available power from the Mai Tai laser for the TPA processes. A Labview program for registration was used to write the designed patterns. Figure 3.10 shows the registration results measured using a scanning electron microscope (SEM). 10 $\mu$m crosses (separated by a distance of 40 $\mu$m) surround the location of the QD. There is also a 5×5 $\mu$m box written at the four different corners of the crosses to identify and register the position of each dot. The speed of the registration was as fast as possible to avoid thermal drift in the system. The centre of the 4 crosses points to the position where the PhC cavity would be fabricated.

All PL and photolithography processes were undertaken at 4K. The exposed samples were then warmed up to room temperature and baked at 95°C for 5 minutes to form polymers. After 5 minutes of cooling, propylene glycol methyl ether acetate (PGMEA) was used to dissolve any unpolymerised resist and the sample was blown dry.

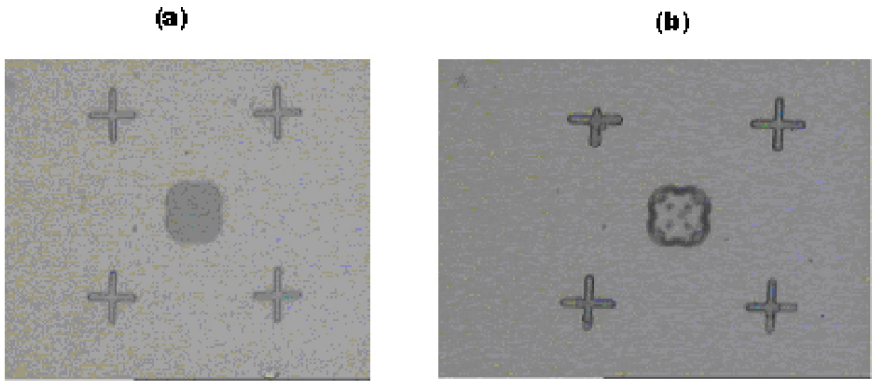


**Figure 3.10:** QD registration results prior to RIE. (a) Perfect pattern design. (b) An unsatisfactory result where the exposed cross has either detached from the surface during development or was not exposed properly.

Prior to the PhC fabrication, the pattern was cleaned with a 20 sccm, 100 mTorr, RF 250 W and 440 V DC Ar plasma for 30 seconds. The clean pattern is transferred to tungsten layer by RIE using a total flow of 44 sccm $CF_4$:$O_2$ 10:1 gas mixture at pressure of 20 mTorr, RF 250 W, 480 V DC for 1 minute [62]. The last step involves removing the remaining SU-8 by using an $O_2$ plasma ashing at 20 sccm, 20 mTorr, 250W and 540 V DC for 2 minutes.

### 3.3.2 Discussion on SU-8 adhesion and problems

A high laser power has a crucial effect in inducing TPA processes. Before registering QDs using TPA on SU-8, we did several power dependent measurements on GaAs samples coated with SU-8 using an excitation range from 120 mW to about 10 mW into the microscope objective as shown in Figure 3.11. The best exposure results occurred at about 33 mW where the markers were thick enough without being broken. However, in the registration process using QD samples, unsatisfactory exposure results still appeared and we generally attributed this to contamination of QD samples before SU-8 coating.

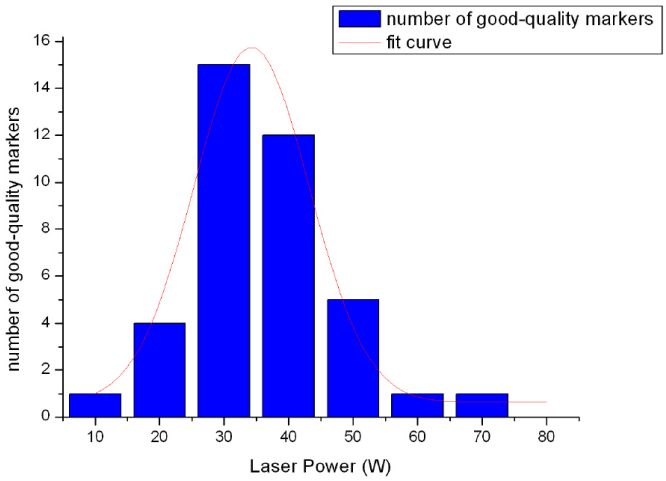


**Figure 3.11:** High quality registration numbers over laser power. The fitted curve shows that the best power is around 33 mW.

For instance, in Figure 3.10(b), the top left cross has its top branch missing and the bottom crosses also have parts missing.

The SU-8 adhesion seems to be good, but the residuals on top of the sample become a major problem due to contamination that seriously affects the visibility under e-beam lithography. When we develop SU-8 with PGMEA and rinse with IPA, the IPA might not be cleaned completely and blowing the sample dry also creates dust. Another issue can be silver dag or dirt contamination from the surrounding environment: a perfectly clean sample could not be obtained. However, this disruption can be reduced to a minimum by being careful during SU-8 spinning and developing.

## 3.4 Scan quantum dot positioning using a new scanning techknoledge

The difficulties we met in the SU-8 method led us to a new all-optical method to measure the positions of single QDs. Performed on very low QD density samples, this deterministic

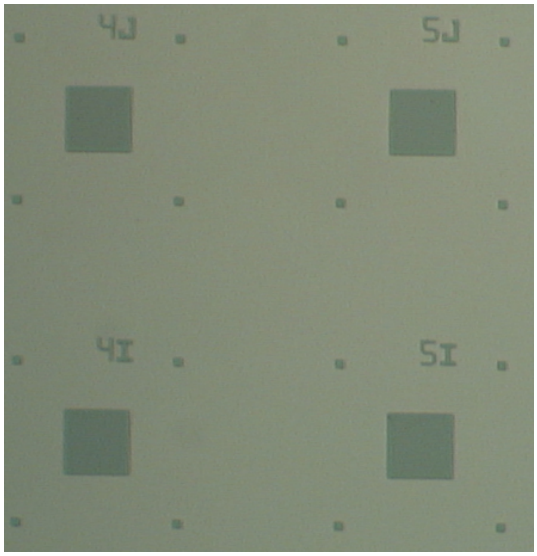


**Figure 3.12:** SEM image of a scanning pattern.

method can precisely locate the position of the desired QD relative to the surrounding markers.

### 3.4.1 Locating quantum dots

One can locate the transition point in a step-varying system disregarding the scanning laser itself by fitting a Gaussian curve to the differentiated scanning data. We can also locate the centre of the QD relative to a reference edge by fitting the centre of the mission peak and taking an the average over many scans.

After identifying an ideal wafer of suitable QD density, we sputter coated a 60 nm thick tungsten layer. A pattern comprising 80 $\times$ 80 $\mu$m apertures together with 4 surrounding 10 $\times$ 10 $\mu$m squares was fabricated as shown in Figure 3.12. e-beam lithography using PmmA as a resist was used to produce the patterns. At the end we developed and etched the sample to create the openings as described in the previous section.

The QD has to be chosen sufficiently far away from the edges of the aperture to avoid interference with the photonic crystal being patterned. An aperture size of 80 $\mu$m is

reasonable and suitable for our piezo stage's 100 $\mu$m scanning range.

### 3.4.2 Results and discussion

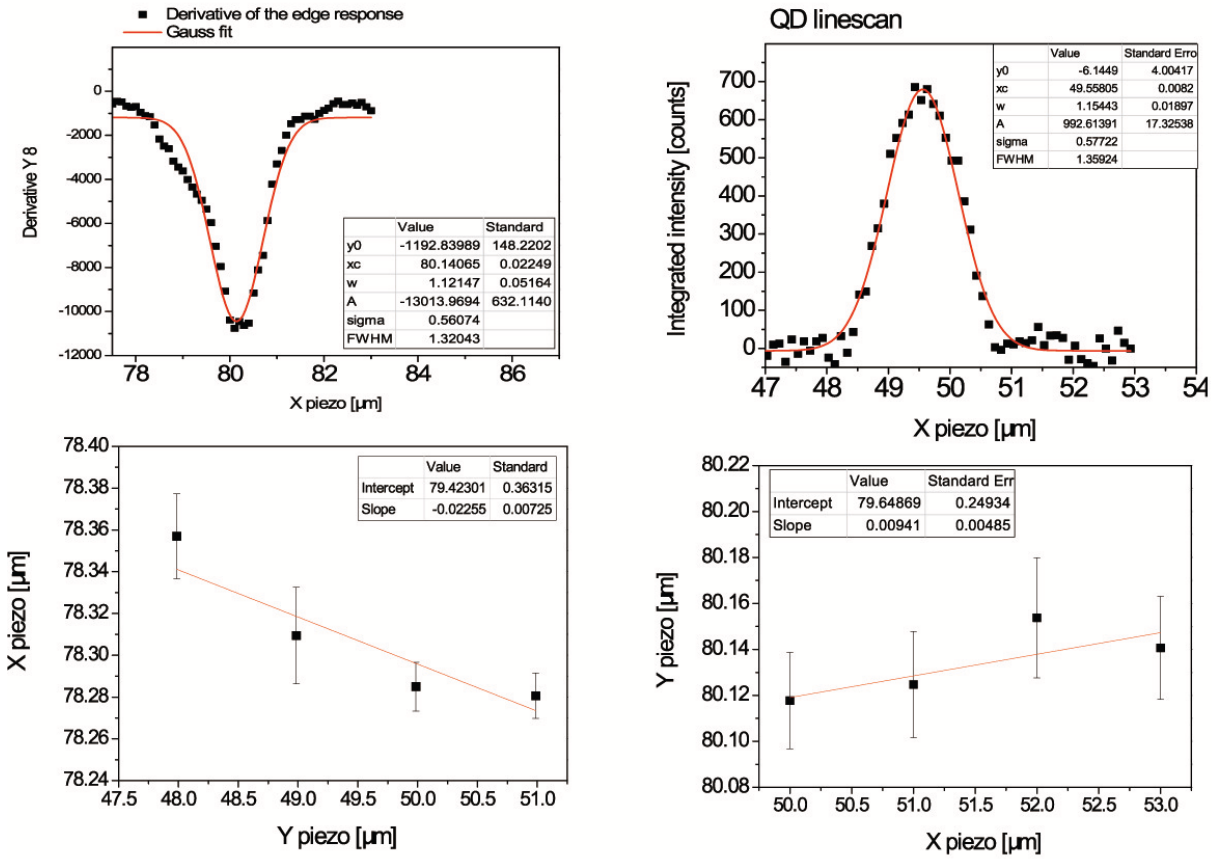


**Figure 3.13:** Gaussian fits to the scanning data.

The sample is mounted in the Janis ST-500 cryostat and cooled down to 4.2K, and an 800 nm Ti:Sapphire laser is used to excite the carriers. Excitation and emission are both collected through an infrared high resolution microscope objective mounted on an $xyz$ piezo stage with the InGaAs Array detector, and successive scans of the laser beam over the chosen quantum dot's emission window were taken in the $x$ and $y$ directions, respectively. This then enabled the dot position to be determined with an accuracy of

50 nm. With the same program we moved the laser beam towards the edge of the 80 $\mu$m pattern. The reflection spectrum identifies the position of the edge because of the different reflectivity of Tungsten and GaAs.

After differentiating the emission profile, the scans were fitted by Gaussian curves. An example of these fitted curves is shown in Figure 3.13. The peak of the fitted line is where the edge of the square is and the line below is the average of four scans, thus we can plot where the edges are regarding to QDs. Then we should be able to directly detect the edges and write the photonic crystal patterns using an e-beam machine. In general, we could limit the QD registration accuracy within 120 nm. Obviously, the more scans undertaken the more accurate the results would be. In fact, authors have demonstrated [63] that thirty scans over the same edge yield a statistical error of only 5 nm. The actual PhC writing on a registered QD is currently undergoing. However, devices based on high density QDs will be introduced in the next chapter.

# Chapter 4

# Light-matter interaction

## 4.1 Cavity quantum electrodynamics

Modern CQED has more than fifty years accumulated knowledge of cavity design and atom manipulation. Following Section 3.3.1, we will discuss here the details of a study into solid state CQED(SS-CQED).

The coupling of an atom in free space with vacuum radiation modes decides the atom's radiative properties. The atom's spontaneous emission itself is determined by the coupling of excitons (in the case of solid systems) to resonant field modes. At first, it was believed that the quantum fluctuations of the vacuum field could not be varied once certain boundary conditions had been applied. Although this is true, the properties of field modes can indeed be modified and controlled by placing mirrors or conductors around the atom, hence causing the density of vacuum fluctuations to change. In other words, we can inhibit or enhance atomic radiative properties by controlling the vacuum environment.

### 4.1.1 SS-CQED: a short history

After the prediction by Purcell in 1946 [64], CQED as a newly established field has attracted a huge amount of interest from the research community. The application in optics dates from the 1990s [65] and has inspired people to combine novel types of heterostructures with photons at micro or nanometre scales.

Largely depending on MBE techniques, SS-CQED generally includes passive devices and active devices. Passive devices are various cavities, including micro-disc/pillar and photonic band-gap structures [66]. The former are fabricated by depositing layers of semiconducting materials like Bragg mirrors with different refractive indices. The latter are devices with manipulated photonic band-gaps to control the propagating light, which will be discussed in the next section.

Active components include all sorts of light-emitting diodes. Among them are quantum wells, which are two-dimensional quantum confined structures [67]. Electrons confined by energy bands perform optical transitions by means of optical or electronic excitation. Quantum dots introduced in the last chapter are considered prominent candidates due to the similarity of their energy level structures and dynamics to that of real atoms. Single-walled carbon nanotubes, which will be addressed in the next chapter are also promising candidates [4]. Other light sources include the nitrogen-vacancy centre in diamond [68] and trapped ions [69], and will not be discussed in this thesis.

With both passive and active components, the main issue then becomes how to couple the generated photons into well-defined spatial modes and out of the SS-CQED device. The light emitter has to be placed at the antinode of the cavity, which also increases the device efficiency. Spontaneous emission was found to be weakly enhanced by Tanaka et al. using one-dimensional semiconductor microcavities. [70]. A much stronger emission rate was found using three-dimensional confinement techniques, like that measured by Bayer et al. [71]. An alternative method is using photonic band structures [72] [73].

The techniques introduced above also make SS-CQED a promising candidate for QIP applications.

### 4.1.2 Coupling regimes

Figure 4.1 illustrates the basic concept of SS-CQED. The two-level emitter with dephasing rate $\gamma$ (i.e. QD) in Figure 4.1 (a) interacts resonantly with a single cavity mode with photon loss rate $\kappa$. The coupling strength between them is $g$. The QD-cavity system can be studied by a sample with high density QDs (as in Figure 4.1 (b)) embedded in a photonic crystal cavity (shown in Figure 4.1 (c)).

When the coupling strength of two same-energy oscillators is larger than mean of the oscillators' own decay rates, the system field will split into two eigenstates. The state splitting is $2g$, which follows:

$$g = \frac{\mathrm{dE_{VAC}}}{\hbar} \tag{4.1}$$

where d is the dipole moment of the single emitter and $\mathrm{E_{VAC}}$ is the vacuum field. This is called Vacuum Rabi Splitting(VRS). The vacuum field $\mathrm{E_{VAC}}$ can be expressed as:

$$\mathrm{E_{VAC}} = \left[\frac{\hbar\omega}{2\epsilon_0 \mathrm{V}}\right]^{1/2} /\mathrm{n} \tag{4.2}$$

where $\omega$ is the light angular frequency, $\epsilon_0$ is the free space permittivity, $V$ is the cavity mode volume and $n$ as the semiconductor index of refraction. In the case of SS-CQED with single emitter decay rate of $\gamma$ and a cavity decay rate of $\kappa$, the linewidths of the coupled system $[\kappa + \gamma]/2$ have to be narrower than twice the emitter-cavity coupling strength $g$ to resolve the VRS. [74]

There are two distinct coupling regimes, weak and strong. In the weak coupling regime:

$g < \gamma, \kappa$, and so the coupling of a single emitter to the cavity can either enhance or inhibit the irreversible spontaneous emission rate due to the cavity Purcell effect [64].

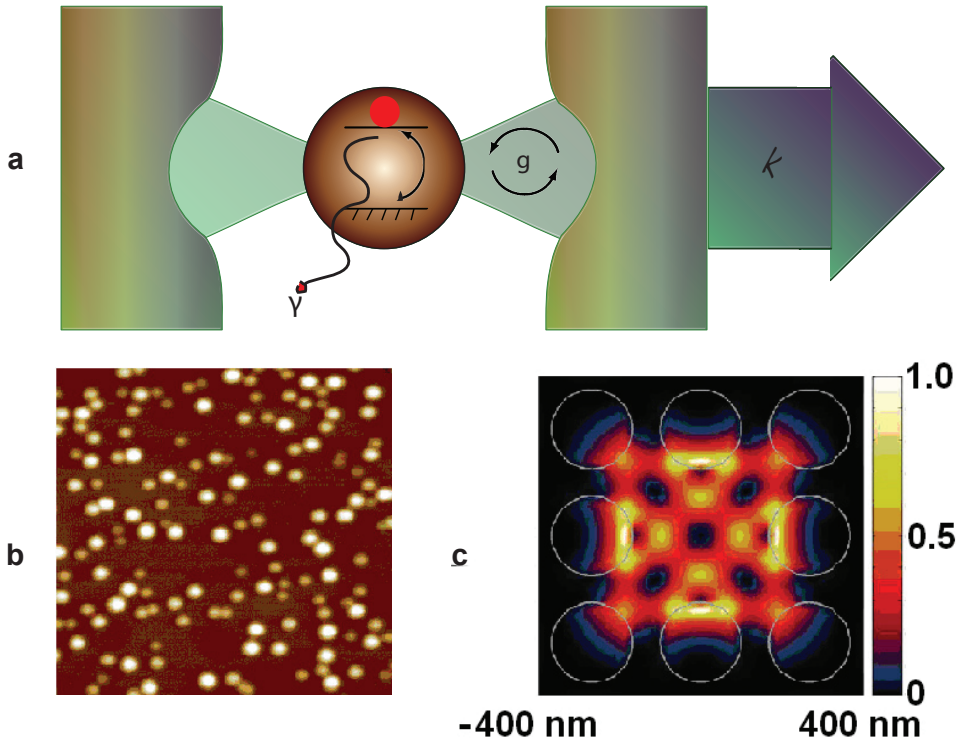


**Figure 4.1:** Fundamental concepts in CQED. (a) A schematic of a single two-level atom with dephasing rate $\gamma$ coupled to a cavity with photon loss rate $\kappa$ and coupling strength $g$. (b) The emitter and cavity mode has a spatial profile as shown in AFM data taken from X. Xu. (c) Calculated electric field energy distribution of a cavity mode.

This Purcell effect is proportional to $Q/V_{\mathrm{CAV}}$ where Q is the quality factor of a cavity which is defined by:

$$Q = \frac{\lambda}{\Delta\lambda}$$

and $\lambda$ is the wavelength of the cavity mode and $\Delta\lambda$ corresponds to the FWHM. It is obvious that increasing Q enhances the Purcell factor so achieving a high quality factor is one of the central goals of cavity fabrication. The maximum interaction requires the emitter to be located at the anti-node of the cavity mode, which also means that light

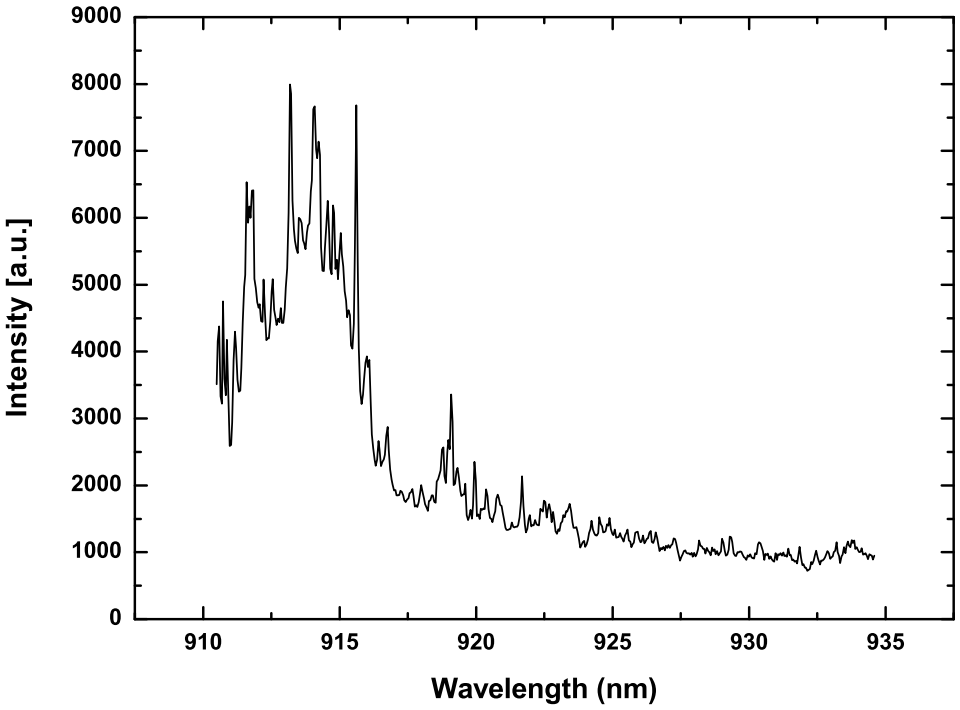


**Figure 4.2:** The weak coupling spectra.

emission for single photon sources is more reliable. Furthermore, directional emission can be achieved through the cavity output direction.

An example of weak coupling is shown in Figure 4.2. The QDs' emission as Lorentzian lines around 915nm show extreme high intensity compared to normal single QDs. In the low-Q, weak-coupling regime, the linewidth of a QD $\gamma$ increases linearly with the cavity enhancement such that $\gamma = \gamma_{dot} + \gamma_{enh}$, with the dot's natural dephasing rate $\gamma_{dot} = \gamma_{nonrad} + \gamma_0$ and the Purcell enhanced rate $\gamma_{enh} = 4g/\kappa$. $\gamma_{nonrad}$ is the dot's non-radiative dephasing rate, and $\gamma_0$ is the radiative decay rate of the QD in free space. A standard Purcell factor of about 5 is obtained from Figure 4.2.

In the strong coupling regime:

$g > \gamma, \kappa$. A reversible exchange of energy between the emitter and cavity can emerge

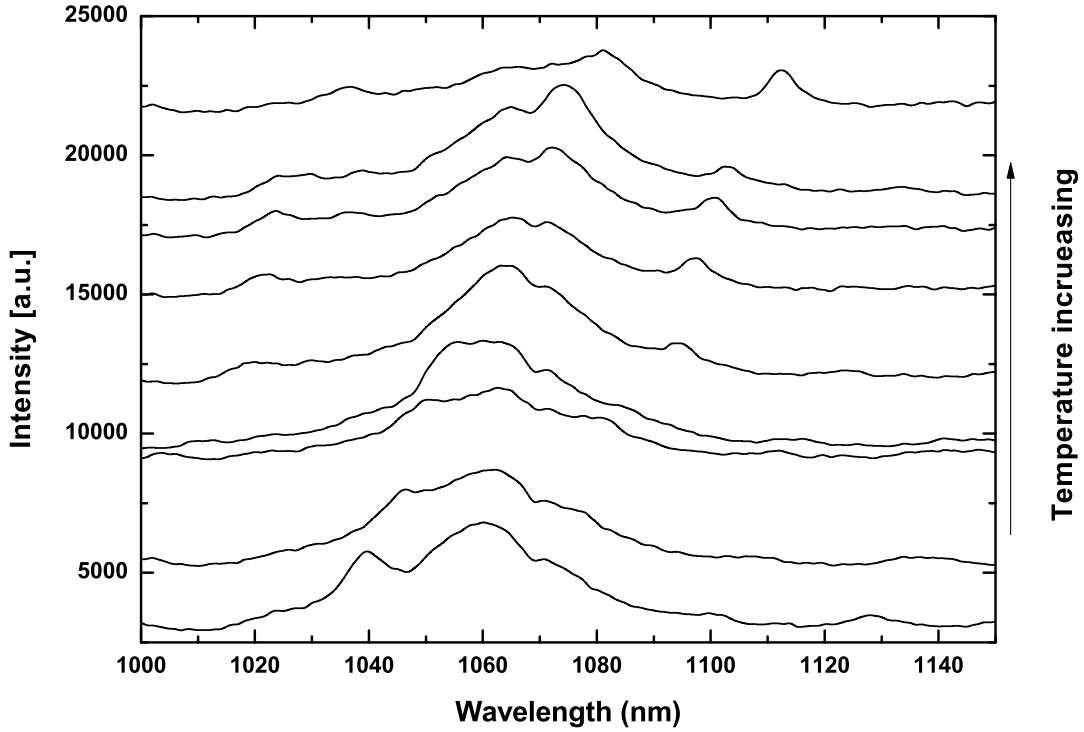


**Figure 4.3:** Anti-crossing of cavity mode and dot emission in the strong coupling regime.

when the coupling between the emitter-field is much greater than the decay rates. This VRS happens because lifting the degeneracy (anti-crossing) creates a Rabi splitting [75]. In Figure 4.3, an anti-crossing is observed by detuning the QD frequency by varying the temperature of the system. It should be noted that the observation of anti-crossing in experiments is difficult due to the necessity for high resolution. The data presented in Figure 4.3 shows an anti-crossing that is barely resolved with the resolution being limited at the point of strong coupling. The crossing point shows the sign of multiple peaks as described in [3]: a pure photonic state of the cavity.

Strong coupling is very interesting as it allows non-linear quantum optics experiments to be performed in conditions of as few as two photons [76]; direct single photon emission

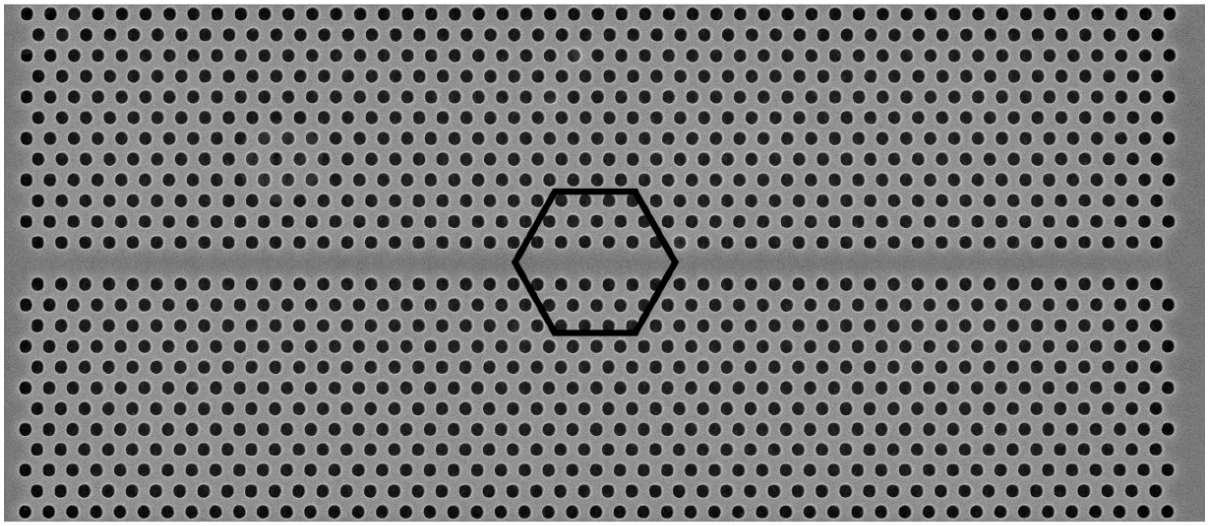

**Figure 4.4:** SEM image of a photonic waveguide.

along with single-atom lasing can be observed [28]; It can also generate entangled photons for QIP or perform quantum gate operations [77].

## 4.2 Photonic crystals

In the previous chapter, single QDs were located with respect to an L3 Photonic Crystal cavity. An ideal device using L3 PhCs with just one or a few QDs at the antinodes is highly demanding and was demonstrated by only a few groups [3] [78]. In this chapter, another type of photonic band gap structure will be addressed.

### 4.2.1 Photonic waveguide

Photonic crystal waveguide (PhCWG) cavities provide the highest $Q$ factors reported to date among microcavities which have a mode volume $V$ of the order of $(\lambda_0/n)^3$ [79] [80]. The resulting very large $Q/V$ makes them particularly suitable candidates for studying strong light-matter interactions. In addition, the PhCWG section can be tailored to

form large-scale arrays of low-loss coupled resonators with the possibility of in-line input-output coupling as recently demonstrated [81].

### 4.2.2 Device design

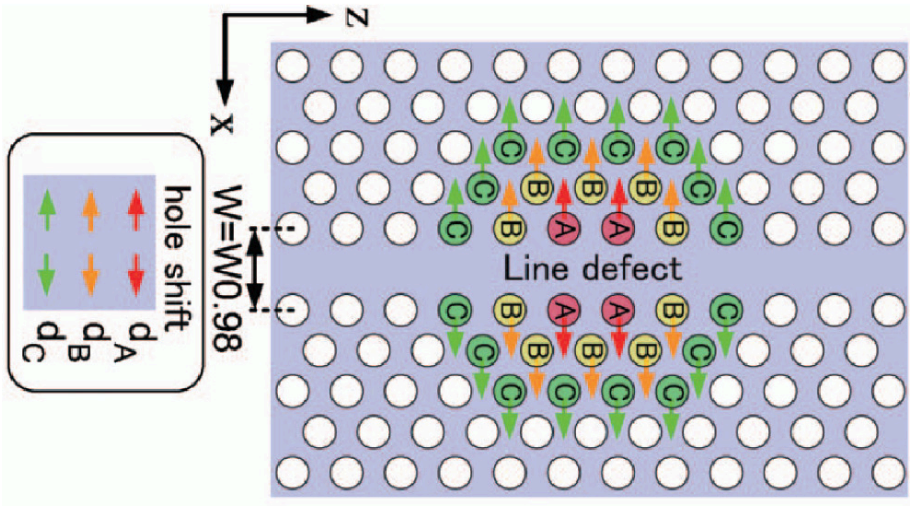


**Figure 4.5:** SEM image of the cavity embedded in a PhCWG with width W=0.98$\sqrt{3}a$ indicated by the white double arrow, where $a$ is the lattice constant. The holes are shifted within the dashed hexagon by (red arrows) 6 nm, (yellow arrows) 4 nm, and (green arrows) 2 nm in a 250 nm PhC lattice with a hole size of about 140 nm.

The PhCWG cavity studied here is based on the local modulation of the PhCWG width [80]. It was designed to emit resonantly at the low energy tail of a high dot density sample so as to limit absorption effects due to the QD ensemble and light losses related to fabrication imperfections. The holes were shifted slightly and gradually away from the PhCWG as indicated in Figure 4.5 by a distance adapted from Ref. [80]. The gradual shift of the holes by a few nano-metres creates a low-loss resonant mode confined by the mode gap of the PhCWG, based on the same principle as that used in a double

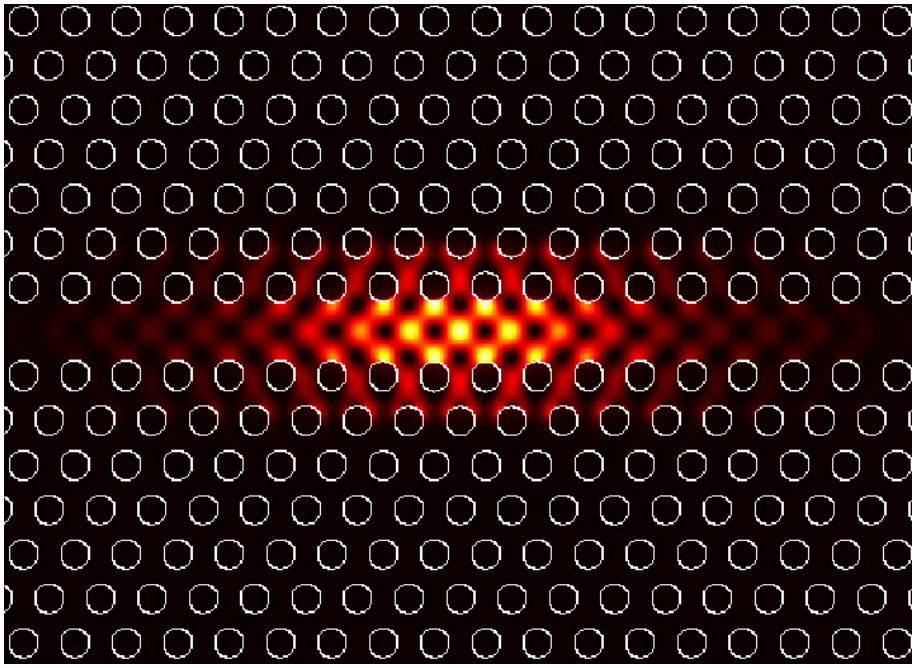

**Figure 4.6:** Calculated electric field energy distribution of the cavity mode.

heterostructure [79].

The device was fabricated by collaborators at the Hitachi Laboratory of Cambridge by first defining the PhC pattern lithographically in poly (methylmethacrylate) with a 100 kV VB6 Leica e-beam machine. The pattern was then transferred onto a 180-nm-thick GaAs slab containing InAs QDs using reactive ion etching (RIE) with a $SiCl_4$/Ar mixture; the remaining resist was removed with a $NH_4OH$ acetone soak before HF treatment formed an air-bridge. Finally, a digital etch step was employed using $O_2$/HCl to remove any damaged native oxide resulting from the RIE procedure [82]. A scanning electron microscope SEM image of the fabricated cavity is shown in Figure 4.4 and a view of the entire PhCWG structure with no apparent disorder is shown in Figure 4.5. The expected cavity mode profile, $Q$, and mode volume were obtained using a freely available three-dimensional finite difference time domain FDTD package MEEP as discussed in Chapter 2. A $Q$ of about $2 \times 10^7$ with $V \sim 1.3(\lambda_0/n)^3$ for $n = 3.46$ [83] was found using flux planes surrounding the PhCWG with the same size as the fabricated device. The electric field

energy distribution shown at the center of the cavity in Figure 4.6 confirms that.

### 4.2.3 PhCWGs characterisation

Photoluminescence PL measurements were carried out on a high InAs dot density ($\sim 100$ dots/$\mu m^2$) wafer with dots grown by molecular beam epitaxy giving broad emission centered at 1.35 eV. The sample was mounted in a He flow cryostat cooled to 5 K and the dots pumped with a $\sim$1 $\mu$m spot size from a $He - Ne$ laser, mounted using a 100$\times$ microscope objective (numerical aperture 0.75). The emission light was collected by the same objective, dispersed through a 0.55 m spectrometer and detected with a cooled charge coupled device camera. A typical PL spectrum obtained with this cavity is shown in Figure 4.7 under a pumping power of 32 $\mu$W. The spectrum consisted of an isolated sharp peak and a series of closely spaced peaks at slightly higher energies. These features were reproduced in all the PhCWGs investigated, with peak energies determined by the PhC lattice constant, hence indicating resonances associated with the band structure of the device. The cavity resonance shown by the arrow in Figure 4.7 was clearly identified by shifting the laser spot laterally along the PhCWG and through the cavity. This cavity mode with a $Q$ factor of 8000 is an ideal studying subject and we attribute the sharp peaks observed either side of the cavity to waveguide resonances whose origin is not fully understood at this stage and is the subject of further study.

Cavities with various hole sizes $r$, lattice constant $a$, and ratio $r/a$ were investigated. Devices emitting at higher energies show lower $Q$ as explained in the previous chapters. The $Q$s reported here are orders of magnitude lower than the ultra-high values shown elsewhere in Si and GaAs samples for this type of cavity [80]. However, it is worth pointing out that these ultra-high $Q$ have only been reported so far for cavities emitting at lower energies than in the present work and without a layer of QDs. We believe some of the losses in our samples are associated with the more significant bulk GaAs material

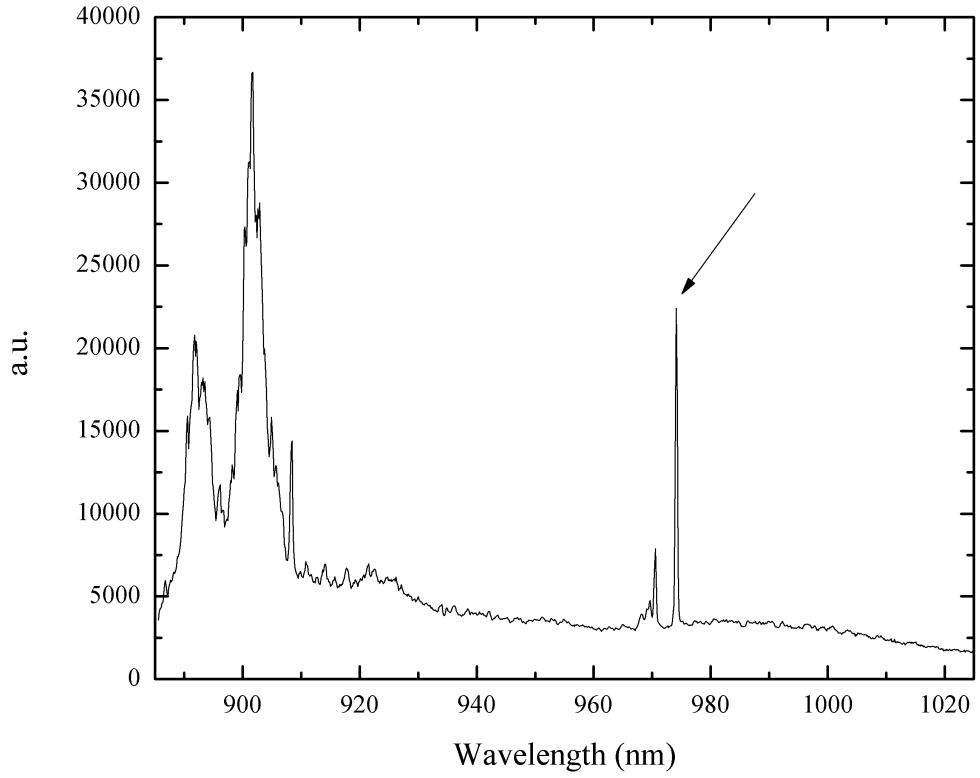


**Figure 4.7:** Photonic crystal waveguide with a high Q cavity.

absorption, electron or hole traps observed with higher energies [84], as well as absorption by the QD ensemble [85] whose PL is shown in Ref. [28].

Time-resolved PL measurement was carried out with the superconducting nanowire single photon detector. Figure 4.8 (a) shows the PL of the device composed of high density QDs and an L3 PhC peaking at 920nm wavelength. (b) is the life time of the central peak shown in (a). The measured decay time of 0.7 ns is shorter than that of typical bulk QDs in this sample of $\sim$ 1.2 ns, indicating the existence of a small Purcell Effect. Furthermore, it was shown in Ref. [86] that if the QD is not spatially coupled to the cavity mode, its lifetime will be inhibited by as much as an order of magnitude even if they are in spectral resonance. Thus experimental enhancement of spontaneous

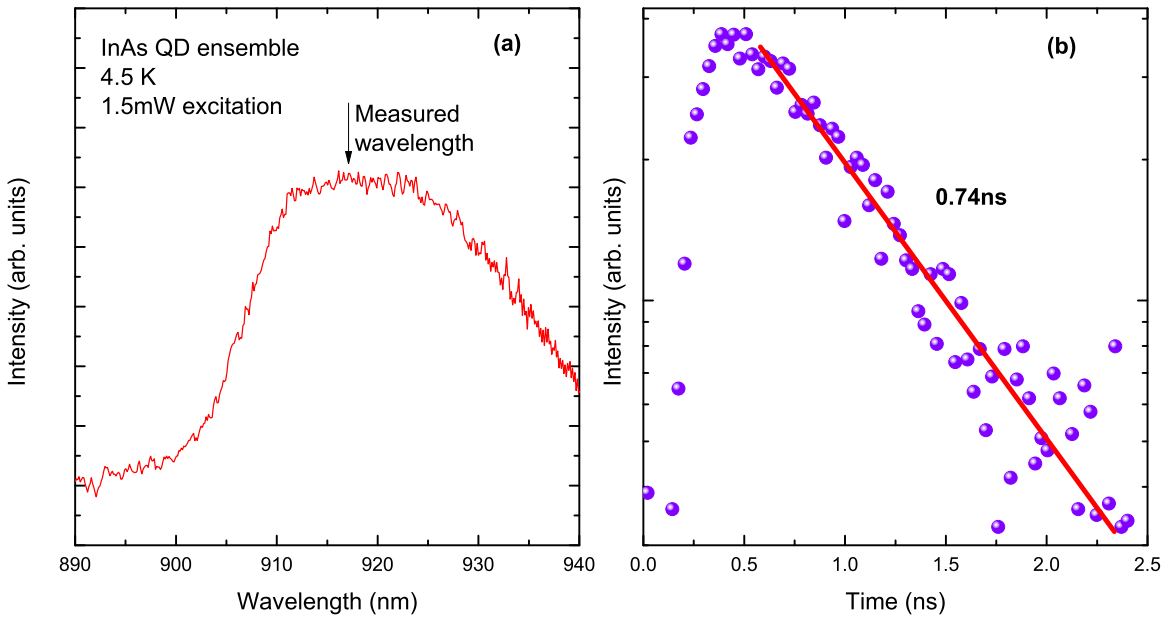


**Figure 4.8:** Lifetime of QDs inbeded in a L3 PhC measured by a SCSPD.

emission rate is not easy due to the double requirement of the QDs being both spectrally and spatially coupled to cavities.

## 4.3 Strong coupling

In quantum mechanics, electrons, atoms or photons can be in a range of states such as superpositions which differ from macroscopic-scale matters. This can be explained by decoherence theory inspired by the famous pseudo-experiment proposed by Albert Einstein et. al. [87]. This is more like a practical question since the coupling of elements with their environment decides the decoherence. This is also why a high Q-factor cavity along with vacuum and low temperature is required in our experiments. In this section, we are going to show the calculation first of the strong coupling boundary then follow with the experimental proof.

### 4.3.1 Looking for the boundary of strong coupling

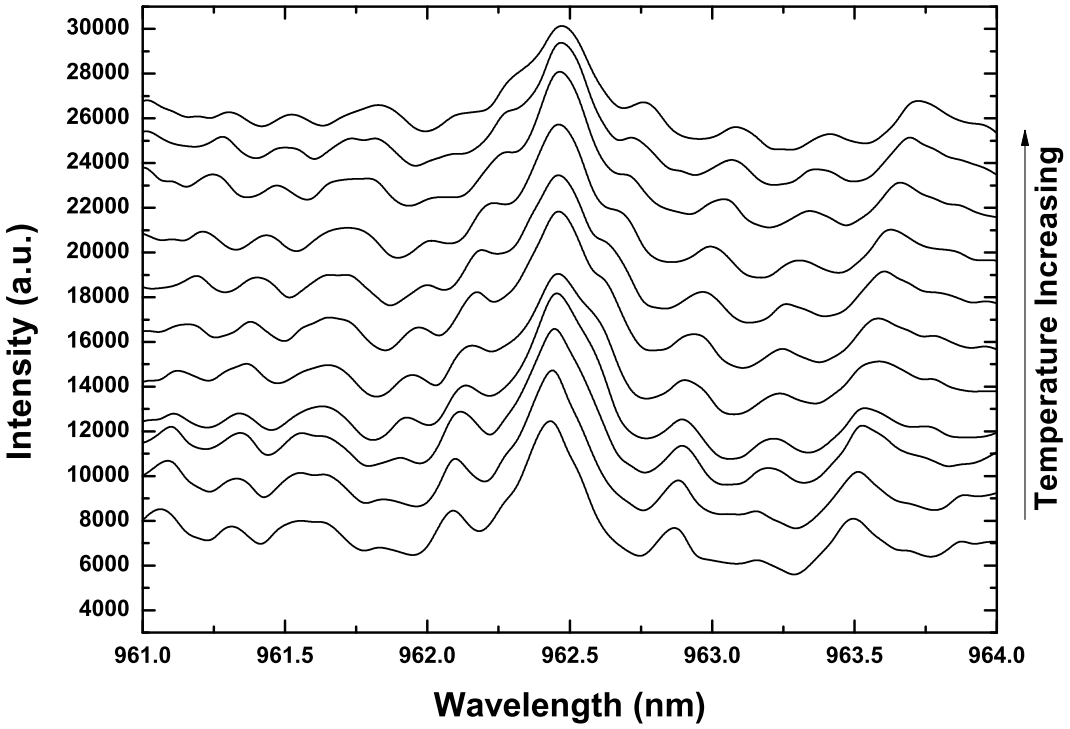


**Figure 4.9:** A QD's emission and cavity mode crossing each other without interaction.

Figure 4.9 shows the PL of a temperature detuned quantum dot crossing a cavity mode centered at 962.5 nm. There is no sign of any weak or strong coupling between the QD emission and the cavity mode. In the case of a single InAs QD coupled to a PhCWG nanocavity, the exciton transition can be modelled by a two-level system as described in Chapter 2 according to the Jaynes-Cummings model. The Hamiltonian can be written as:

$$H = \hbar\Omega_{exc}\hat{\sigma}_3 + \hbar\omega_\mu(\hat{a}_\mu^\dagger\hat{a}_\mu + \frac{1}{2}) + ig\hbar(\hat{\sigma}_-\hat{a}_\mu^\dagger - \hat{\sigma}_+\hat{a}_\mu) \tag{4.3}$$

where $\Omega_{exc}$ is the fundamental exciton frequency, $\hat{\sigma}_+$, $\hat{\sigma}_-$, $\hat{\sigma}_3$ are pseudo-spin operators

for population oscillations between two atomic levels $g$ and $e$, and $\hat{a}_\mu^\dagger$, $\hat{a}_\mu$ are creation and annihilation operators for the cavity mode.

This Hamiltonian has a Rabi splitting that occurs at a single angular frequency $2g\sqrt{\bar{n}+1}$, associated with the coupling constant from Equation 4.2 and the mean photon number $\bar{n}$ (classical limit). When the coherent field is weak, the quantum behavior of the Rabi oscillation can be simplified to $2g$, corresponding to the ground state and the first excited doublet [88]. Combining equations 4.1 and 4.2 we have:

$$g = \sqrt{\frac{1}{4\pi\epsilon_0\epsilon_r}\frac{\pi e^2 f}{mV}} \tag{4.4}$$

where $\epsilon_0(\epsilon_r)$ is the vacuum (relative) permitivity and the oscillator strength $f = 2m\omega_0 d^2/(e^2\hbar)$, where $m$ is the free electron mass. The spontaneous emission spectrum can be then calculated following a master-equation approach with both the QD exciton ($\mathbf{\Gamma_{exc}}$) and the cavity mode $\mu$. The complex energy splitting then can be expressed as:

$$\hbar\Omega = \hbar\Omega_{exc} \pm \sqrt{\hbar^2 g^2 - \left(\frac{\Gamma_{exc} - (\hbar\omega_\mu/\mathrm{Q})}{4}\right)^2} - \mathrm{i}\left(\frac{\Gamma_{exc} + (\hbar\omega_\mu/\mathrm{Q})}{4}\right) \tag{4.5}$$

The solutions of Eq. 4.5 are plotted in Figure 4.10 as a function of $Q$. Assuming the InAs QD is spatially and spectrally resonant with the ground cavity mode at energy $\hbar\omega_\mu$~1.315 eV. The PhCWG mode volume was calculated using the FDTD method as $1.3(\lambda/n)^3$ at 5K which gives $V$ ~$2.7\times10^{-14}$cm$^3$ and an oscillator strength $f = 10.7$ for typical self-assembled InAs QDs [89]. The oscillator strength $f = 10.7$ is a typical value for self-assembled InAs QDs as measured in Ref. [90]. The boundary line for our experiment is predicted to appear at $Q$ ~3000 and to saturateby $Q$ ~10000.

Figure 4.11 is an attempt to study the strong coupling boundary. A 4000 $Q$ PhCWG with high density QDs was studied. One can almost see that a Rabi splitting was starting to appear. This demonstrates that our model is in good agreement with experimental observation. Nevertheless, a more complete model is necessary which includes the bi-excitons and many-body interactions [91] [92].

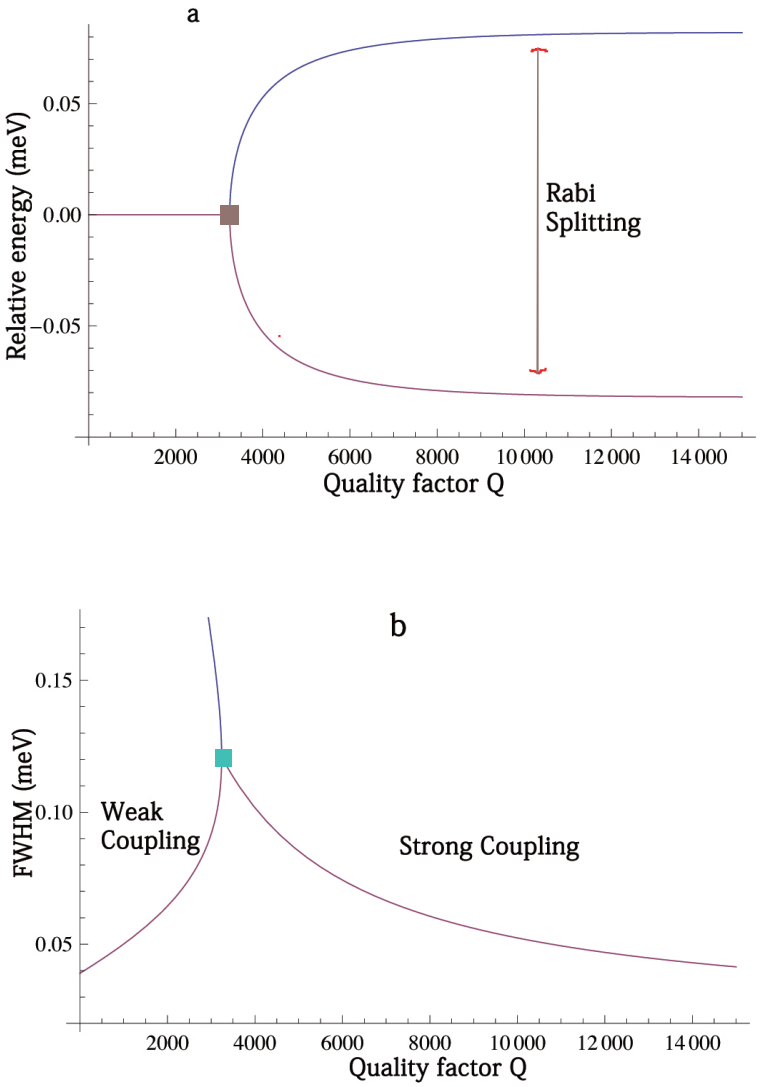


**Figure 4.10:** (a) Real and (b) imaginary parts of Eq. 4.5 as a function of $Q$. The condition for strong coupling $2g \geq [\kappa + \gamma]/2$ is the square point in both (a) and (b) with the $Q$ value $\sim 3400$.

### 4.3.2 Identifing promising samples

The whole QD-cavity experiment that we performed was a complicated process which needed many researchers working together. The samples were grown at Imperial College and Sheffield University. I then characterized the bare samples in micro-PL before

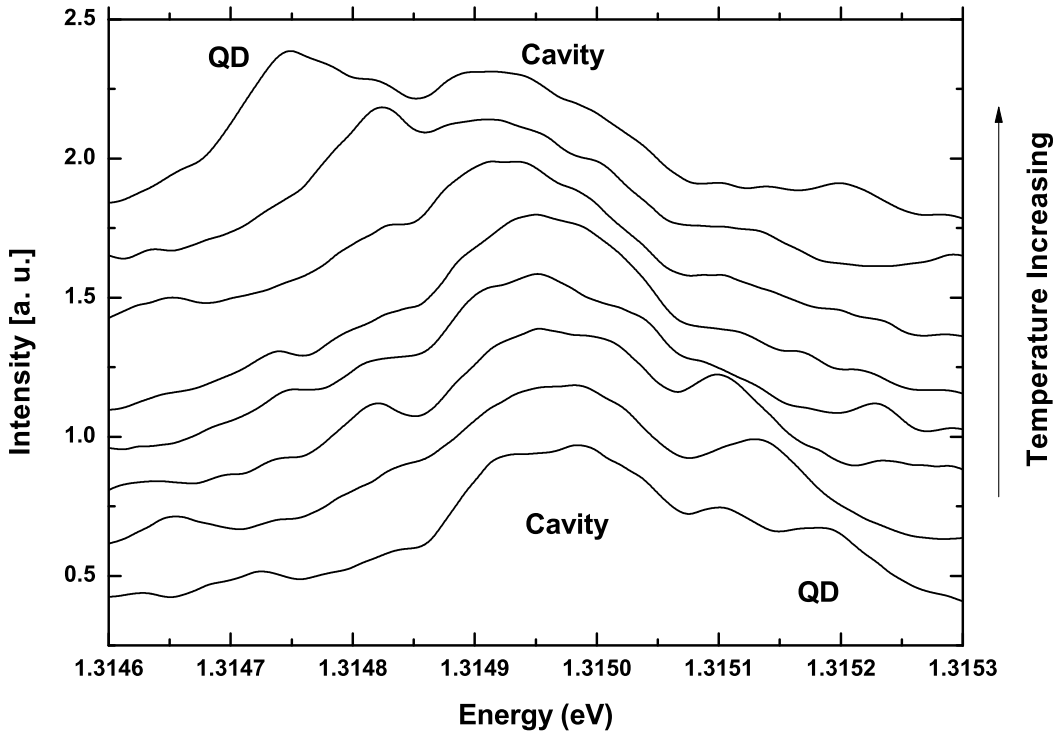


**Figure 4.11:** Strong coupling discovered at an extreme condition.

they were sent to Cambridge for processing. The QD Samples were next patterned and returned to Oxford. I spatially registered the position of QDs as described in the last chapter and then sent them back to collaborators in Cambridge for PhC fabrication. At the end, the PhC devices were sent to me to finalize the study of strong coupling etc.

This back and forth shuttling produced a requirement for identifying promising samples early in the process. Firstly, the PL characterization was very important for all the following steps. The decisive factors were the QD density and PL performance. For example (Figure 4.12), a typical dot's spectrum saturates with increasing excitation power. Uniform fitting as shown in red line is essential for a well isolated quantum dot. Secondly, looking for strong coupling was always challenging. The temperature detuned resonant QD and cavity spectra had to fulfill many conditions including finite linewidths

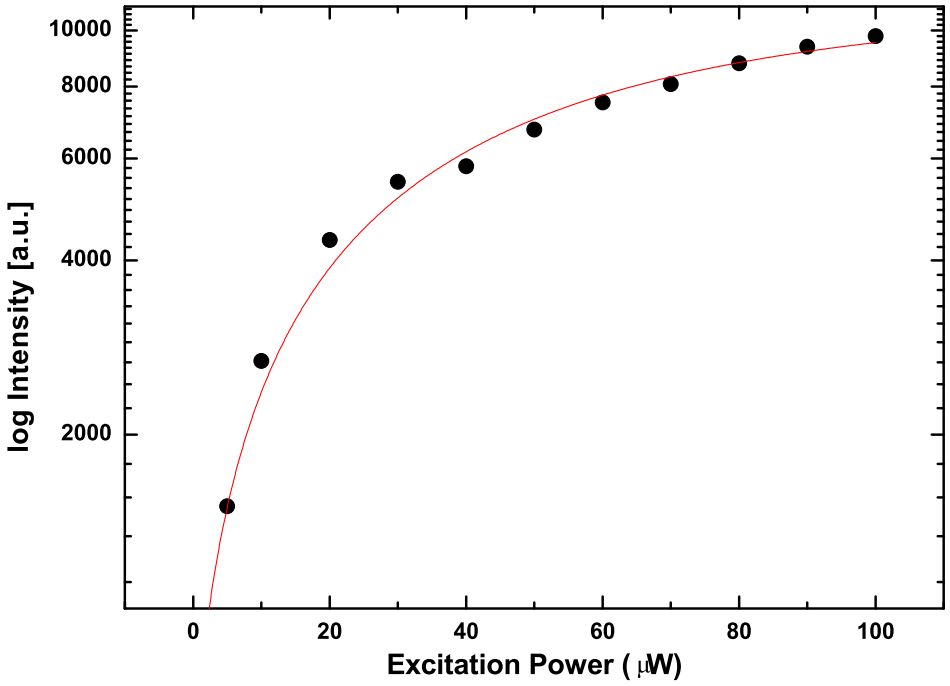


**Figure 4.12:** The power dependence of a cavity with QDs inside.

and accurate resolution limited focusing.

### 4.3.3 Strong coupled quantum dots in a photonic waveguide

A clear strong coupling regime was observed with a reduced pump power of 3.2 $\mu$W and a QD slightly to the blue of the cavity mode. The QD is strongly redshifted toward the cavity as the temperature increases due to band gap shrinkage as observed in Figure 4.13.

In an uncoupled system, both the QD and cavity photon would merge into a single peak without perturbation in their respective quantum states as showed in Figure 4.9. In Figure 4.13, by increasing temperature from 19K to 29K, a obvious strong coupling phenomenon was observed. Two Lorentzians were fitted to the dressed state spectrum

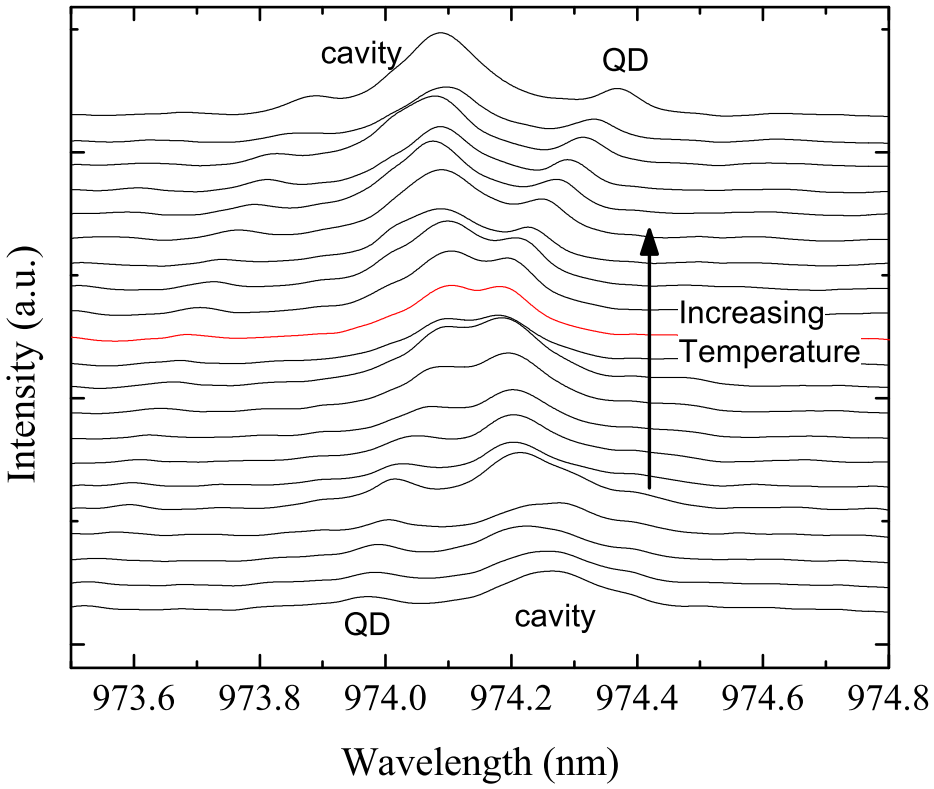


**Figure 4.13:** PL spectra of the strongly coupled QD-cavity mode system for various temperatures in steps of 0.5 K showing the anticrossing as the dot is tuned toward the cavity mode. Two distinct peaks of similar line widths at resonance can be seen as red spectra.

and the plotted linewidths are shown in Figure 4.14. The emission intensity of the quantum dot exciton at initial detuning is smaller by about one order of magnitude than that of the cavity mode. The FWHM of the cavity mode (190 meV for low-excitation conditions) is about 3-times larger than that of the quantum dot. Despite increasing the temperature (up to 29 K) the emission spectrum constantly consists of two distinct features. However, at 29 K the components of the emission exchange their energy states: the QD exciton emission movesto the low-energy side with similar FWHM to that seen

at 19K at higher energy. Both the emission components reached similar line width and intensity at about 24 K and the cavity mode emission finally moved to the lower-energy side.

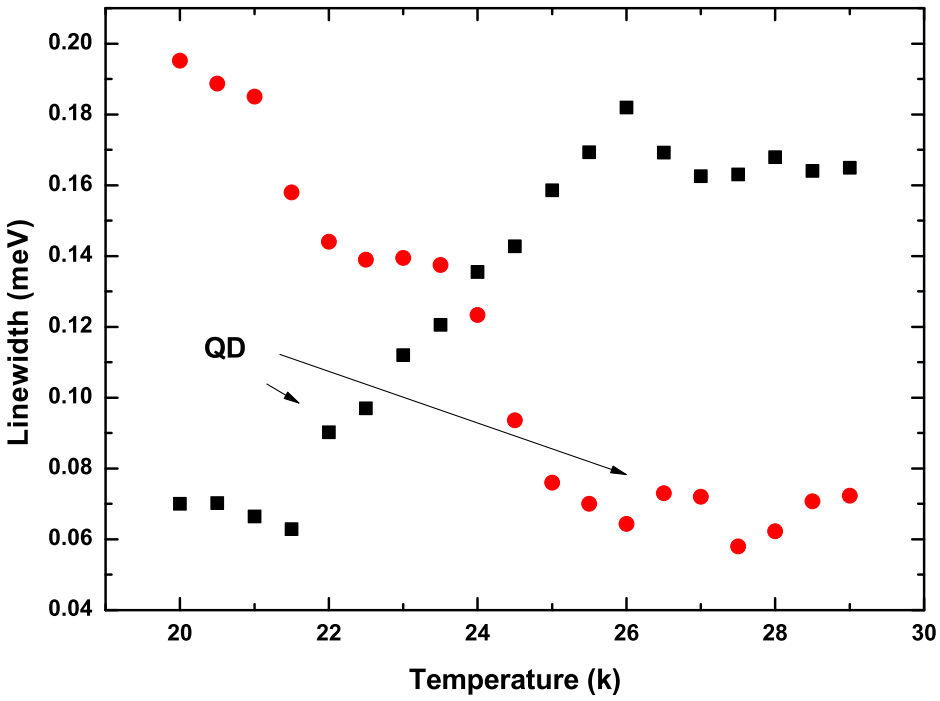


**Figure 4.14:** Linewidth plotted as a function of temperature from Figure 4.13. The linewidth of both QD and cavity is tuned to the same level as the strong coupling is occurring.

The energy spectrum of the two contributions to the spectrum avoid crossing and showing degeneracy over the entire temperature detuning process. This manifests itself experimentally as two distinct Lorentzian peaks are a clear indication of an anti-crossing of the single QD exciton and the cavity-mode due to strong coupling. Note that the cavity peak should redshift slightly as the temperature increases due to the increased bulk refractive index of GaAs. The blueshift observed here can be understood by considering

removal of material on the surface of the sample during the heating process. We believe this material consists of condensed gas on the cold sample surface [93].

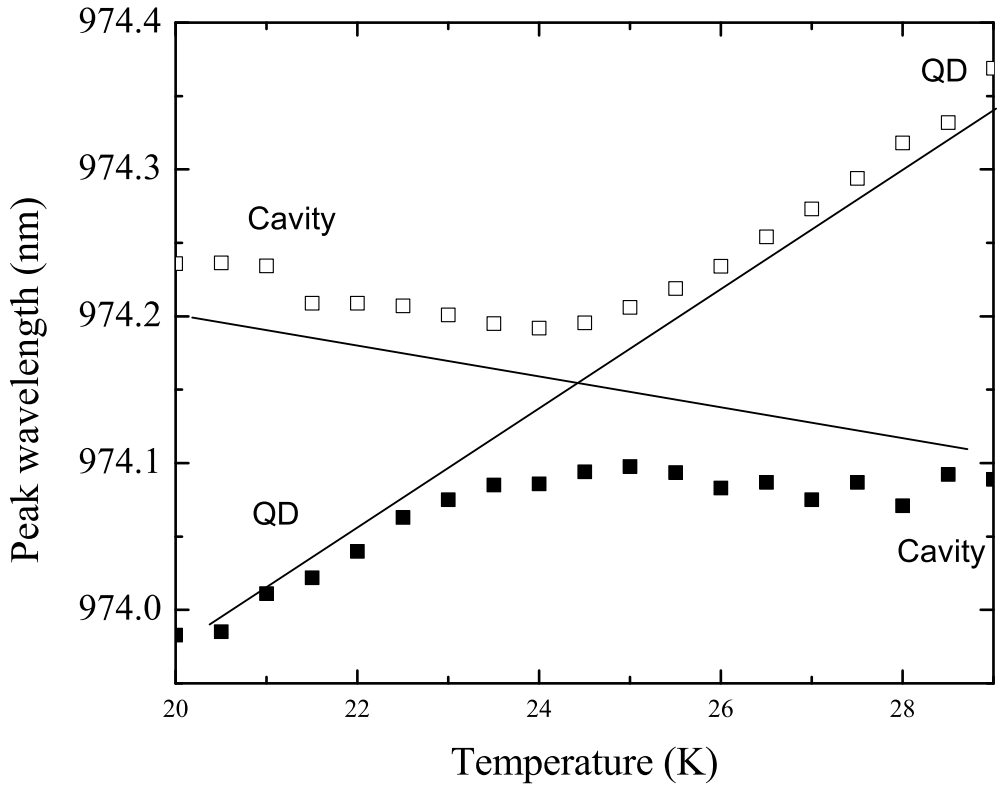


**Figure 4.15:** Peak positions of the strongly coupled and uncoupled system for various detunings, showing a Rabi splitting of about 140 $\mu$eV at zero detuning. The squares indicate the measured peaks from the strongly coupled system while the solid lines are obtained from an uncoupled dot and cavity measured on the same sample, respectively. The black lines show the calculated peak positions for a strongly coupled system for a particular detuning energy.

A Rabi splitting energy $E$ of about 140 $\mu$eV is deduced from the peak positions of the dot and PhCWG cavity mode at resonance (zero detuning) as shown in Figure 4.15.

Rabi splitting occurs at resonance when the excito-photon coupling strength becomes greater than the mean of their decay rates so that the energy can be exchanged reversibly between the QD and the cavity mode. We measure the cavity line width $\gamma_c = 160\mu$eV from the full-width at half-maximum of our cavity peak at 5 K, and $\Gamma_{exc} = 78\mu$eV for the single QD. The latter linewidth corresponds to the resolution limit of our spectrometer. A coupling constant $g$ of $82\mu$eV was deduced from the fitted dot and cavity energy of the strongly coupled system shown in Figure 4.15. We usually have $\gamma_c \gg \Gamma_{exc}$, so the condition to satisfy the strong coupling from the real part of Eq.4.5 simplifies to $g > \gamma_c/4$, which is clearly the case in our results.

Figure 4.16 is a final zoomed-in view of the QD-cavity coupling system at three different temperatures. The Rabi splitting measured in this work is about 70 percent of the $200\mu$eV predicted for $Q = 8000$. It is clear from previous reported results that the main obstacle in achieving the maximum splitting is the misalignment between the QD and the antinode of the cavity mode, which causes the coupling strength to decrease [3]. PhC cavities with smaller $V$ than the PhCWG cavity have the potential to achieve larger Rabi splitting but at the expense of more stringent alignment requirements. The present system would benefit greatly from deterministic procedures to locate the position and energy of the QD for the study of coupled high $Q$ PhC resonators for quantum electrodynamics applications [58] [94].

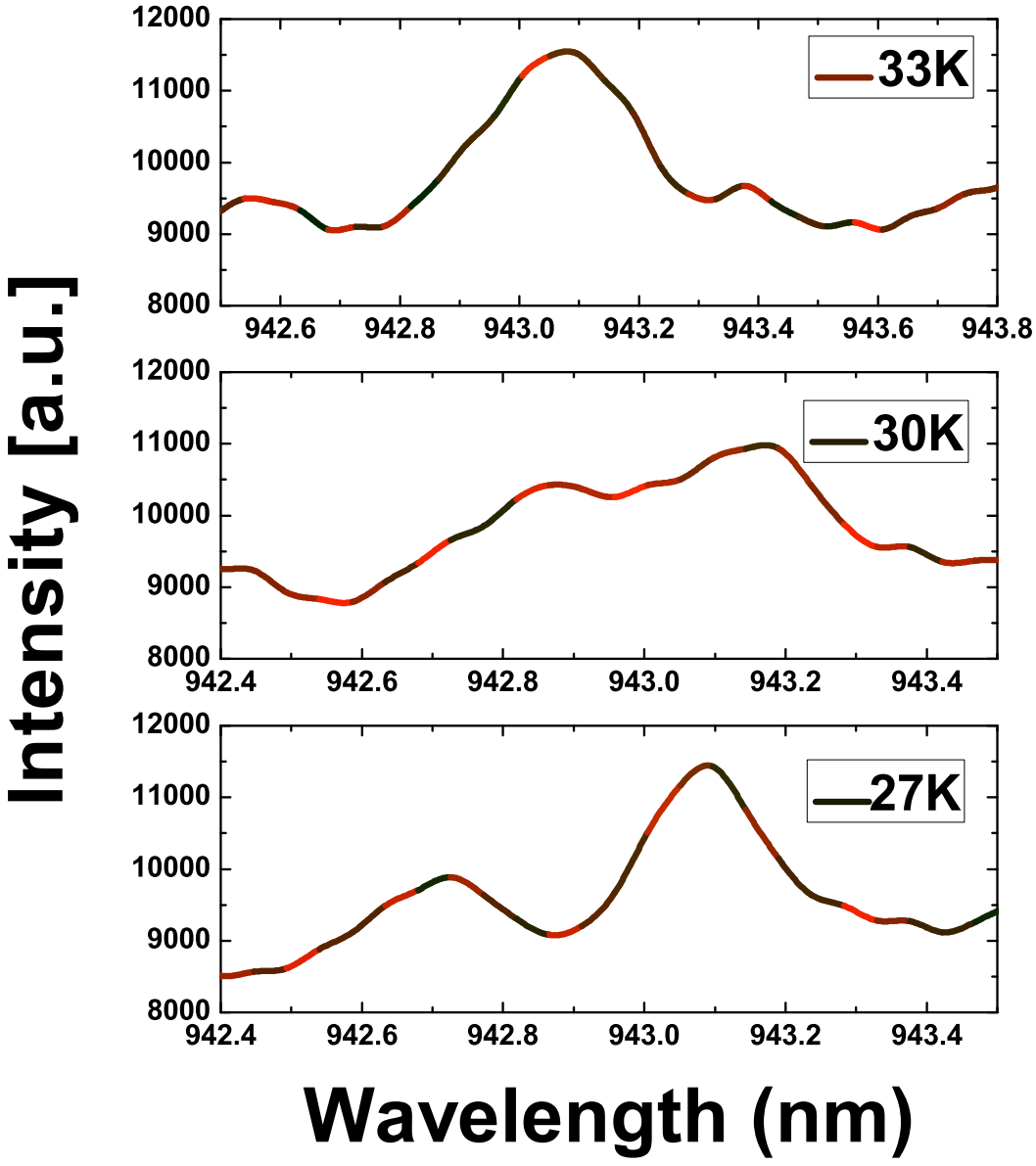


**Figure 4.16:** Three different temperature spectra showing the tuning of strong coupling.

# Chapter 5

# Single-walled carbon nanotubes

## 5.1 Carbon materials, an introduction

Carbon is essential in our daily life and can be found everywhere around us. Carbon exists as crystalline states in natural compounds like diamond or graphite, or in a molecular state such as oil or hydrocarbon gases [95]. Nowadays it is synthesised into many different kinds of materials. The physical and electrical properties of these carbon materials differ strongly due to their allotropic structure. For instance diamond is the hardest natural material, but graphite is rather soft and conductive. Carbon is in group 4 of the periodic table of elements and four valence electrons can be found in the ground state in the second shell: $C(1s^2 2s^2 2p_x^1 2p_y^1)$.

In 1985, Harold Kroto, Richard Smalley and Robert Curl discovered a completely new carbon structure with 60 carbon atoms [38], which earned them the Nobel Prize in 1996. These carbon molecules along with other similar materials are now referred as fullerenes after Buckminster Fuller. A so called "bucky ball" is composed with 60 carbon atoms aligning in a icosahedral symmetry to resemble the structure of a football. In 1991, Sumio Iijima discovered long cylindrical tubes with diameters on the nano-scale when he was studying fullerenes on a graphite electrode [96] and this spawned research on

carbon nanotubes. He continued his work and found carbon nanotube production would be enhanced if cobalt or iron were added to the electrodes, which led to the discovery of single-walled carbon nanotubes (CNT) [97]. CNTs express phenomenal physical and chemical properties such as ballistic charge transport, strong mechanical strength and elasticity along with striking optical properties [98].

New carbon materials are continuously being discovered or fabricated. Graphene for example, a single sheet of carbon atoms densely packed in a honeycomb crystal lattice, has attracted great deal of interest [99]. The discovery of the astonishing properties of graphene such as extremely strong mechanical strength and super high conductivity won Geim and Novoselov the Nobel Prize in Physics for 2010. The focus of this chapter is on CNTs inspired by their ability to emit light quanta as explained in ref. [4]. The term CNT in this thesis is used to mean a single-walled carbon nanotube, rather than a double or multi-walled carbon nanotube.

## 5.2 The synthesis of CNTs

Semiconducting CNTs are one-dimensional direct band-gap materials and consequently promising candidates for optical studies. The distinct structural and optical properties of CNTs arise [100] from the wrapping angles (chirality) of the graphene sheets and the diameters of the CNTs produced. This phenomenal optical behavior originates from the band structure of a graphene sheet where the $\pi^*$ bonds touching $K$ and $K^{'}$ points in the fist Brillouin zone. When the graphene sheet is wrapped up into a tube the band structure is modified producing one dimensional entities. Depending on the exact nature of the wrapping, the nanotubes can be metallic or semiconducting in nature. The parameter which controls this is known as the wrapping vector $\mathbf{w} = n\mathbf{a}_1 + m\mathbf{a}_2$, where $\mathbf{a}_1$ and $\mathbf{a}_2$ are the hexagonal lattice vectors. The PL is determined by many factors including the tube diameter, chiral angle (n,m) and surrounding environment [101]. If $n - m$ is

divisible by 3 then the tubes are conducting. In this thesis, we focus only on tubes which are semiconducting at room temperature. For completeness, the three families of CNTs are $n - m$ =constant, $2n + m$ =constant and $n + 2m$ =constant. The $2n + m$ family defines tubes with similar diameters but different chiral angles and the $n - m$ family defines tubes with same chiral angles but different diameters. We can also classify semiconducting tubes into 2 categories *Type1* and *Type2*, by $\mod[(n-m), 3] = 1, 2$, respectively, defined by $(E_{22}/E_{11})$, the different directions of the CNTs transition energy ratios deviation from a central value [102]. Defects in CNTs also have a strong effect on the properties of the tubes. In our experiments, we studied various polymer surrounded CNT samples to enhance the PL. These were produced both by the CoMoCat and HiPCO processes (described below) and they were dispersed in the solvent toluene. All of the samples are aqueously suspended in the polymer and have strong selectivity of chiral angles [49].

### 5.2.1 CNT growth

There are several ways to grow CNTs yielding different diameter and chirality distributions and purities, including Pulsed-laser Vaporization (PLV) of graphite [103], the Carbon Arc (CA) Discharge [104], Thermal or Plasma-assisted Chemical Vapour Deposition (CVD) [105]. The CVD method has been divided into two processes to attain high purity and small diameter tubes. High-pressure Carbon Monoxide Decomposition (HiPCO) [106] techniques produce single-walled carbon nanotubes from gas-phase reactions of iron carbonyl in carbon monoxide at high pressures (10-100 atm). On the other hand, the Co-Mo Catalyst (CoMoCat) [107] technique can produce smaller and narrower diameter nanotube distributions using cobalt and molybdenum as catalysts from CO gas. In general, the raw CNT always contains amorphous carbon and metallic impurities so it is necessary to purify the raw CNT materials. Another issue is that as-grown CNTs

end to clump together in bundles and often intertwine with each other. This makes measuring the properties of one CNT very difficult. One way to overcome this is to coat the CNT in a polymer.

### 5.2.2 Conjugated polymers

Polymeric molecules in general are made by bonding large weight molecules covalently to their nearest neighbors. The linked units of small molecules are called monomers. In contrast to the $\sigma$-bonds in saturated $sp^3$ hybridized polymers, $\pi$-conjugated polymers are repeated structures of $sp^2$ hybridized carbon atoms. All four valence electrons in the $\sigma$-bonds are stationary (saturated) and thus have zero conductivity while in $\pi$-bonds the polymer chain results in a high charge carrier mobility. CNTs have controllable solubility in polymer solution [49]. Figure 5.1 shows the chemical structures of a poly[9,9-dioctylfluoren] (PFO). The side chains assist the self-assembly of the octyl lateral tails which interconnect the polymer chains like a zipper. The polymer selectively wraps nanotubes and thus de-bundles the un-processed CNTs. Two other polymers were used in this work, first being poly(3-hexylthiophene) (P3HT) and the second (F8BT).

As one dimensional chain structures, the optical properties of conjugated polymers can be generalized in a similar fashion to those of CNTs', which were introduced in

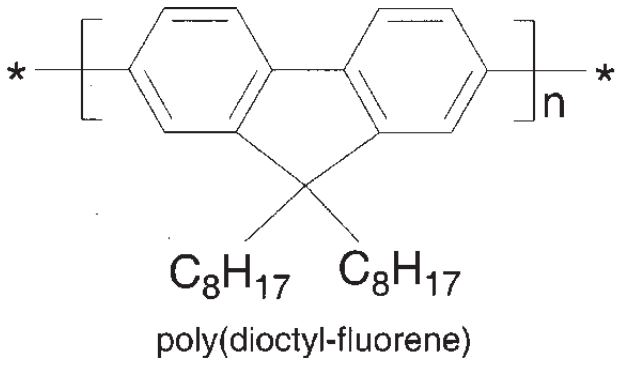


**Figure 5.1:** Chemical structures of PFO.

Chapter 1. Electrons are excited from the valance band when photons are absorbed to form excitons. The momentum and spin of these transitions obey the selection rules and they are often cited as HOMO-LUMO transitions where the electron is lifted from the highest occupied molecular orbital (HOMO) to the lowest unoccupied molecular orbital (LUMO). The exciton will then relax through the emission of phonons and decay through emission of a photon or non-radiatively [108]. All the above properties assured us of the selection of conjugated polymer as a surfactants for CNTs. Despite this, some devices based on CNT blends with conjugated polymers have shown poor performance in recent studies [109] [110]. However, the theoretical studies from Kanai [111] and experimental studies from Stranks [112] demonstrated that charge separation, and hence the energy transfer from the polymer to the CNTs, is only efficient when small diameter semiconducting CNTs are individually embedded.

### 5.2.3 Dispersion of CNTs in conjugated polymers

The HiPCO CNTs were bought from Nanotechnologies Incorporated (CNI), while the CoMoCat material was purchased from SouthWest NanoTechnologies (SWeNT). The synthesis and analyses of the CNTs samples were similar to the ones described in ref. [49]. Firstly, $5-10$ mg of the various polymers were added to $10-20$ ml of an organic solvent (toluene, or chlorobenzene). To completely solubilize the polymer, this mixture was treated in a sonic bath for about 60 mins. Next, the powdered CNTs were added to the mixture at an appropriate amount, which is normally around $5-10$ mg. The material was subsequently treated in a high power ultrasonic disintegrator at a frequency of 23 kHz with a 10 micron amplitude for 15 mins. The disintegration breaks the CNT bundles into raw CNTs and therefore allows an interaction between individual CNTs with the dissolved polymer chains in the dispersion. Some polymers were found to be able to fully wrap around a CNT as shown in Figure 5.2 and the rebundling rate was found to be low.

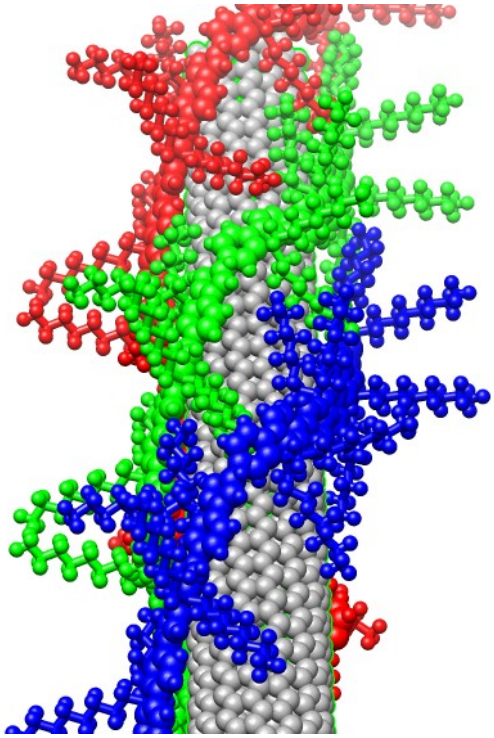

**Figure 5.2:** Schematic diagram of a (8,6) CNT coated with a monolayer of sheath PFO. PFO chains are colored blue red and green.

All polymers and CNT raw materials were used without further purification or processed in air.

To remove the remaining bundles from the dispersion, the freshly ultrasonicated solution was placed in a centrifuge, which separates the particles by their density. The density of the CNT-bundles was calculated to 1.2 $gcm^{-3}$ [113], while the single CNTs in the aqueous dispersion were estimated to have a density of 1.0 $gcm^{-3}$. Thus if the solvent has an appropriate low density between $1.0 - 1.2$ $gcm^{-3}$, then any remaining unreacted bundles could be removed. In a selective dispersion, the selection of solute is very important since certain CNT species are preferentially dissolved. This is also the reason we chose toluene or chlorobenzene since the geometry of solutions effects how the polymer wraps the CNT and results in differing densities [114].

## 5.3 Characterization, a study case of single photon material

Since O'Connell et al. successfully separated individual carbon nanotubes [113], PL studies of CNTs have boosted the entire field. A quite thorough understanding of their linear optical properties such as diameter and chirality dependent optical excitation and phonon assisted relaxation have been made. Recently, quantum correlations in PL were also reported from a single CNT [4]. Therefor, a complete study of the single tube stage is necessary and will be detailed in the following sections.

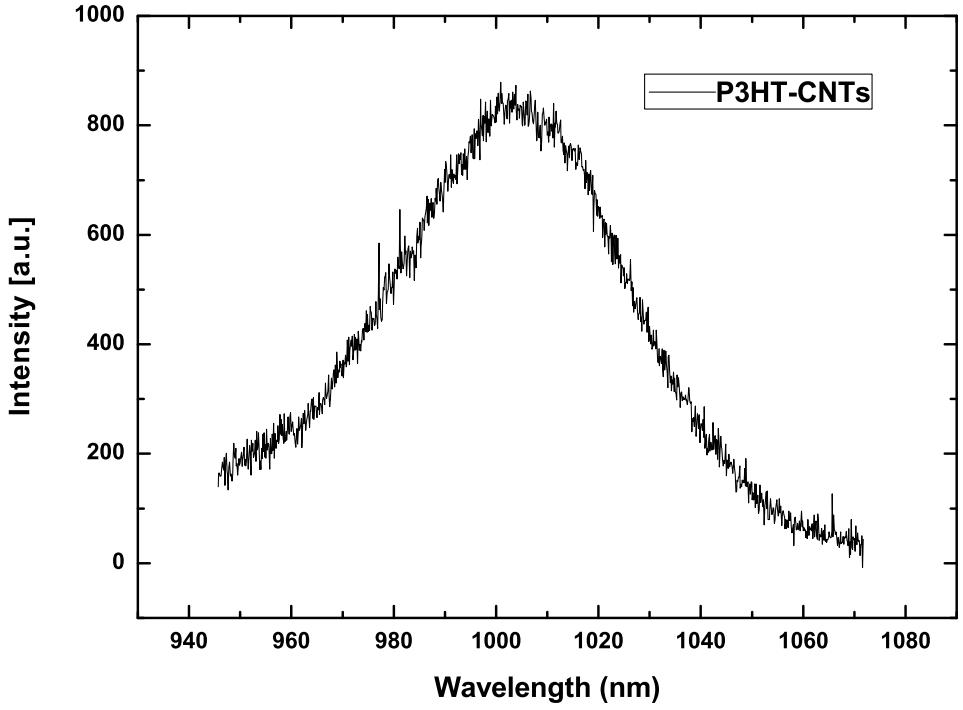


**Figure 5.3:** PL Emission from P3HT-CNTs bundle showing spectra red-shift.

### 5.3.1 Carbon nanotubes bundles

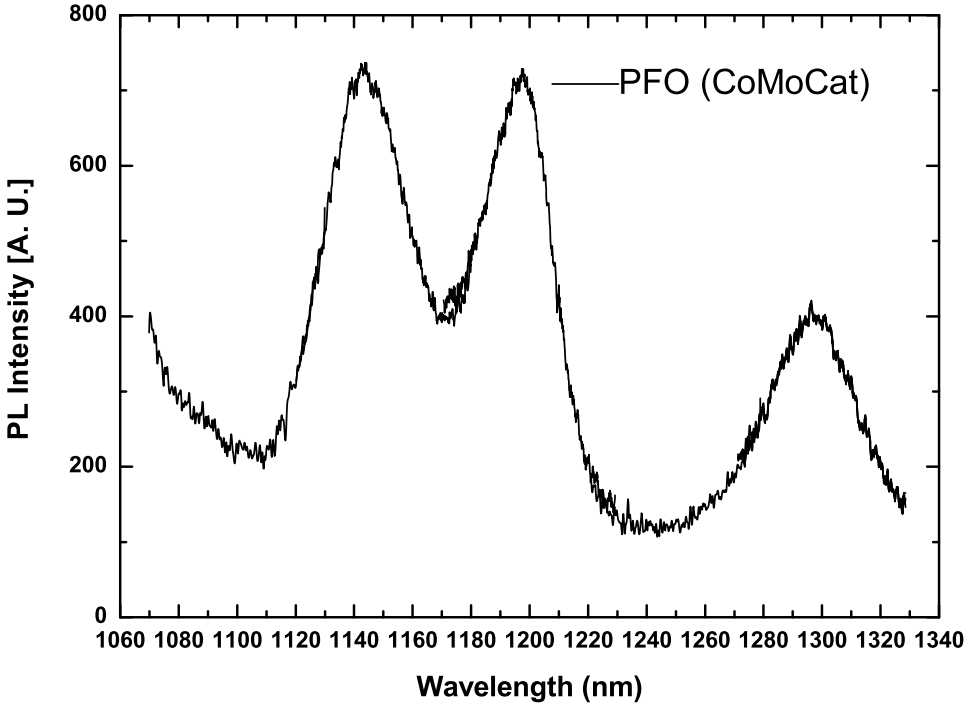


**Figure 5.4:** PL from CoMoCat nanotubes, excited with 632nm laser.

After sample preparations introduced in the previous section, we dispersed both HiPCO and CoMoCat CNTs with P3HT, F8BT or PFO polymers on quartz wafers. Figure 5.3 shows the PL emission under resonant CW laser excitation of P3HT coated CoMoCat CNTs. Individual CNTs are wrapped and separated as explained in the previous section, which results in bright PL emission. An multi-photon broadening of $\sim$20 meV FWHM indicates photoluminescence arising from nanotube bundles. $(6, 5)$ tubes are responsible for the peak around 1005 nm. A red shift for these P3HT bundles is found compared to that from F8BT bundles (993nm) and this has been recognised as a solvatochromic shift, in which the local environment of various dielectric media experiences a change in the absorbed molecules dipole moment and leads to a rearrangement

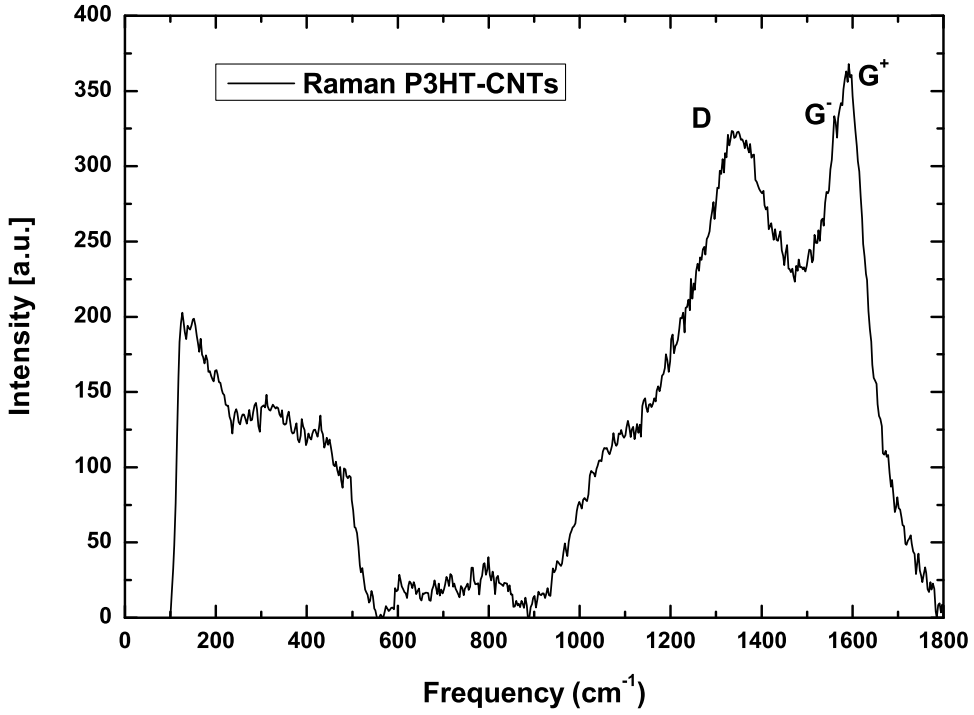


**Figure 5.5:** Raman spectroscopy of P3HT-CNTs bundle.

of the reaction field between the molecules in the excited and ground states [115]. Figure 5.4 shows a CoMoCat CNT-bundle in PFO polymer solution. Clearly, selectivity of polymers to the diameters of CNTs has shown from the PL centered at ∼1200 nm(8,6) tube. (7,6)( ∼1140 nm) and (8,7) (∼1290 nm) can also be seen. These CNT PLs arise from different tube geometry with respect to their environment.

Raman spectroscopy was carried out to study the phonon relaxation of the CNTs. Figure 5.5 shows a typical spectrum of our Raman modes using a JY Horiba Labram Aramis imaging confocal Raman microscope with 532 nm excitation. The *D*-band and *G*-band features for CNTs are clearly shown (without radial breathing modes due to the limit of the experimental system). The $D - band$ mode peaked at 1350 $cm^{-1}$ originates from one-phonon second-order Raman scattering processes. One of the *G*-band

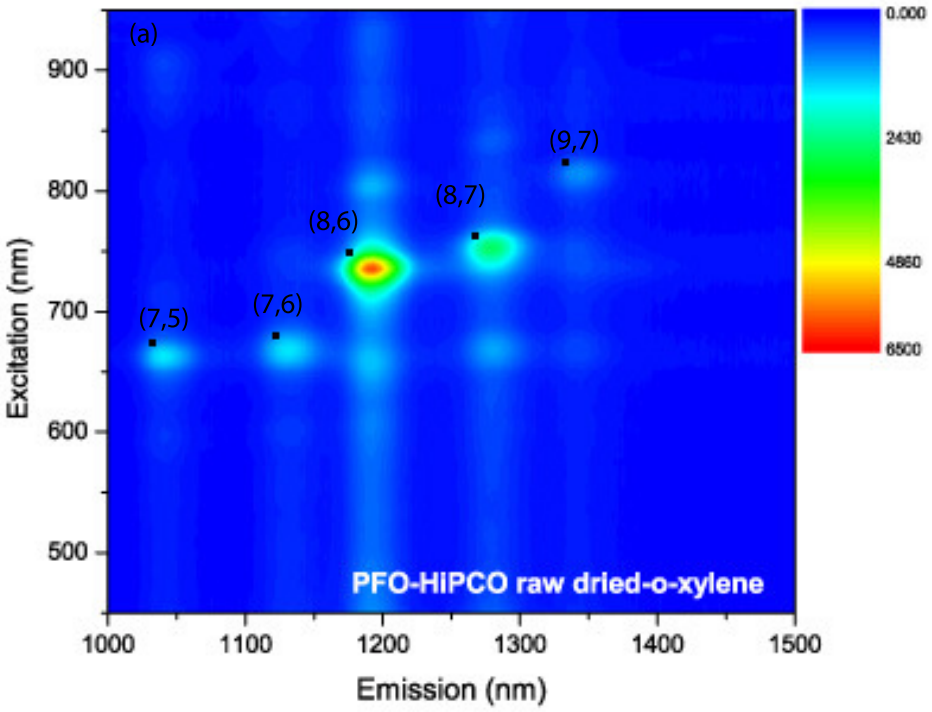


**Figure 5.6:** Photoluminescence excitation maps of the purified PFO-HiPCO compounds made in Xylene and redispersed in chloroform. The CNT positions are indicated by black spots for the bundle species. The PL of free PFO is clearly removed and only the energy transfer induced emission is found to correlate with the absorption of the PFO film.

modes peaks at 1592 cm$^{-1}$ ($G^+$) and the other at about 1560 $cm^{-1}$ ($G^-$). The $G^+$ mode arises from carbon atom vibrations along the nanotube axis (LO phonon mode) and has a frequency that is dependent upon the charge transfer from dopant additions to the CNTs (in this case the polymer). The $G^-$ mode arises from carbon atom vibrations along the circumferential direction of the CNTs (TO phonon) and has a lineshape dictated by wether the CNTs are metallic (Breit-Wigner-Fano lineshape) or semiconducting (Lorentzian lineshape) [116].

There are several proposed decay schemes for CNTs, among which is the strong exciton binding energy dominated radiative decay lifetime, which has been calculated to be 1-10 ns [117], much longer than any experimental results 1-100 ps [118] [119]. This indicates the existence of non-radiative channels inside the CNTs. Structural defects, impurities and other heterogeneities can greatly change the optical properties of CNTs via localization of excitons [120]. "Dark" exciton states have been proposed to have limited contribution to non-radiative decay [121], as do phonon-assisted indirect exciton ionization processes, which involve Coulomb and exciton-phonon interactions. Multi phonon decay lifetimes of localized excitons have been shown to be 2-3 orders of magnitude shorter than that those for free excitons, and this can explain the measured lifetimes [122]. All of the above decay schemes have contributions from single CNTs as single photon sources [4].

Photoluminescence excitation map (PLE) is a very efficient technique to study the energy transitions with in CNTs. Figure 5.6 shows one of the purified PFO-HiPCO CNTs PLE maps recording every emission PL corresponding to each excitation wavelength. The features seen denote emissions from tubes with different chiralities and charge transfer from polymer to tubes. Specific peaks are denoted by black spots and their chirality assignments. The map shows a good selectivity of PFO and proves the removal of any free polymer. The crossing lines arise from energy transfer from stacked CNTs with help from the polymer [114].

### 5.3.2 How to find single CNTs

The photon luminescence quantum yield of CNTs can be defined according to:

$$\Phi = \kappa_r/(\kappa_r + \kappa_{nr}) \tag{5.1}$$

in which $\kappa_r$ and $\kappa_n r$ denote the radiative lifetime and non-radiative decay rate, respectively. $\Phi$ is usually $\sim 10^{-3} - 10^{-4}$, indicating the dominance of non-radiative relaxation

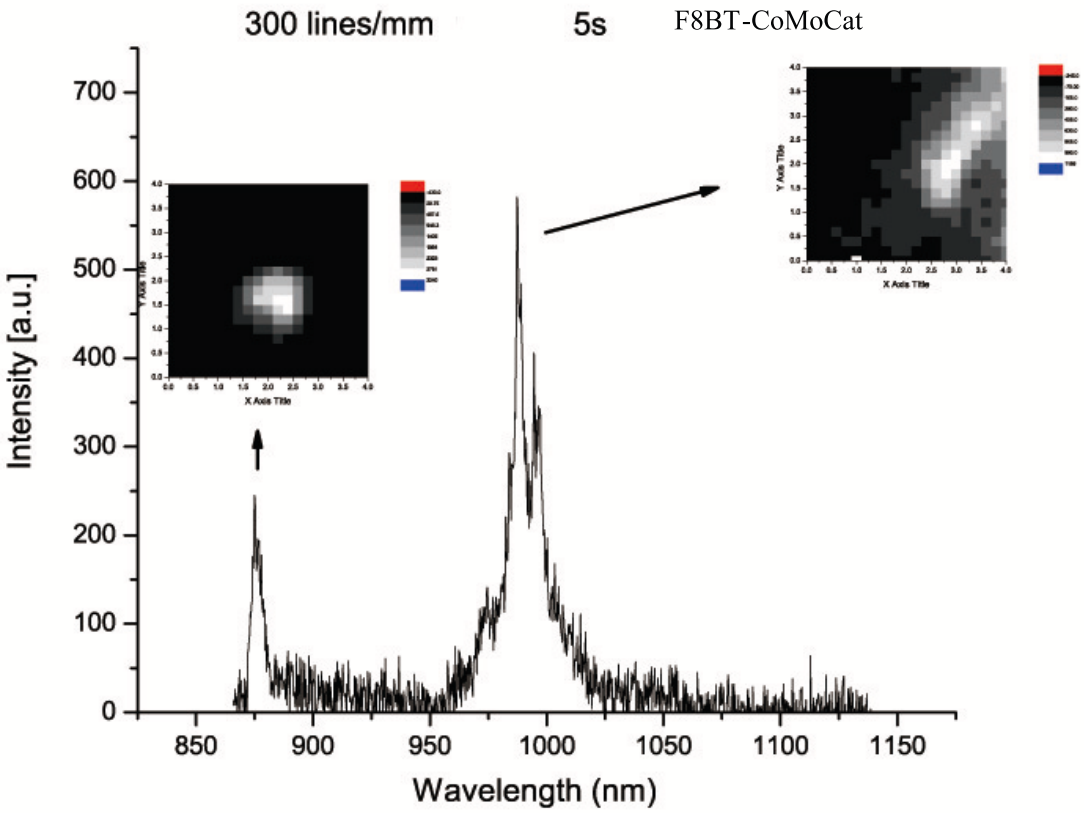


**Figure 5.7:** Single carbon nanotube found by spatial mapping.

processes in the emission of CNTs. These non-radiative relaxation processes set difficulties for studying CNTs at the single tube level. We used solid-immersion lens(SIL) on some of our sample surfaces to enhance both the excitation and collection areas [4] and managed to see our first single CNT spectra as shown in Figure 5.7. The spatial maps can be collected using the same method as discussed in Chapter 3. This is a sample with F8BT wrapped CoMoCat CNTs. The central peak at 993 nm is obviously a $(6, 5)$ tube. The doublet will be studied in more detail in the following sections and narrow emission with FWHM $\sim$ 4 meV can be seen. On the higher-energy side appears another single CNT-like peak can be assigned to a (8,3) nanotube.

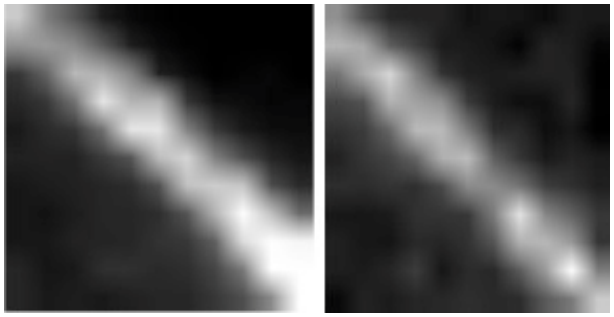

**Figure 5.8:** Since CNTs are wrapped by Polymers, so we can find polymer emission first, which is stronger.

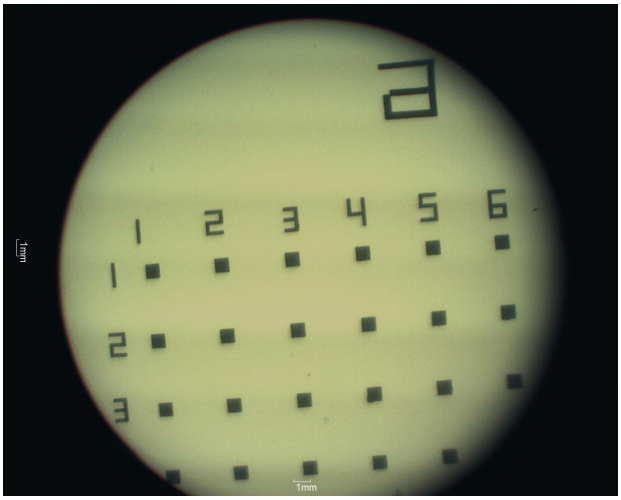


**Figure 5.9:** Image of design of a gold markers.

Polymer emission can also be a indication of the existence of single CNTs. As shown in Figure 5.8, the left-hand figure is luminescence from P3HT. The diameter of the white part is around 1$\mu$m which is limited to the spot size of the laser. The right-hand figure is luminescence from a $(6, 5)$ CNT at the same position. The same shape seen for both indicates that polymer emission ($\sim$680 nm as for P3HT) can be a guide to finding single CNTs ($\sim$993 nm as for (6,5) tube) owing to its stronger luminescence [112].

As the CNTs are scattered randomly on the surface of the substrate, it is almost impossible to return to the same tube to continue measurements on subsequent days. The solution is to pattern the substrate with registration marks, allowing the position

of any CNT to be found. In order to achieve this registration we designed a pattern composed of squares coded by letters and numbers as shown in Figure 5.9. A 60nm-think layer of gold was first deposited on a glass wafer. An e-beam machine was then used to transfer the pattern onto a resist spun on the gold, followed by chemical etching. The new substrates with the registration marks were then spin-coated with a low-density CNT solution.

### 5.3.3 Single CNTs

An upgraded CNT product has boosted our research on single CNTs. Normally the aggregated CNTs are purified with concentrated acid to get rid of the metallic and non-nanotube carbonaceous materials. However, this also cuts the bonds of tubes. Thus we used "nanotube sludge (unpurified tubes)" to obtain long single CNTs. An AFM image as in Figure 5.10 was taken to show the quality of the new CNT wrapped in PFO dispersed on a quartz wafer. Clearly one single CNT can be seen with 1 $\mu$m + length along with a diameter $\sim$1.2 nm. The bright dots are believed to be PFO nanocrystals of typical dimensions $3-10$ nm which are considered to limit contributions to the emission from CNTs [112].

Among all the compounds we used in our experiments, PFO wrapped CNTs are found to have the best single tube optical performance since PFO polymers, as opposed to other surfactant polymers, tend to be more separated from CNT surfaces. Thus they have a low charge compared to conventional ionic surfactants [123] and have the most stable hybrid system in (8,6) nanotube [124]. Figure 5.11 is a typical PL spectrum from a PFO-CNT. A super-narrow linewidth is observed with FWHM of $\sim$ 500 $\mu$eV, which is much less than any previously reported. We conclude this is an intrinsic property of the CNT unveiled by the polymer surfactant separating the CNT from the ambient environment while in the case of air suspended CNTs or ionic surfactant CNTs, charges will give rise

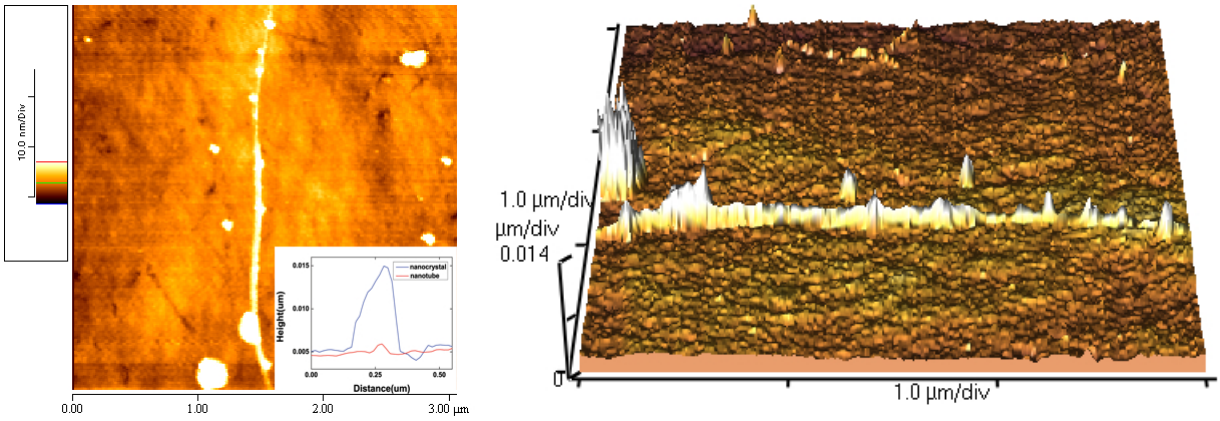


**Figure 5.10:** AFM images revealing one single CNT. The bright spots are PFO polymer nanocystals with a height around 3-10 nm as shown in the inset. The right hand is the same figure with a 3D view.

to broadening.

A detailed study can be carried out through PLE maps on single CNTs. Figure 5.12 is a PLE map recorded for excitation energies increasing by steps of 2 nm featuring a PFO wrapped CNT. Spectrally discrete peaks are seen. We expected the map to only be a zoom in of Figure 5.6, however, much more information can be deduced from this map. We assign peak at 1.735 eV as the main $E_{22}$ interband transition from (8,6) nanotube. Higher energy peaks of this peak can be attributed to both the contributions of state filling confinement and phonon absorption processes [125]. State filling spectroscopy will be mentioned again in the next section and plays a crucial role in the interpretation of the emission from a CNT as a single photon source. According to Bachilo et. al. [100], the radial breathing mode is located at 243.7 $cm^{-1}$ above the peak emission energy. Thus we assign peak at 1.77 eV as the radial breathing mode (RBM) phonon assisted absorption. When excitation is in resonance with the RBM mode, high intensity emission can be observed due to the strong electron phonon coupling brought in by the 1D confinement

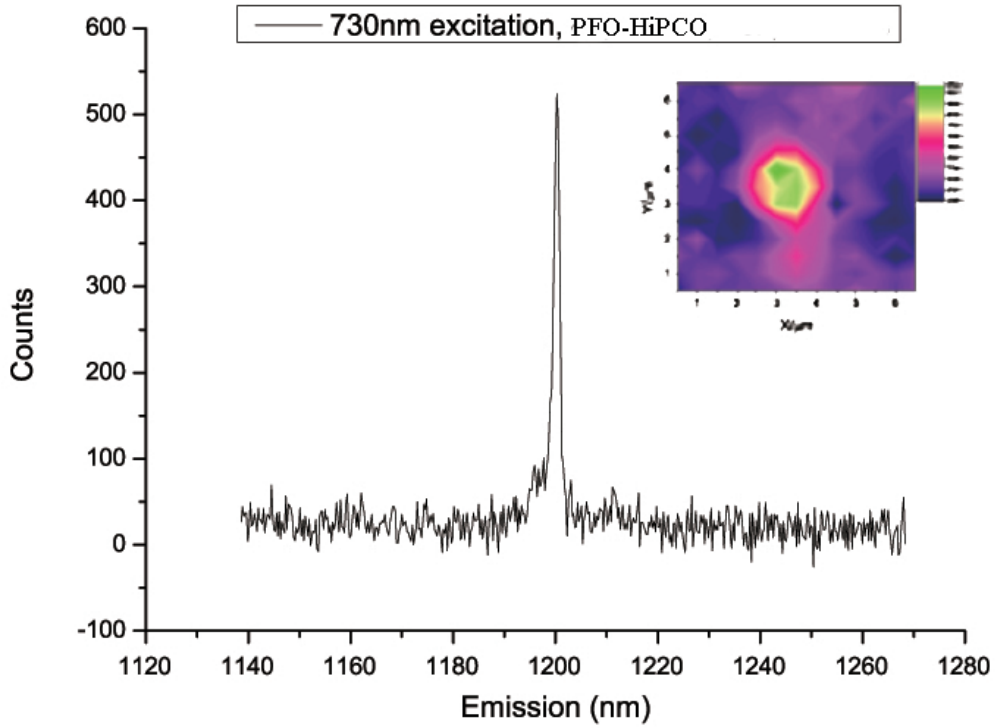


**Figure 5.11:** Single carbon nanotube wrapped in PFO emission at 1200nm. The inset is a spatial map showing the length of the single CNT is about 1$\mu$m.

structure [126]. The green streak below the main emission has been connected to multi-phonon relaxation and explained in ref. [125]. In general a PLE map is a very practical and efficient tool for studying various CNT properties. The 1D structure of CNT needs to be studied further and the phonon-exciton interaction is a key factor.

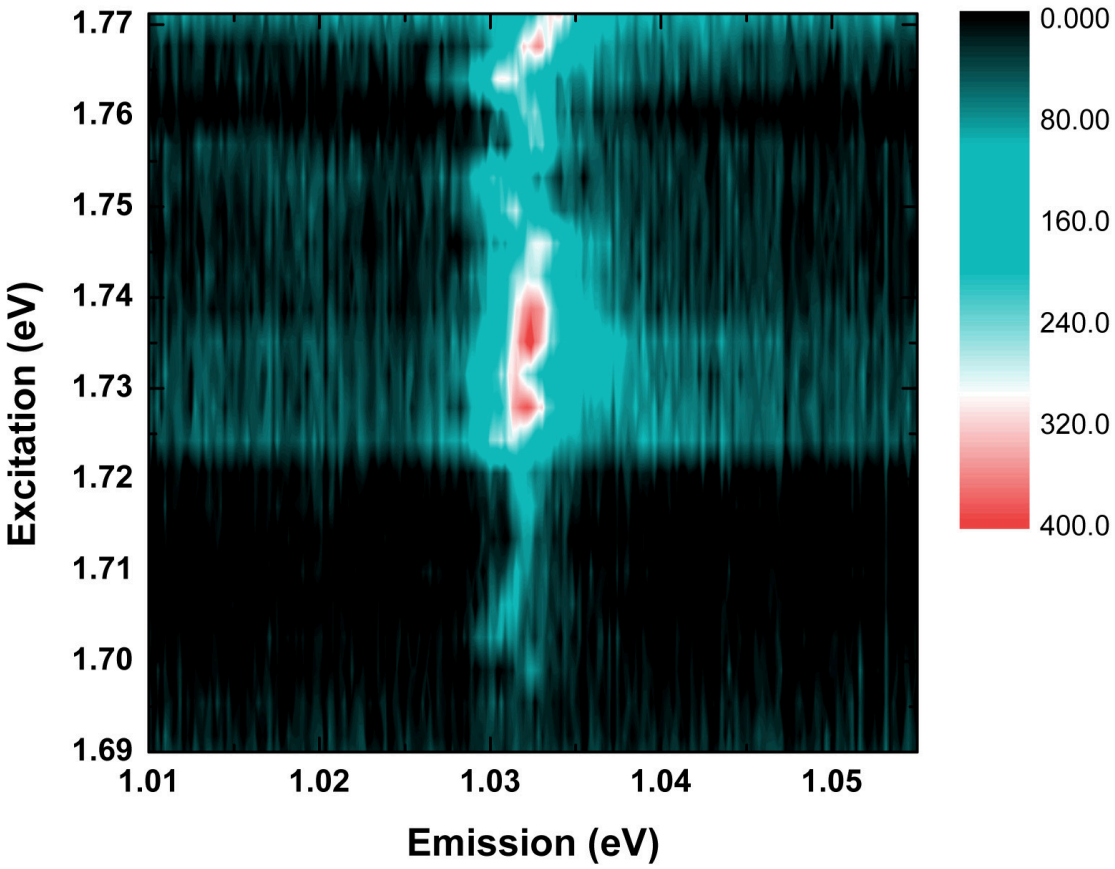


**Figure 5.12:** PLE from a single CNT with two major spots highlighting different transition schemes.

## 5.4 Quantum dots confined in single-walled carbon nanotubes

Various experiments have been carried out on the single CNT level. Thanks to the small diameter of semiconducting CNTs, the unintentional confinement of the electronic or excitonic states from small diameter semiconducting CNTs along the tube axis leads to odd (bright) and even (dark) singlet states and a mixing of two eigenstates [13, 117]. Theoretical work has predicted the existence of QDs inside CNTs due to disorder in semiconducting CNTs [127]. The observation of strong photon antibunching reinstated

this prediction [4]. In addition, the impurity centres such as polymer nanocrystals shown in Figure 5.10 could also separate the tube into a series of dots.

### 5.4.1 State filling spectroscopy of CNTs

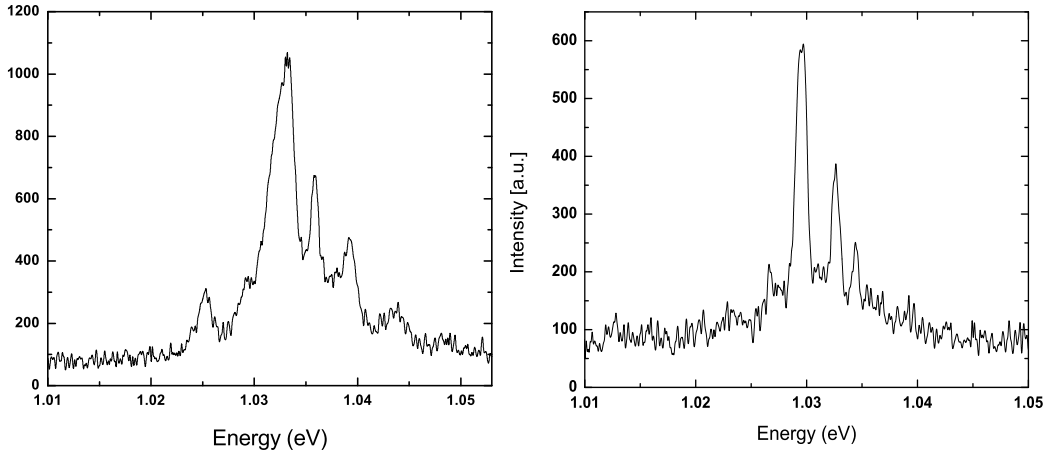


**Figure 5.13:** Two different PL spectra showing the state filling effect.

Quantum dot-like states are observed to form in small diameter nanotubes as shown in Figure 5.11, resulting in spatial confinement of excitons along the nanotube axis [128]. These states are easily recognised as the strong sharp spectral lines in photoluminescence spectra which are typical of quantum dots [129]. State filling spectroscopy is a well known phenomena in systems with confined discrete energy states such as InAs QDs we introduced in Chapter 3. Each energy level can be populated only by a certain number of relaxed carriers from excited states due to Pauli principle [130]. In CNTs, due to the rolled up structure from graphene, the allowed wave vector components perpendicular to the tube axis will be quantized and bring curvature effect to the density of states. This forms the VHS 1D subbands. In addition, impurity centres such as the polymer nanocrystals shown in Figure 5.10 could separate the tube into a series of quantum dots.

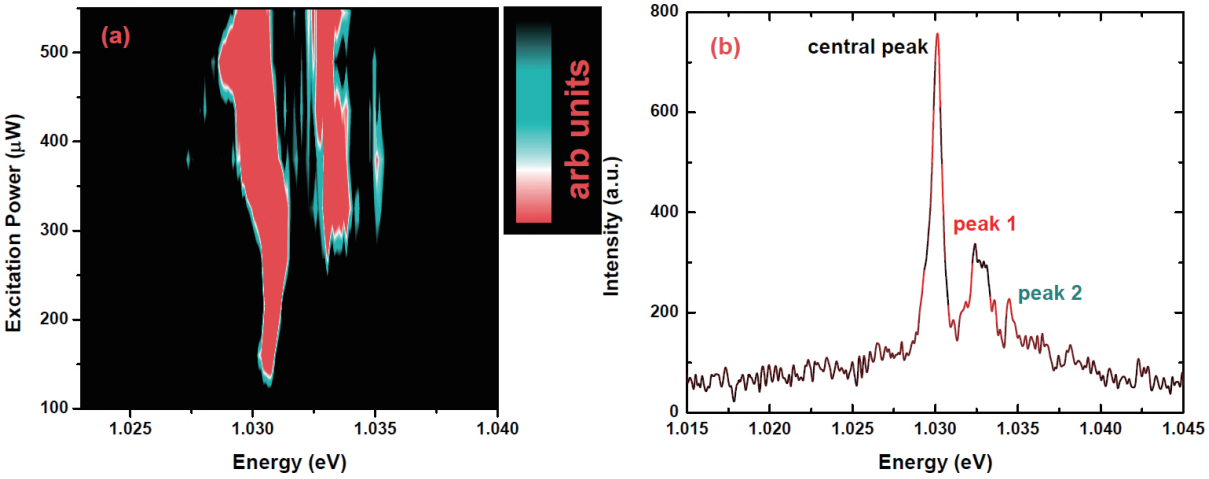


**Figure 5.14:** Power dependence measurement of an individual (8,6) CNT. (a) plot of excitation power against photon energy. New states are emerging with increasing excitation energy. The colors changing from black to green to red indicate an increase in peak intensity. (b) A spectrum showing the state filling effect in an (8,6) CNT.

Therefore we should be able to observe state filling effects when the excitation power is increased.

Figure 5.13 shows two examples of higher energy states we observed in our experiments. These are from different PFO-CNT samples with a fairly high excitation. Both figures have two obvious higher energy peaks and a lower energy shoulder. Appendix B provides a simulation of the narrow CNT lineshapes and an explanation to the main peak of Figure 5.13, which serves as a evidence of the existence of the state filling effect.

Figure 5.14 shows a series of spectra taken after individual (8,6) CNTs were excited with different powers. In the low energy regime, only one sharp peak with about 1meV FWHM is observed. When the excitation power is increased, new peaks at higher energy start to emerge as highlighted in the right Figure (b). The approximate equidistance of the emission features is similar to that seen in many self-assembled QDs. Note that saturation and a red-shift appears at higher power, which are also distinguishing features

of three-dimensional confinement of carriers in QDs.

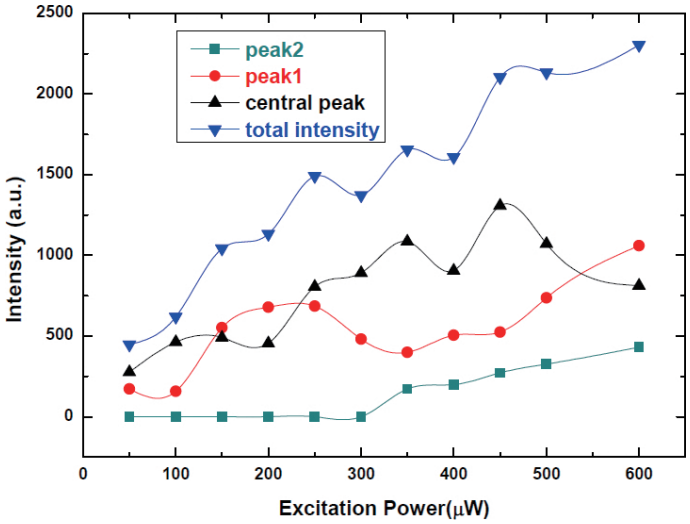


**Figure 5.15:** Power dependence measurement of an individual (8,6) CNT from 3 peaks originated from the same QD.

Figure 5.15 plots FWHM times the peak intensity vs excitation laser power of each peak depicted in Figure 5.14. The black, red and green lines indicate the central peak, peak 1 and peak 2 in Figure 5.14 (b), respectively. There is a strong correlation between each emission intensity, i.e., whenever the central peak intensity increases (decreases), peak 1 or 2 will decrease (increase) in sympathy. This clearly shows a correlation between each energy state and thus supports the assertion that these emission peaks originate from the same dot-like states. This is a strong demonstration of 3D confinement of carriers in single CNTs. Note the calculation in appendix B proves that the 3 peaks are not simply from different CNTs.

### 5.4.2 Spectral difusion and charge transfer in CNTs

It is well known that on-off blinking and spectral diffusion are common features in colloidal nanocrystals with energies determined by the quantum confined Stark effect

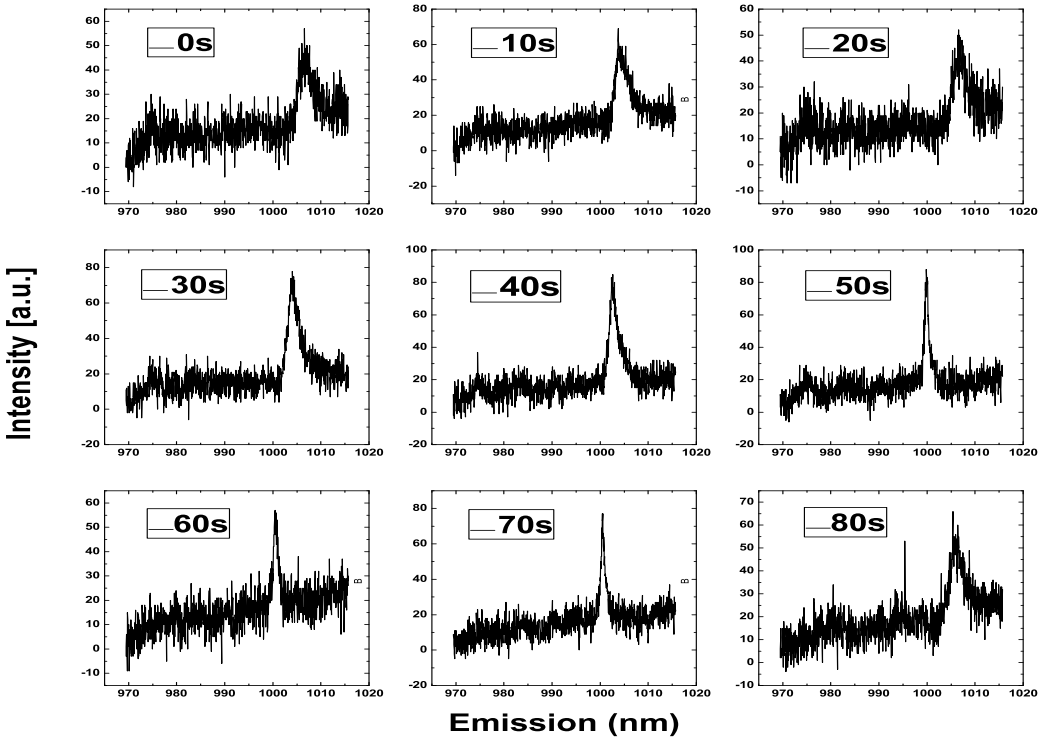


**Figure 5.16:** 9 spectrums showing a P3HT-CNT exhibiting spectral diffusion taken with 10 seconds intervals.

(QCSE) [131]. This phenomenon was also observed by Muller et al. in a unstable electrostatic environment with elongated nanocrystals [132].

In one dimensional quantum confinement structures such as CNTs, we observe variations in the PL of single nanotubes both in terms of intensity and spectral position. Figure 5.16 shows 9 continuous PL spectra from a P3HT (6,5) nanotube recorded every 10 seconds (integration time). Both linewidths and spectral positions keep changing.

One feature where our results differ from the random jittering reported previously is in the appearance of coherent on-off intensity oscillations with a well defined periodicity, discovered in some polymer wrapped CNTs. The first periodic observation was from a PFO-CNT bundle as highlighted in red in Figure 5.17. For $\sim$ every 4 mins the PL from the CNT bundle is seen to complete one period of oscillatory emission. We speculate this

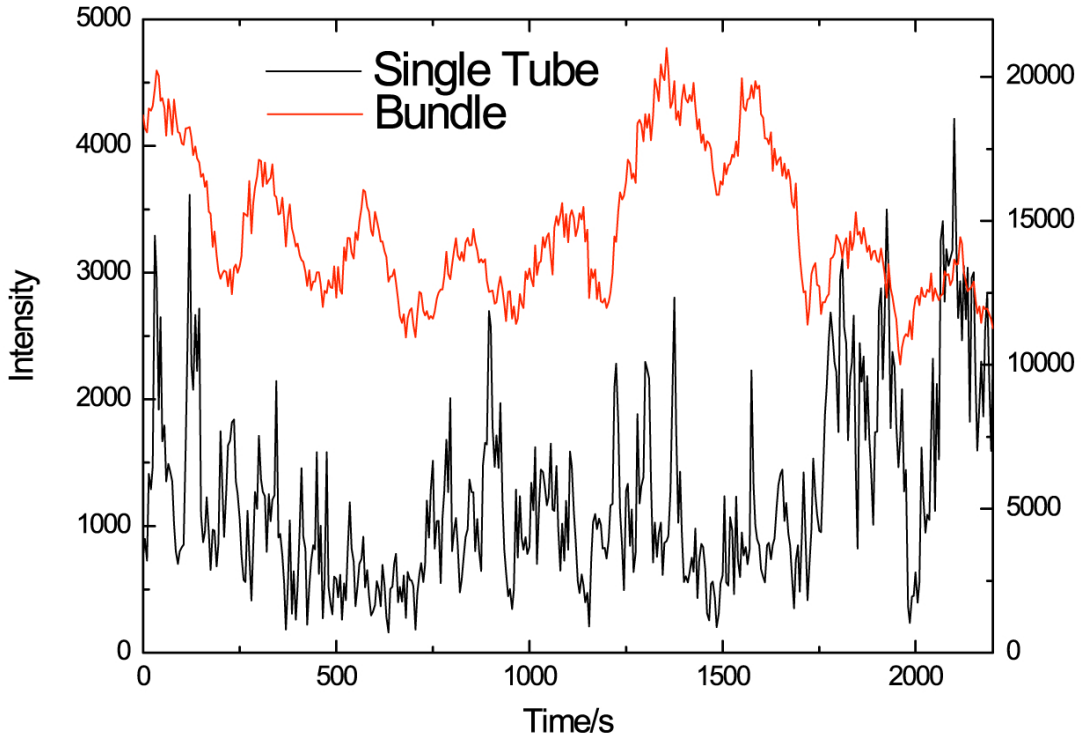


**Figure 5.17:** Spectral comparison of time evolutions from both a single CNT (black) and bundled CNTs.

background subtracted feature is indicating an average charge movement from individual CNTs. However, a single peak from a (8,6) CNT PL under the same excitation laser spot did not show any sign of periodicity.

For the single tube spectral diffusion, both peak position and intensity have been observed varying. The inset of Figure 5.18 shows a typical spectrum of single tube spectral wandering. The energy difference between the higher and lower energy peaks is about several meV. This is consistent with discoveries from other groups [133] [134]. Exciton localization has been attributed to the main reason of the jittering [128]. For example, if the exciton is localized at both polymer wrapped and unwrapped part, the

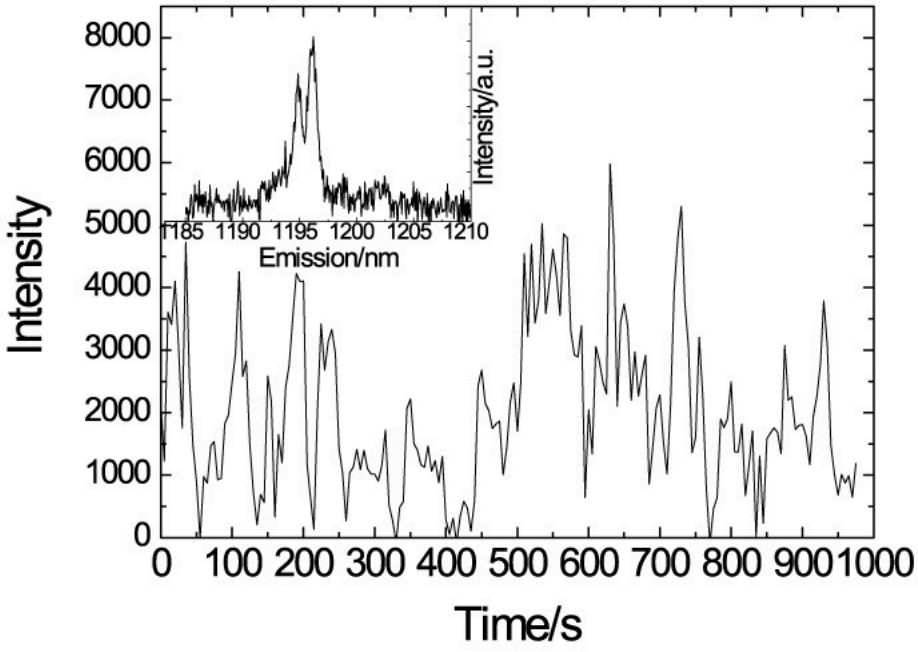


**Figure 5.18:** Time evolution of the intensity of one CNT PL spectra. Oscillation of diffusion is observed. The inset shows one typical PL from the single CNT.

spectrum will become a doublet due to the difference of local dielectric function.

To make things more obscure, a periodic single CNT spectral fluctuation was also found from a PFO-CNT as shown in Figure 5.18. This particular tube is spatially remote from any other features. A Fourier transform in Figure 5.19 indicates the period of the CNT oscillation as 46 seconds. Other similar periodic CNTs have also been observed with various jitter frequencies ranging from $45 - 320$ seconds. The variance in these frequencies provides a clear indication that the oscillations do not arise from a systematic experimental variation but arise from the intrinsic property of CNTs. It was not previously discovered because firstly, none of the studies, to our knowledge have encountered such narrow linewidths which we attribute to the homogeneous spontaneous

broadening from intrinsic CNTs. Secondly, the single CNT is remote from any bundle so any inter-tube charge transfer has been excluded.

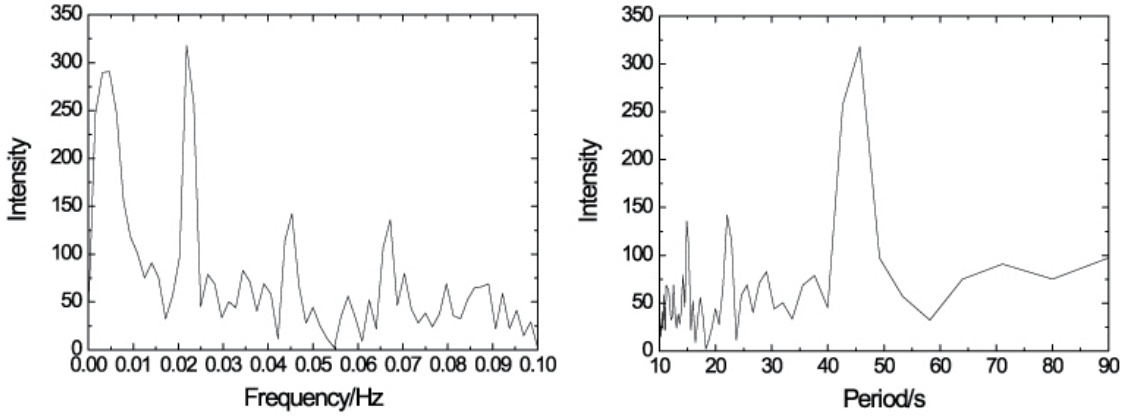


**Figure 5.19:** A Fourier transform of the bundle spectra shown in the red curve in Figure 5.17.

Luckily, an unique discovery might be able to help us explain the mysterious observations we have encountered. Figure 5.20 shows five PL spectra from the same spot on a single CNT at various times taken from the temporal evolution series on the right with an accumulation time of 10 s. Colors changing from black to red indicate a increase in emission intensity. The time separation between each spectrum is approximately 100 to 300 seconds. Surprising behavior was observed that the main peak from an (8,7) nanotube at 0.993 eV, which would disappear and relocate at 1.043 eV then shift back to its original energy. This is neither trion exciton nor phonon side band because of the un-matched energy separation of 40 meV [135] [136]. To explain this intriguing phenomenon, we compare the situation to the case of electron cotunneling in the Coulomb blockade regime [137] [138]. Backscattering within the tube would break the tube into a series of quantum dot-like confined electronic states. Even though localized states form, many electrons in the nanotube are still likely to be delocalized and traveling along the

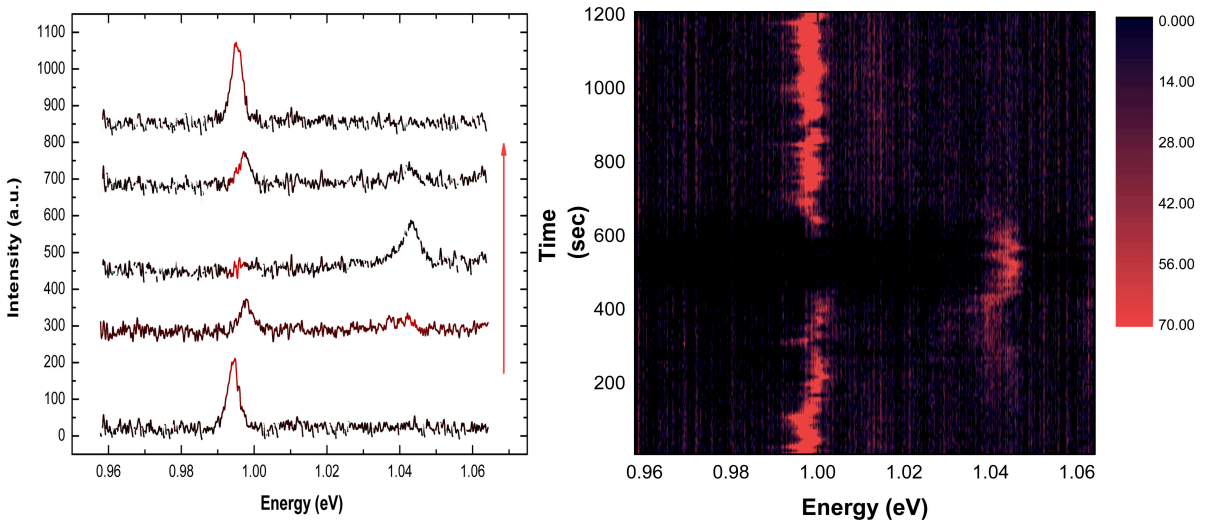


**Figure 5.20:** Temporal evolution of a single CNT. The figure on the left shows individual spectra taken from the one on the right. The data were collected by focusing the laser beam on a single CNT and collect the emission at every 10s. The colors changing in the right pane from black to red indicate increasing emission intensity.

tube axis. Charge exchange could then occur in this situation between these localized and delocalized states where the exchange rate was calculated to be 0.1 to 0.001 $s^{-1}$ depending on the environment [127].

To understand these spectral diffusion effects described above, one has to firstly consider the localized states in CNTs. We will discuss two types of localization below. The coupling of CNT surface carriers to their environment determines the local dielectric function, hence leads to variation in photoluminescence.

The first one is exciton localization. This has been studied in detail by other groups [139–141]. The observed energy variations mainly arise from different dielectric constants of the surrounding polymer. Take Figure 5.18 as an example, if the localized CNT part is under polymer wrapping, the radiative exciton recombination occurs locally and this will cause lower emission energy in the spectrum. If the localized exciton is `not` under polymer

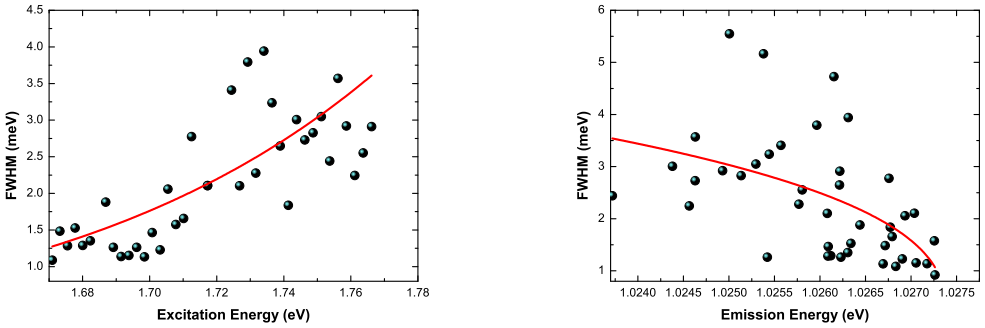


**Figure 5.21:** The PL linewidth (FWHM) of excitation and emission as a function of photon energy for a nanotube transition.

wrapping, higher emission in the spectrum will be seen. In addition, Stark effect due to localized charges can also vary the PL. Figure 5.21 plots the linewidth of the excitation energy and emission energy taken from one of the PLE maps in our investigation. The fluctuation-induced local field leads to a red shift in the exciton energy. The experimental data shows a square root energy dependence on the electric field which is highlighted in the red fitted lines, and this is consistent with previously reported experiments [133]. A further finding here is that the excitation energy also experiences a similar but opposite trend with the emitted photon energy. This is a clear evidence of reversible exciton transfer in both absorption and emission. Note the QCSE is a general observation in almost all our PLE maps and power dependent maps.

The second confinement scheme is quantum dots confined in CNTs. We have introduced this concept in the last section. In this typical case, polymer nanocrystals cut one tube into several dot-like segments. Under the same laser excitation in a confocal experiment, exciton can be formed in one QD-like state. If somehow the exciton can be transfered to the neighboring QD, then we might get a different high energy PL as we observed in Figure 5.20. However, the mobilized excitons tend to be trapped in lower energetic levels hence we observed the return of the emission energy [134] in PL spectrum.

Here we propose three possible schemes. The first one is electron cotunneling as in quantum dots in the Coulomb blockade regime. Impurity centres inside the nanotube can set barriers to free charge transport. Delocalized charges will then try to find the lowest activation energy and shortest hopping distance [142] which creates a channel for possible carrier transfer. This is not the preferred interpretation though, since there is insufficient evidence to explain the 40 meV energy difference and the reversible process. The second interpretation involves phonon assisted electron exchange. Due to the 1D structure of CNTs, phonons have been proven to play a crucial role in the optical transitions of CNTs. The exciton performance is also severely affected depending on the phonon-electron interaction. If the exciton is coupled with an optical phonon, such as we observed in Figure 5.6, its relaxation by emitting phonons can form a non-equilibrium population of phonons. The strong electron-phonon coupling proposed in these 1D structures then allows two adjacent QD-like states in the nanotube to interact with each other via this phonon population, allowing a new exciton to form. However, this is not a stable energy due to the existence of the phonon population and the fluctuation of localized charges arising from the QCSE [132]. In this scheme, low temperature is expected to quench the PL intensity due to the less populated phonons so that the phonon assisted charge transfer has limited occurrence possibility which is consistent with the 0.1 to $0.001\,s^{-1}$ rate mentioned above. The third possible charge exchange scheme is through the polymer backbone. In this particular case, as energy transfer from PFO to CNTs, electrons are confined in the nanotube. However, holes are probably created in the polymer. On the PFO-HiPCO interface network, a bound state charge transfer would produce free polarons. The polarons along with the remaining holes can form a weak "exciplex" as described in ref. [112]. At the same time, the escaped electrons can be trapped in the new QD and this generates the higher energy peak we observed in Figure 5.20. The weak exciplex bond will relax by emitting nonradiatively, and a reverse transition could then

happen in the same way. The real picture of observed charge transfer could, of course, be a combination of all 3 schemes proposed above. The quantitative analysis of the whole process, though, needs further theoretical investigation.

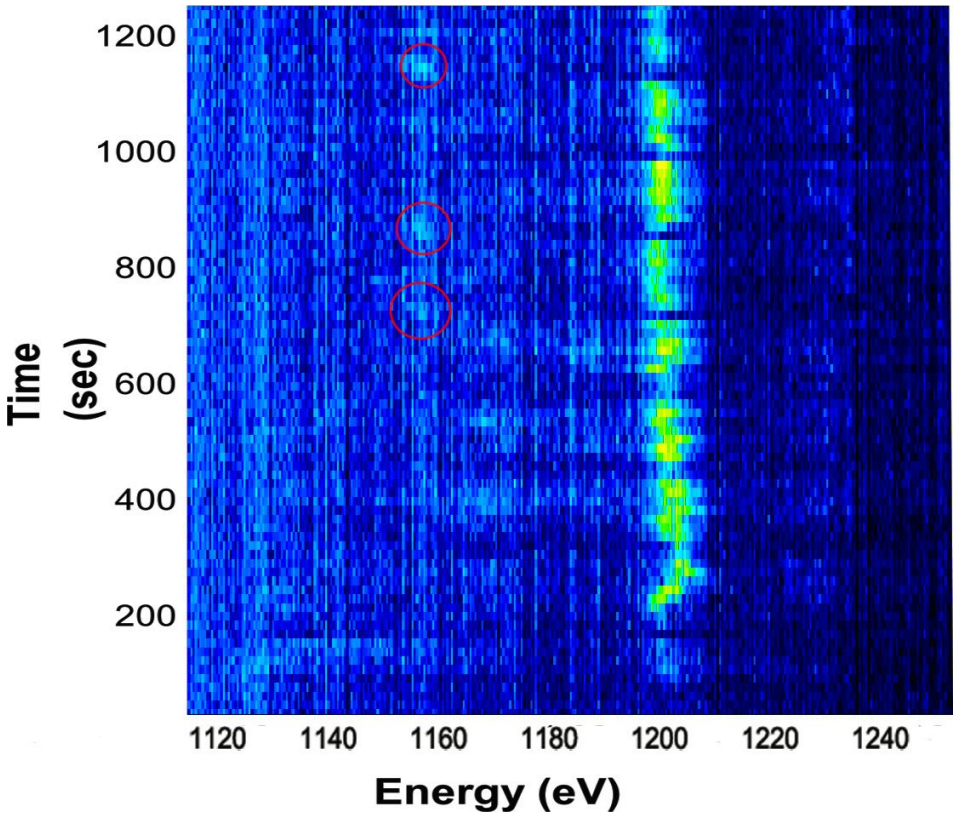


**Figure 5.22:** Periodical appearance of CNT emission, quantum dot confined charge transfer appears at 1158 nm as highlighted in red circles.

We can further predict that if the QDs are arranged at a certain distance apart then periodic oscillation of charge transfer would occur as we observed in some of our experiments as shown in Figure 5.22 as the spots highlighted in red circles. For the same reason, when the separation between dots is irregular, the random charge exchange could occur as we have seen in Figure 5.20. Note both the photon energy and linewidth of the original peak in Figure 5.20 differ from the new peak at higher energy, the same situation is also true in Figure 5.22 at 1158 nm with weaker visibility.

## 5.5 CNTs as single photon sources and future work

We previously focused on intratube excitonic interactions and proved the local confinement in CNTs. This strong confinement in CNT QDs made the CNT a good candidate for applications as single photon sources. The ETH group pioneered the idea of photon antibuching from single CNTs [4]. This fascinating idea can be firmly explained by the QD confinement introduced in the previous section. We have an nontrivial discovery here, which might contribute to the general single photon generation idea for single CNTs.

As we can see from the previous PLE maps, while changing the excitation energy, the CNT QD exciton could move in one spectral direction. If a cavity mode induced by the 1D tube structure is at the same time moving towards the dot emission, an interaction between them is likely to occur. In Figure 5.23, two emission lines started from 700 nm and began to approach each other while increasing the excitation wavelength. An anticrossing-like feature appears at 720 nm and the peaks start to shift away until a strong emission at the resonance $E_{11}$ intersubband transition energy is seen.

An estimated Q of 2500 according to conditions set in the previous chapter is probably not enough to conclude that this is strong coupling in a nanotube. A systematic study of the CQED inside CNTs is necessary, which for practical considerations will be quite demanding. However, the possible application of CNTs in quantum equipment including single photon sources and quantum qubits is a realistic possibility given our early results.

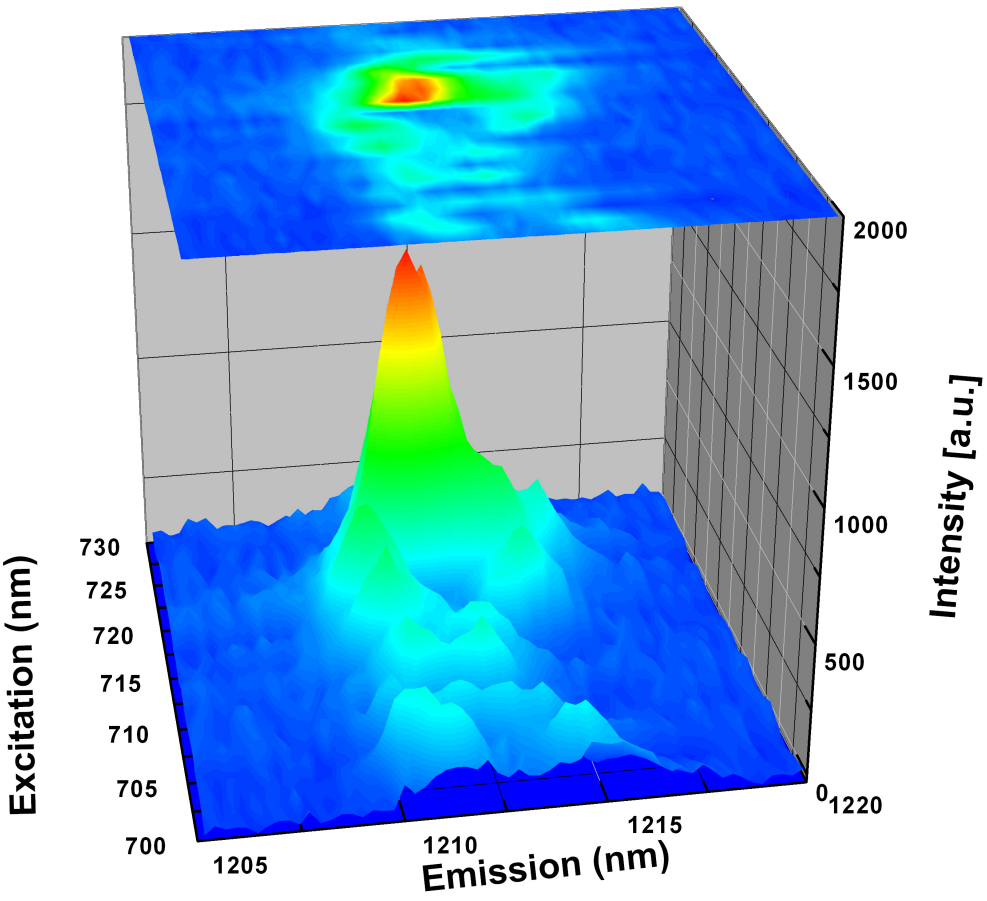


**Figure 5.23:** A PLE map shows signs of anticrossing.

# Chapter 6

# General conclusion and outlook

Single photon sources in the infrared have been thoroughly studied in this thesis. Photon correlation measurements are not covered in this work, mainly because both the potential candidates have shown antibunched light emission. There are also many other single popular potential SPSs such as ion trap and diamond NV centers but due to their bluer emission energies, they are not included in this work either.

The FDTD algorithm has been introduced and applied by using the MEEP software package. We matched the leaky modes of a photonic crystal slab to the three metal nitride doped fullerene $Er_3N@C_{80}$ emission peak at 1519 nm and absorption peak at 1492 nm. Given the enhanced near-field electric-field intensity distribution simulations, optimal fluorescence emission is expected when the leaky modes of the PhC are coupled with the excitation and emission peaks of $Er_3N@C_{80}$. The device is currently being fabricated. The PhC with predicted parameters are already prepared and we are expecting to see emission and absorption enhancement after spin coating fullerenes on. It is worthwhile to point out that this leaky mode matching method should be able to applied to other materials such as carbon nanotubes.

InAs quantum dots within photonic band gap micro-cavities have been successfully fabricated. With state of art growth control, we obtain low density ($3 \times 10^8$ $cm^{-2}$)

infrared (beyond 1200 nm) high quality QDs. Both time-integrated and time-resolved measurements have been taken place to reveal the optical transition in single QDs. Two methods are utilised to register the dot position so that we can write the photonic crystals at the perfect place where the dot is spectrally and spatially placed at the anti-node of the cavity mode. SU-8 lithography can accurately register a single QD. However, the chemical deposition complicates the whole process and furthermore, contamination and SU-8 adhesion always seems to be an issue. Thus, we developed a neat technique simply by scanning laser across the pre-written pattern. The Gaussian fit to the reflecting profile determines where the dot is positioned relevant to the marker edges. This method has to be repeated multiple number of times to minimize the system errors. Thermal drift is always a concern so we have to limit the time spent on each optical registration processes [143]. We are currently waiting for new QD samples to test this scanning registration method. In the mean time, high density dot samples have been coupled to PhCWGs and a distinctive strong coupling effect has been observed. This is of fundamental importance as it applies to non-linear quantum optics and quantum information processing. Nevertheless, it should be noted that if a system is far into the strong coupling regime, it is generally *not* suitable for single-photon generation [144]. We calculated our design boundary of the strong coupling regime as around Q = 4000. For an actual device of Q = 8000, we deduced a Rabi splitting energy $E$ of about 140 $\mu$eV. The main obstacle in achieving the maximum coupling strength is the misalignment between the QD and the antinode of the cavity mode. This is extremely important especially in the low density dot sample scenario. The QD registration techniques introduced in Chapter 3 thus become the key process of our protocol.

We synthesised high quality single-walled carbon nanotubes in the form of bundles or separated single tubes by means of polymer surfactant. The optical properties of CNTs severely depend on their diameter, chirality and surrounding environment. We

have tried many different ways to look for PL from single CNTs. The main issue is the existence of dominant nonradiative decay channels and environmental induced diffusion. The ideal situation would be depositing low density CNT solution on a masked wafer and then placing a SIL at the desired region. This would enable us to do a complete study on only one tube. In addition, coupling CNTs with micro-cavities is another solution. Enhancement of both absorption and emission is expected and we can apply most of the technique introduced in Chapter 3 and 4. PLE spectra have shown clear evidence of the existence of excited states. We were not able to test more CNTs with various chiralities due to the limit of our excitation sources. Spectral diffusion reveals the existence of QD-like states which supports the prediction that single-walled carbon nanotubes can be fabricated into single photon sources.

# Appendix A

# 2-D photonic crystal slab MEEP code

```
; MEEP code
; Xu Wang

; The structures of model:
; Square lattice of holes with period = 300nm and radius = 90nm
; PML layer
; Air layer ( where the source plane is in)
; Layer A TiO2 with air holes, thickness = 100nm
; Layer B TiO2, thickness = 25
; Layer C SOG with TiO2 holes, thickness = 100nm
; Layer D SOG, thickness ¬200nm
; Substrate (glass)
; PML layer (the material is the same with the adjacent one)

; when use-pc?=false then there will be no structure, just for normalization
; when spol?=false then the polarization will be p-polarized
```

```
17
18 (define-param use-pc? true)
19 (define length-scale 300)
20 (define-param spol? true)
21
22 (define TiO2 (make dielectric (index 2.46)))
23 (define glass (make dielectric (index 1.46)))
24 (define SOG (make dielectric (index 1.17)))
25
26 ; Choose the period of lattice to be unit distance, a
27
28 (define z-A (/ 100 length-scale))
29 (define z-B (/ 25 length-scale))
30 (define z-C (/ 100 length-scale))
31 (define z-D (/ 200 length-scale))
32 (define pad-sub 5)
33 (define pad-air 5)
34 (define rad (/ 90 length-scale))
35
36 (define sx 1)
37 (define sy 1)
38 (define z-pml 2)
39 (define sz (+ (* 2 z-pml) pad-air z-A z-B z-C z-D pad-sub))
40
41 (define centre-sub (- (* 0.5 (+ z-pml pad-sub)) (* 0.5 sz)))
42 (define centre-D (+ centre-sub (* 0.5 (+ z-pml pad-sub z-D))))
43 (define centre-C (+ centre-D (* 0.5 (+ z-D z-C))))
44 (define centre-B (+ centre-C (* 0.5 (+ z-C z-B))))
45 (define centre-A (+ centre-B (* 0.5 (+ z-B z-A))))
46
47 ; define the centers of slices to output
48
```

```
49 ;(define center-upper (+ centre-A (* 0.5 z-A)))
50 ;(define center-lower (- centre-A (* 0.5 z-A)))
51
52 (if use-pc?
53
54     (set! geometry (list
55         ; Substrate
56             (make block
57               (center 0 0 centre-sub)
58               (size sx sy (+ z-pml pad-sub))
59               (material glass))
60             ; SOG
61             (make block
62               (center 0 0 centre-D)
63               (size sx sy z-D)
64               (material SOG))
65         ; PC layer C
66             (make block
67               (center 0 0 centre-C)
68               (size sx sy z-C)
69               (material SOG))
70             (make cylinder
71               (center 0 0 centre-C)
72               (radius rad)
73               (height z-C)
74               (material TiO2))
75         ; TiO2 layer B
76             (make block
77               (center 0 0 centre-B)
78               (size sx sy z-B)
79               (material TiO2))
80         ; PC layer A
```

```
81              (make block
82                (center 0 0 centre-A)
83                (size sx sy z-A)
84                (material TiO2))
85              (make cylinder
86                (center 0 0 centre-A)
87                (radius rad)
88                (height z-A)
89                (material air)))))
90
91 ;define our cell
92 (set! geometry-lattice (make lattice (size sx sy sz)))
93 (set! pml-layers (list (make pml (thickness z-pml) (direction Z))))
94
95 (set-param! resolution 48)
96
97 ; pw-amp is a function that returns the amplitude exp(ik(x+x0)) at a
98 ; given point x.  (We need the x0 because current amplitude functions
99 ; in Meep are defined relative to the center of the current source,
100 ; whereas we want a fixed origin.)  Actually, it is a function of k
101 ; and x0 that returns a function of x ...
102 (define ((pw-amp k x0) x)
103   (exp (* 0+1i (vector3-dot k (vector3+ x x0)))))
104
105 ; Want to calculate transmission from 450nm-650nm
106 (define fmin (/ length-scale 650))
107 (define fmax (/ length-scale 450))
108 (define-param fcen (* 0.5 (+ fmin fmax))) ; pulse center frequency
109 (define-param df (- fmax fmin)) ; turn-on bandwidth
110
111 ; Only care about k parallel for PBCs and for source direction (phasing)
112 ; Want to scan in the Gamma-M direction - [110]
```

```
113 ; Suggest we keep |kpara| =  0+∆!...0.5*fcen/c
114 ; (At fcen ONLY angle of incidence is in range 0+∆!..30deg)
115 (define-param kpara-fraction 0.1)
116 ; No 2pi yet!
117 (define kpara (vector3 (* kpara-fraction (sqrt 0.5) fcen)
118                (* kpara-fraction (sqrt 0.5) fcen)
119                0))
120
121 (define kpara-2pi (vector3-scale (* 2 pi) kpara))
122
123 (define amp-z kpara-fraction)
124 (define amp-x (sqrt (* 0.5 (- 1 (* amp-z amp-z)))))
125 (define amp-y amp-x)
126
127
128 (set! k-point kpara) ; use PBCs
129
130 (set! sources
131    (if spol?
132       (list
133        (make source
134      (src (make gaussian-src (frequency fcen) (fwidth df)))
135      (component Ex)
136      (center 0 0 (- (* 0.5 sz) z-pml))
137      (size sx sy 0)
138      (amplitude (sqrt 0.5))
139      (amp-func (pw-amp kpara-2pi (vector3 0 0 (- (* 0.5 sz) z-pml)))))
140        (make source
141      (src (make gaussian-src (frequency fcen) (fwidth df)))
142      (component Ey)
143      (center 0 0 (- (* 0.5 sz) z-pml))
144      (size sx sy 0)
```

```
145       (amplitude (- (sqrt 0.5)))
146       (amp-func (pw-amp kpara-2pi (vector3 0 0 (- (* 0.5 sz) z-pml))))))
147        (list
148         (make source
149       (src (make gaussian-src (frequency fcen) (fwidth df)))
150       (component Ex)
151       (center 0 0 (- (* 0.5 sz) z-pml))
152       (size sx sy 0)
153       (amplitude amp-x)
154       (amp-func (pw-amp kpara-2pi (vector3 0 0 (- (* 0.5 sz) z-pml)))))
155         (make source
156       (src (make gaussian-src (frequency fcen) (fwidth df)))
157       (component Ey)
158       (center 0 0 (- (* 0.5 sz) z-pml))
159       (size sx sy 0)
160       (amplitude amp-y)
161       (amp-func (pw-amp kpara-2pi (vector3 0 0 (- (* 0.5 sz) z-pml)))))
162         (make source
163       (src (make gaussian-src (frequency fcen) (fwidth df)))
164       (component Ez)
165       (center 0 0 (- (* 0.5 sz) z-pml))
166       (size sx sy 0)
167       (amplitude amp-z)
168       (amp-func (pw-amp kpara-2pi (vector3 0 0 (- (* 0.5 sz) z-pml)))))))))
169
170
171 ; flux plane for transmission(at the bottom of the structure,
172 ; just above the PML-glass)
173
174 (define-param nfreq 101)
175 (define trans
176   (add-flux fcen df nfreq
```

```
177              (make flux-region
178                (center 0 0 (- z-pml (* 0.5 sz)))
179                (size   sx sy 0))))
180
181 ;run the simulation
182
183 (define-param dT 10)
184 (run-sources+ (stop-when-fields-decayed dT
185                          Ex
186                          (vector3 0 0 (- z-pml (* 0.5 sz)))
187                          1e-3)
188            (at-beginning output-epsilon))
189
190          (display-fluxes trans)
```

# Appendix B

# Modeling of electron phonon coupling in CNTs

The PL lineshape is primarily governed by the interaction of excitons with 1D acoustic phonons, and can therefore be treated theoretically using an independent boson model [13]. The 1D acoustic phonons discussed here include three important modes, a stretching (S) mode, a twisting (T) mode, and a radial breathing (RBM) mode. The stretching mode corresponds to the deformations of the nanotube along the tube axis. With small wave vectors it has linear dispersion $\omega_s(q) = v_s q$ with $q$ as the phonon wave vector [145]. The twisting mode mediates the nanotube polarized along its circumference. We neglect the coupling of electrons to twisting mode due to the small coupling strength. The RBM alters the effective tube diameter and its major contribution is the appearance of phonon sidebands.

We assume a harmonic confinement localizes the exciton in CNTs with well defined energy splitting $\Delta \mathrm{E} \gg k_{\mathrm{B}} T$ and this system is independent from the surrounding environment. As described in Ref. [13] we have the exciton $-$ phonon coupling matrix elements:

$$g_j(q) = G_j(q) F^{exc}(q) \tag{B.1}$$

where $j$ stands for either an $S$ mode or a RBM mode. The first factor, the bulk coupling matrix element $G$ in equation 5.2, depends on the specific coupling mechanism:

$$G(q) = D/\sqrt{2\rho L\hbar\omega(q)} \tag{B.2}$$

with $D$ the mode strength, $L$ the length of the CNT and $\rho$ the linear mass density. The form factor $F^{\mathrm{exc}}$ can be calculated from the wave function $\Psi^{\mathrm{exc}}(z)$ of the electron and hole within the CNT potential:

$$F^{\mathrm{exc}}(q) = \int dz |\Psi^{\mathrm{exc}}(\mathbf{z})|^{\mathbf{2}} \mathbf{e}^{\mathbf{iq}\cdot\mathbf{z}} \tag{B.3}$$

with $\Psi^{\mathrm{exc}}(\mathbf{z})$ consisting of a Gaussian envelope along z :

$$\Psi^{exc}(z) = \frac{1}{\pi^{1/4}\sigma^{1/2}} exp(-\frac{z^2}{2\sigma^2}) \tag{B.4}$$

we then get $F^{\mathrm{exc}}(q) = \exp(-\frac{q^2\sigma^2}{4})$ and $\Delta E = \frac{\hbar^2}{m^*_{\mathrm{exc}}\sigma^2}$ with $m^*_{\mathrm{exc}}$ the exciton effective mass. $\sigma$ is the confinement length. Figure B.1 shows our fitting to experimental data. The red line perfectly fitted to PL from the PFO-HiPCO CNT. We used $\sigma = 3$ nm and $L$= 1500 nm with $m^*_{\mathrm{exc}} \backsimeq 0.2$, the assumption $\Delta E \gg k_B T$ is adjusted. Thus our model works well with strongly confined nanotubes.

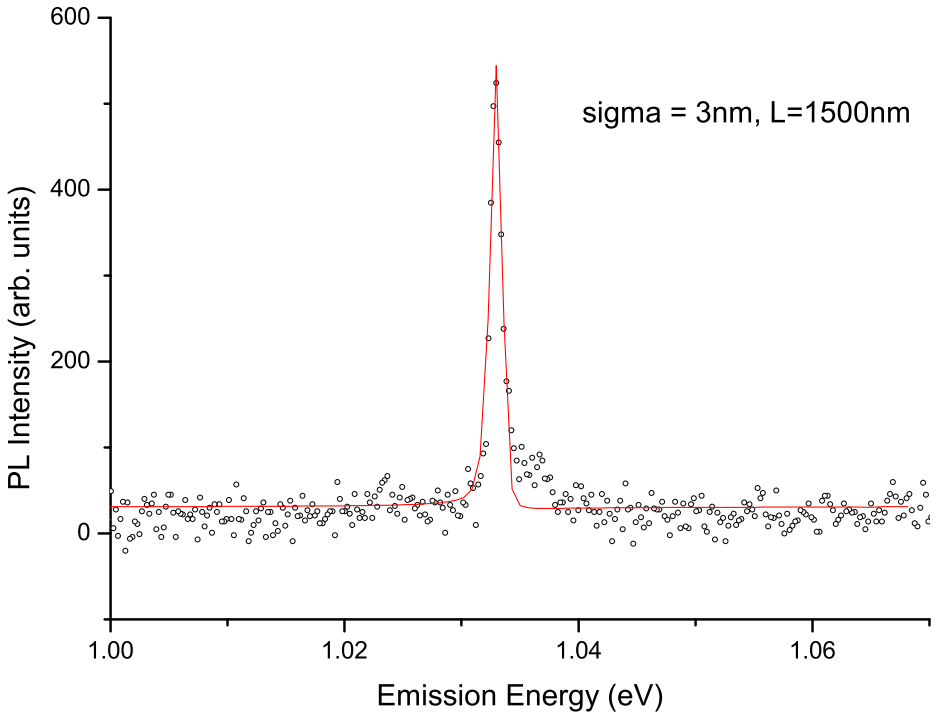


**Figure B.1:** Boson modeling of an experimental signal from PFO-HiPCO CNT. Dots show the experimental data while the red line is theory fitting.

With $g_j(q)$ we can model the absorption spectrum of the CNT by a Fourier transformation of its linear susceptibility $\chi(\mathrm{t})(t \geq 0) = -ie^{-i\bar{\Omega}_T(t)}\chi_T(t)\chi_0(t)$, with temperature-dependent and independent part as:

$$\chi_{\mathrm{T}}(t) \propto \begin{cases} i\exp(\sum_q |\gamma_{\mathrm{S,RBM}}(q)|^2[-n_{\mathrm{S,RBM}}(q)|e^{-i\omega_{\mathrm{S,RBM}}(q)t} - 1|^2]) & \text{(B.5)} \\ i\exp(\sum_q |\gamma_{\mathrm{S,RBM}}(q)|^2[e^{-i\omega_{\mathrm{S,RBM}}(q)t} - 1]). & \text{(B.6)} \end{cases}$$

where $\gamma_j(q) = g_j(q)/\omega_j(q)$, phonon occupation number $n_j(q) = (e^{\hbar\omega_j(q)/k_{\mathrm{B}}T} - 1)^{-1}$ and the polaron-shifted transition energy is $\bar{\Omega} = \Omega - \sum_{j,q} |\gamma_j(q)|^2\omega_j(q)$.

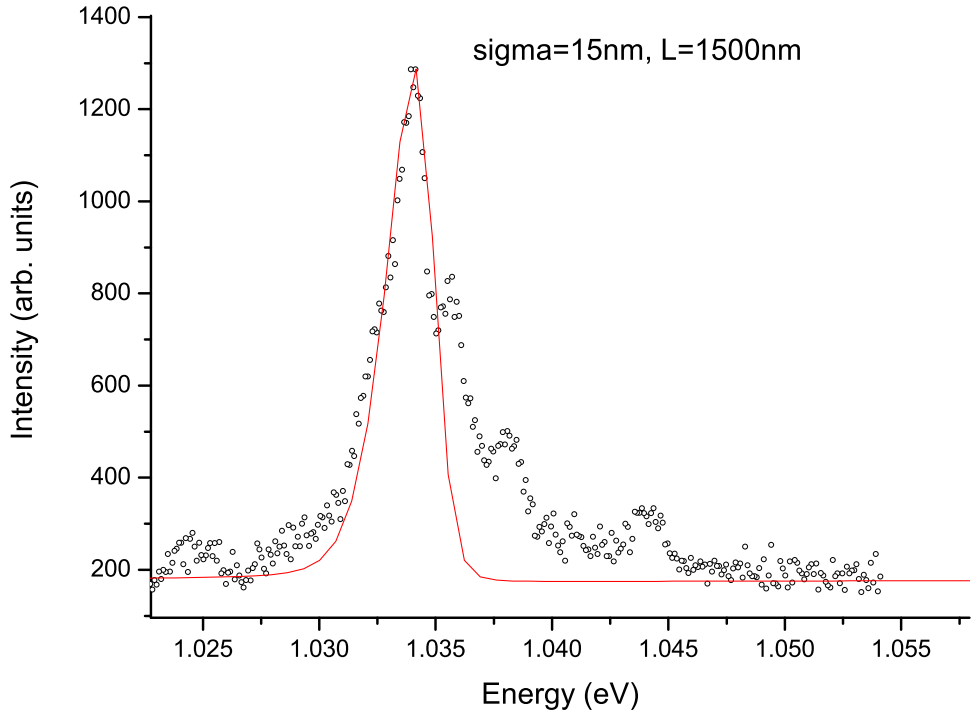


**Figure B.2:** Boson modeling of a multi-peak spectrum from a PFO-HiPCO CNT. Dots show the experimental data while the red line is a theoretical fit.

Figure B.2 shows a fit of the theory to a multi peak spectrum. We have to adjust the $\sigma$ to 15nm thus $\Delta E$ is no longer much larger than $k_{\mathrm{B}}T$, i.e. weak confinement. The experimental data cannot be properly fitted because of the higher energy peaks. However, this is not a bad thing since it provides evident to support the assertion that luminescence originates from quantum dot confinement. If the equidistance peaks observed in Figure B.2 are from different states of the same QD, then state filling effects will quench the confinement. There is therefore an issue of 3-dimensional confinement which we discussed in chapter 5.

# Bibliography


[1] D. F. Charles Santori and Y. Yamamoto, *Single-photon Devices and Applications* (Wiley, Germany, 2010).

[2] C. Kittel, *Introduction to Solid State Physics*, 7 ed. (Wiley, New York, 1996).

[3] K. Hennessy, A. Badolato, M. Winger, D. Gerace, M. Atature, S. Gulde, S. Faelt, E. L. Hu, and A. Imamoglu, Nature **445**, 896 (2007).

[4] A. Hogele, C. Galland, M. Winger, and A. Imamoglu, Physical Review Letters **100**, 217401 (2008).

[5] T. Nakaoka, S. Kako, and Y. Arakawa, Phys. Rev. B **73**, 121305 (2006).

[6] A. D. Andreev and E. P. O'Reilly, Phys. Rev. B **62**, 15851 (2000).

[7] T. Saito and Y. Arakawa, Physica E **15**, 169 (2002).

[8] C. Santori, D. Fattal, J. Vuckovic, G. Solomon, and Y. Yamamoto, Nature (London) **419**, 594 (2002).

[9] R. B. Patel, A. J. Bennett, I. Farrer, C. A. Nicoll, D. A. Ritchie, and A. J. Shields, Nature Photonics **4**, 632 (2010).

[10] G. Bester and A. Zunger, Phys. Rev. B **71**, 045318 (2005).

[11] L. W. Wang and A. Zunger, Phys. Rev. B **51**, 17398 (1995).

[12] F. Wang, G. Dukovic, E. Knoesel, L. E. Brus, and T. F. Heinz, Phys. Rev. B **70**, 241403 (2004).

[13] C. Galland, A. Hogele, H. E. Tureci, and A. Imamoglu, Phys. Rev. Lett. **101**, 067402 (2008).

[14] E. Gaufres, N. Izard, X. L. Roux, S. Kazaoui, D. Marris-Morini, E. Cassan, and L. Vivien, Applied Physics Letters **18**, 5740 (2010).

[15] A. Pawlis, A. Khartchenko, O. Husberg, D. As, K. Lischka, and D. Schikora, Solid State Communications **123**, 235 (2002).

[16] M. B. Ward, D. C. Unitt, Z. Yuan, P. See, R. M. Stevenson, K. Cooper, P. Atkinson, I. Farrer, D. A. Ritchie, and A. J. Shields, Solid State Communications **21**, 390 (2004).

[17] S. P. Walborn, M. O. Terra Cunha, S. Pádua, and C. H. Monken, Phys. Rev. A **65**, 033818 (2002).

[18] R. J. Glauber, Physical Review **131**, 2766 (1963).

[19] P. W. Shor, SIAM Review **41**, 303 (1999).

[20] D. Bouwmeester, A. Ekert, and A. Zeilinger, *The Physics of Quantum Information* (Spinger, Berlin, 2000).

[21] J. S. Bell, *Collected Papers on Quantum Philosophy: Speakable and Unspeakable in Quantum Mechanics* (Cambridge Univ. Press, Cambridge, 1987).

[22] D. Press, T. Ladd, B. Zhang, and Y. Yamamoto, Nature **456**, 218 (2008).

[23] D. Fattal, K. Inoue, J. Vučković, C. Santori, G. S. Solomon, and Y. Yamamoto, Phys. Rev. Lett. **92**, 037903 (2004).

[24] L. Childress, J. M. Taylor, A. S. Sørensen, and M. D. Lukin, Phys. Rev. A **72**, 052330 (2005).

[25] M. D. Lukin and A. Imamoğlu, Phys. Rev. Lett. **84**, 1419 (2000).

[26] S. Reitzenstein, C. Hofmann, A. Gorbunov, M. Strauß, S. H. Kwon, C. Schneider, A. Löffler, S. Höfling, M. Kamp, and A. Forchel, Applied Physics Letters **90**, 251109 (2007).

[27] K. Srinivasan and O. Painter, Nature **450**, 862 (2007).

[28] F. S. F. Brossard, X. L. Xu, D. A. Williams, M. Hadjipanayi, M. Hugues, M. Hopkinson, X. Wang, and R. A. Taylor, Applied Physics Letters **97**, 111101 (2010).

[29] J. D. Joannopoulos, R. D. Meade, and J. N. Winn, *Photonic Crystals* (Princeton, Boston, 1995).

[30] Y. Akahane, T. Asano, B.-S. Song, and S. Noda, Opt. Express **13**, 1202 (2005).

[31] K. M. Leung and Y. F. Liu, Phys. Rev. Lett **65**, 2646 (1990).

[32] K. Kawano and T. Kitoh, *Introduction to optical waveguide analysis: Solving Maxwell's Equations and the Schrodinger Equation* (John Wiley and Sons, Inc., Canada, 2001).

[33] A. Mekis, F. Shanhui, and J. D. Joannopoulos, IEEE Microwave and Guided Wave Letters **9**, 502 (1999).

[34] K. Yee, IEEE Transactions on Antennas and Propagation **14**, 302 (1966).

[35] S.-H. Sun and C. Choi, Microwave and Wireless Components Letters **17**, 253 (2007).

[36] J. P. Berenger, J. Comp. Phys. **114**, 185 (1994).

[37] A. F. Oskooi, D. Roundy, and M. Ibanescu, Computer Physics Communications **181**, 687 (2010).

[38] H. Kroto and J. Heath, Nature **318**, 162 (1985).

[39] P. R. Buseck, S. J. Tsipursky, and R. Hettich, Science **257**, 215 (2002).

[40] J. Cami, J. Bernard-Salas, E. Peeters, and S. E. Malek, Science **329**, 1180 (2010).

[41] D. S. Bethune, C. H. Kiang, M. S. de Vries, G. Gorman, R. R. Savoy, J. Vazquez, and R. Beyers, Nature **363**, 605 (1993).

[42] K. Kobayashi and S. Nagase, Chemical Physics Letters **262**, 227 (1995).

[43] K. Kobayashia, S. Nagasea, and T. Akasakab, Chemical Physics Letters **261**, 502 (1995).

[44] W. Harneit, Phys. Rev. A **65**, 032322 (2002).

[45] S. Stevenson, G. Rice, T. Glass, K. Harich, F. Cromer, M. R. Jordan, J. Craft, E. Hadju, R. Bible, M. M. Olmstead, K. Maitra, A. J. Fisher, A. L. Balch, and H. C. Dorn, Nature **401**, 55 (1999).

[46] N. Ganesh, W. Zhang, P. C. Mathias, E. Chow, J. A. N. T. Soares, V. Malyarchuk, A. D. Smith, and B. T. Cunningham, Nature **2**, 515 (2007).

[47] E. by Albert G. Baca and C. I. H. Ashby, *Fabrication of GaAs Devices* (The institution of Electrical Engineers, London, United Kingdom, 2005).

[48] D. Rosenblatt, A. Sharon, and A. A. Friesem, IEEE Journal of Quantum Electronics **33**, 2038 (1997).

[49] A. Nish, J.-Y. Hwang, J. Doig, and R. J. Nicholas, Nature Nanotechnology **2**, 640 (2007).

[50] A. Y. Cho and J. R. Arthur, Progress in Solid-State Chemistry **10**, 157 (1975).

[51] S. Ino, Japanese Journal of Applied Physics **16**, 891 (1977).

[52] B. Alloing, C. Zinoni, V. Zwiller, L. H. Li, C. Monat, M. Gobet, G. Buchs, A. Fiore, E. Pelucchi, and E. Kapon, Applied Physics Letters **86**, 101908 (2005).

[53] S. Rodt, R. Heitz, R. L. Sellin, A. Schliwa, K. Poschke, and D. Bimberg, Physica E **21**, 1065 (2004).

[54] K. S. Il'in, M. Lindgren, M. Currie, A. D. Semenov, G. N. Gol'Tsman, R. Sobolewski, S. I. Cherednichenko, and E. M. Gershenzon, Applied Physics Letters **76**, 2752 (2000).

[55] K. M. Rosfjord, J. K. W. Yang, E. A. Dauler, A. J. Kerman, V. Anant, B. M. Voronov, G. N. Gol'tsman, and K. K. Berggren, Optics Express **14**, 527 (2006).

[56] robert h. hadfield, Nature Photonics **3**, 696 (2009).

[57] R. H. Hadfield, M. J. Stevens, S. S. Gruber, and A. J. Miller, Optics Express **13**, 10846 (2005).

[58] K. H. Lee, A. M. Green, R. A. Taylor, D. N. Sharp, J. Scrimgeour, O. M. Roche, J. H. Na, A. F. Jarjour, A. J. Turberfield, F. S. F. Brossard, D. A. Williams, , and G. A. D. Briggs, Applied Physics Letters **88**, 193106 (2006).

[59] M. Fox, *Quantum Optics, An Introduction* (Oxford University Press, Oxford, 2006).

[60] X. M. Wen, L. V. Dao, P. Hannaford, S. Mokkapati, H. H. Tan, and C. Jagadish, Journal of Physics: Condensed Matter **19**, 386213 (2007).

[61] Y. Zhong, K. S. Wong, W. Zhang, and D. C. Look, Applied Physics Letters **89**, 022108 (2006).

[62] Z. Lin and K. Lian, Mirosystem Technologies **13**, 253 (2007).

[63] S. M. Thon, M. T. Rakher, H. Kim, J. Gudat, W. T. M. Irvine, P. M. Petroff, and D. Bouwmeester, Applied Physics Letters **94**, 111115 (2009).

[64] E. M. Purcell, Phys. Rev. **69**, 681 (1946).

[65] Y. Yamamoto and R. E. Slusher, Physics Today **46**, 66 (1993).

[66] G. Khitrova, H. M. Gibbs, M. Kira, S. W. Koch, and A. Scherer, Nature Physics **2**, 81 (2006).

[67] G. Bastard, *Wave Mechanics Applied to Semiconductor Heterostructures* (Wiley, New York, 1991).

[68] A. Gruber, A. Drabenstedt, C. Tietz, L. Fleury, C. W. J, and C. von Borczyskowski, Science **276**, 2012 (1997).

[69] A. Kuhn, M. Hennrich, and G. Rempe, Physical Review Letters **89**, 067910 (2002).

[70] K. Tanaka, T. Nakamura, W. Takamatsu, M. Yamanishi, Y. Lee, and T. Ishihara, Phys. Rev. Lett. **74**, 3380 (1995).

[71] M. Bayer, T. L. Reinecke, F. Weidner, A. Larionov, A. McDonald, and A. Forchel, Phys. Rev. Lett. **86**, 3168 (2001).

[72] T. Yoshie, A. Scherer, J. Hendrickson, G. Khitrova, H. M. Gibbs, G. Rupper, C. Ell, O. B. Shchekin, and D. G. Deppe, Nature (London) **432**, 200 (2004).

[73] E. Peter, P. Senellart, D. Martrou, A. Lemaitre, J. Hours, J. M. Gérard, and J. Bloch, Phys. Rev. Lett. **95**, 067401 (2005).

[74] R. J. Thompson, G. Rempe, and H. Kimble, Physical Review Letters **68**, 1132 (1992).

[75] J. P. Reithmaier, G. Sk, A. Löffler, C. Hofmann, S. Kuhn, S. Reitzenstein, L. V. Keldysh, V. D. Kulakovskii, T. L. Reinecke, and A. Forchel, Nature **432**, 197 (2004).

[76] R. J. Thompson, Q. A. Turchette, O. Carnal, and H. J. Kimble, Phys. Rev. A **57**, 3084 (1998).

[77] L.-g. Zhou, L. F. Wei, M. Gao, and X.-b. Wang, Phys. Rev. A **81**, 042323 (2010).

[78] M. Kaniber, A. Laucht, A. Neumann, J. M. Villas-Bôas, M. Bichler, M.-C. Amann, and J. J. Finley, Phys. Rev. B **77**, 161303 (2008).

[79] B. S. Song, S. Noda, T. Asano, and Y. Akahane, Nature Materials **4**, 207 (2005).

[80] E. Kuramochi, M. Notomi, S. Mitsugi, A. Shinya, T. Tanabe, and T. Watanabe, Applied Physics Letters **88**, 041112 (2006).

[81] M. Notomi, E. Kuramochi, and T. Tanabe, Nature Photonics **2**, 741 (2008).

[82] K. Hennessy, A. Badolato, A. Tamboli, P. M. Petroff, E. Hua, M. Atature, J. Dreiser, and A. Imamoglu, Applied Physics Letters **87**, 021108 (2005).

[83] D. C. Reynolds, K. K. Bajaj, C. W. Litton, G. Peters, P. W. Yu, and J. D. Parsons, Journal of Applied Physics **61**, 342 (1987).

[84] C. P. Michael, K. Srinivasan, T. J. Johnson, O. Painter, K. H. Lee, K. Hennessy, H. Kim, and E. Hu, Applied Physics Letters **90**, 051108 (2007).

[85] J. Hendrickson, B. C. Richards, J. Sweet, S. Mosor, C. Christenson, D. Lam, G. Khitrova, H. M. Gibbs, T. Yoshie, A. Scherer, O. B. Shchekin, and D. G. Deppe, Phys. Rev. B **72**, 193303 (2005).

[86] M. T. Rakher, S. Strauf, Y. Choi, N. G. Stolz, K. J. Hennessey, H. Kim, A. Badolato, L. A. Coldren, E. L. Hu, P. M. Petroff, and D. Bouwmeester, Proc. SPIE **6481**, 648109 (2007).

[87] A. Einstein, B. podolsky, and N. Rosen, Phys. Rev. **47**, 477 (1935).

[88] M. Brune, F. Schmidt-Kaler, A. Maali, J. Dreyer, E. Hagley, J. M. Raimond, and S. Haroche, Phys. Rev. Lett. **76**, 1800 (1996).

[89] L. C. Andreani, D. Gerace, and M. Agio, physica status solidi (b) **242**, 2197 (2005).

[90] L. C. Andreani and G. Panzarini, Phys. Rev. B **60**, 13276 (1999).

[91] E. Moreau, I. Robert, L. Manin, V. Thierry-Mieg, J.-M. Gérard, and I. Abram, Phys. Rev. Lett. **87**, 183601 (2001).

[92] D. V. Regelman, U. Mizrahi, D. Gershoni, E. Ehrenfreund, W. V. Schoenfeld, and P. M. Petroff, Phys. Rev. Lett. **87**, 257401 (2001).

[93] S. Mosor, J. Hendrickson, B. C. Richards, J. Sweet, G. Khitrova, H. M. Gibbs, T. Yoshie, A. Scherer, O. B. Shchekin, and D. G. Deppe, Applied Physics Letters **87**, 141105 (2005).

[94] A. Badolato, K. Hennessy, M. Atatüre, J. Dreiser, E. Hu, P. M. Petroff, and A. Imamoğlu, Science **308**, 1158 (2005).

[95] J. Robertson, Materials Science and Engineering R **37**, 129 (2002).

[96] S. Iijima, Nature **354**, 56 (1991).

[97] D. Bethune, C. Klang, M. de Vries, G. Gorman, R. Savoy, J. Vazquez, and R. Beyers, Nature **363**, 605 (1993).

[98] S. Reich, C. Thomsen, and J. Maultzsch, *Carbon Nanotubes* (Wiley, VCH, 2004).

[99] A. K. Geim and K. S. Novoselov, Nature Materials **6**, 183 (2007).

[100] S. M. Bachilo, M. S. Strano, C. Kittrell, R. H. Hauge, R. E. Smalley, and R. B. Weisman, Science **298**, 2361 (2002).

[101] R. B. Capaz, C. D. Spataru, S. Ismail-Beigi, and S. G. Louie, Phys. Rev. B **74**, 121401 (2006).

[102] *Carbon Nanotubes*, edited by A. Jorio, G. Dresselhaus, and M. S. Dresselhaus (Springer, Germany, 2008).

[103] T. Guo, P. Nikolaev, A. Thess, D. Colbert, and R. Smalley, Chem. Phys. Lett. **243**, 49 (1995).

[104] Z. Shi, Y. Lian, X. Zhou, Z. Gu, Y. Zhang, S. Iijima, L. Zhou, K. T. Yue, and S. Zhang, Carbon **37**, 1449 (1999).

[105] T. Okazaki, T. Saito, K. Matsuura, S. Ohshima, M. Yumura, Y. Oyama, R. Saito, and S. Iijima, Chem. Phys. Lett. **420**, 286 (2006).

[106] J. Wiltshire, A. Khlobystov, L. Li, S. Lyapin, G. Briggs, and R. Nicholas, Chem. Phys. Lett. **386**, 239 (2004).

[107] S. M. Bachilo, L. Balzano, J. E. Herrera, F. Pompeo, D. E. Resasco, and R. B. Weisman, J. Am. Chem. Soc. **125**, 11186 (1999).

[108] J. R. Lakowiecz, *Principles of Fluorescence Spectroscopy, Second Edn* (Kluwer Academic, Plenum Publishers, 1999).

[109] J. X. Geng and T. Y. Zeng, J. Am. Chem. Soc. **128**, 16827 (2006).

[110] J. Arranz-Andres and W. J. Blau, Carbon **46**, 2067 (2008).

[111] Y. Kanai and J. C. Grossman, Nano Lett. **8**, 908 (2008).

[112] S. D. Stranks, C. Weisspfennig, P. Parkinson, M. B. Johnston, L. M. Herz, and R. J. Nicholas, Nano Lett. **11**, 66 (2011).

[113] M. J. O'Connell, S. M. Bachilo, C. B. Huffman, V. C. Moore, M. S. Strano, E. H. Haroz, K. L. Rialon, P. J. Boul, W. H. Noon, C. Kittrell, J. Ma, R. H. Hauge, R. B. Weisman, and R. E. Smalley, Science **297**, 593 (2002).

[114] T. Schuettfort, A. Nish, and R. J. Nicholas*, Nano Lett. **9**, 3871 (2009).

[115] J. H. Choi and M. S. Strano, Applied Physics Letters **90**, 223114 (2007).

[116] M. Dresselhaus, G. Dresselhaus, R. Saito, and A. Jorio, Physics Reports **409**, 47 (2005).

[117] V. Perebeinos, J. Tersoff, and P. Avouris, Nano Lett. **5**, 2495 (2005).

[118] F. Wang, G. Dukovic, L. E. Brus, and T. F. Heinz, Phys. Rev. Lett **92**, 177401 (2004).

[119] A. Hagen, G. Moos, V. Talalaev, and T. Hertel, Applied Physics Letters **78**, 1137 (2004).

[120] J. Lefebvre, J. Fraser, Y. Homma, and P. Finnie, Applied Physics Letters **78**, 1107 (2004).

[121] A. Srivastava, H. Htoon, V. I. Klimov, and J. Kono, Phys. Rev. Lett **101**, 087402 (2008).

[122] V. Perebeinos and P. Avouris, Phys. Rev. Lett **101**, 057401 (2008).

[123] F. Chen, W. Zhang, M. Jia, L. Wei, X.-F. Fan, J.-L. Kuo, Y. Chen, M. B. Chan-Park, A. Xia, , and L.-J. Li, J. Phys. Chem. C **113**, 14946 (2009).

[124] J. Gao, M. A. Loi, E. J. F. de Carvalho, and M. C. dos Santos, ACS Nano **5**, 3993 (2011).

[125] S. G. Chou, F. Plentz, J. Jiang, R. Saito, D. Nezich, H. B. Ribeiro, A. Jorio, M. A. Pimenta, G. G. Samsonidze, A. P. Santos, M. Zheng, G. B. Onoa, E. D. Semke, G. Dresselhaus, and M. S. Dresselhaus, Phys. Rev. Lett **94**, 127402 (2005).

[126] O. Kiowski, S. Lebedkin, F. Hennrich, and M. M. Kappes, Phys. Rev. B **76**, 075422 (2007).

[127] P. L. McEuen, M. Bockrath, D. H. Cobden, Y.-G. Yoon, and S. G. Louie, Phys. Rev. Lett. **83**, 5098 (1999).

[128] C. Georgi, A. A. Green, M. C. Hersam, and A. Hartschuh, ACS Nano **4**, 5914 (2010).

[129] G. Lindwall, A. Wacker, C. Weber, and A. Knorr, Phys. Rev. Lett. **99**, 087401 (2007).

[130] J. Wallentin, K. Mergenthaler, M. Ek, L. R. Wallenberg, L. Samuelson, K. Deppert, M.-E. Pistol, and M. T. Borgström, Nano Letters **11**, 2286 (2011).

[131] S. A. Empedocles and M. G. Bawendi, Science **278**, 2114 (1997).

[132] J. Muller, J. M. Lupton, A. L. Rogach, J. Feldmann, D. V. Talapin, and H. Weller, Phys. Rev. Lett. **93**, 167402 (2004).

[133] K. Matsuda, T. Inoue, Y. Murakami, S. Maruyama, and Y. Kanemitsu, Phys. Rev. B **77**, 193405 (2008).

[134] H. Qian, P. T. Araujo, C. Georgi, T. Gokus, N. Hartmann, A. A. Green, A. Jorio, M. C. Hersam, L. Novotny, and A. Hartschuh, Nano Letters **8**, 2706 (2008), pMID: 18671438.

[135] H. Harutyunyan, T. Gokus, A. A. Green, M. C. Hersam, M. Allegrini, and A. Hartschuh, Nano Letters **9**, 2010 (2009).

[136] I. B. Mortimer and R. J. Nicholas, Phys. Rev. Lett. **98**, 027404 (2007).

[137] A. W. Holleitner, R. H. Blick, A. K. Hüttel, K. Eberl, and J. P. Kotthaus, Science **297**, 70 (2002).

[138] T. B. Tran, I. S. Beloborodov, X. M. Lin, T. P. Bigioni, V. M. Vinokur, and H. M. Jaeger, Phys. Rev. Lett. **95**, 076806 (2005).

[139] A. Hartschuh, H. Qian, A. J. Meixner, N. Anderson, and L. Novotny, Nano Letters **5**, 2310 (2005).

[140] H. Hirori, K. Matsuda, Y. Miyauchi, S. Maruyama, and Y. Kanemitsu, Phys. Rev. Lett. **97**, 257401 (2006).

[141] Y. Lü, H. Liu, and B. Gu, The European Physical Journal B - Condensed Matter and Complex Systems **74**, 499 (2010), 10.1140/epjb/e2010-00098-1.

[142] B. Gao, D. C. Glattli, B. Placais, and A. Bachtold, Phys. Rev. B **74**, 085410 (2006).

[143] A. Zrenner, Journal of Chemical Physics **112**, 7790 (2000).

[144] J. D. Teufel, D. Li, M. S. Allman, K. Cicak, A. J. Sirois, J. D. Whittaker, and R. W. Simmonds, Nature **471**, 204 (2011).

[145] G. Pennington and N. Goldsman, Phys. Rev. B **71**, 205318 (2005).